The Dissertation Committee for Danielle Salina Applestone Certifies that this is the approved version of the following dissertation:

SYNTHESIS AND CHARACTERIZATION OF NANOCOMPOSITE ALLOY ANODES FOR LITHIUM-ION BATTERIES

Committee:

Arumugam Manthiram, Supervisor

John Goodenough

Keith Stevenson

Jeremy Meyers

Charles Mullins

SYNTHESIS AND CHARACTERIZATION OF NANOCOMPOSITE ALLOY ANODES FOR LITHIUM-ION BATTERIES

by

Danielle Salina Applestone, S. B. Chem. E.

Dissertation

Presented to the Faculty of the Graduate School of

The University of Texas at Austin

in Partial Fulfillment

of the Requirements

for the Degree of

Doctor of Philosophy

The University of Texas at Austin

May 2012

Dedication

Dedicated to Rhett Love Applestone

Acknowledgements

I would like to specifically thank Professor Arumugam Manthiram for giving me more chances to complete this work than I probably deserved. Because of his incredible character and the freedom with which he allows his students to work, I have learned far more about myself and batteries than I thought possible in such a short period of time. I would also like to thank Professors John Goodenough, Jeremy Meyers, Keith Stevenson, and Charles Mullins for agreeing to serve on my dissertation committee and for giving clear direction to me during my oral preliminary exam.

Dr. Sukeun Yoon was absolutely essential to my success in completing this dissertation research. He was a great mentor and good energy to be around in the lab. Thank you to Dr. Anmin Cao for all of his hard work helping me with TEM analysis. I would also like to thank Dr. Hugo Celio for his patience in teaching me how to use the Kratos XPS machine. A special thank you to Katharine Harrison for helping to change the lab culture and for just always being there, for having high standards for safety and cleanliness, and for being wonderful to work with in the lab. Additionally, this work could not have been completed without the financial support of the Department of Energy Basic Science grant number DE-SC0005397.

Big thanks go to Rhett Creighton for the sacrifices he made in order to support my desire to improve my education, even when it looked like I might not succeed. And thank you to my parents and friends for all of the encouragement and love it took to finally complete this era of my life.

SYNTHESIS AND CHARACTERIZATION OF NANOCOMPOSITE ALLOY ANODES FOR LITHIUM-ION BATTERIES

Danielle Salina Applestone, Ph.D.

The University of Texas at Austin, 2012

Supervisor: Arumugam Manthiram

Lithium-ion batteries are most commonly employed as power sources for portable electronic devices. Limited capacity, high cost, and safety problems associated with the commercially used graphite anode materials are hampering the use of lithium-ion batteries in larger-scale applications such as the electric vehicle. Nanocomposite alloys have shown promise as new anode materials because of their better safety due to higher operating potential, increased energy density, low cost, and straightforward synthesis as compared to graphite. The purpose of this dissertation is to investigate and understand the electrochemical properties of several types of nanocomposite alloys and to assess their viability as replacement anode materials for lithium-ion batteries.

Tin and antimony are two elements that are active toward lithium. Accordingly, this dissertation is focused on tin-based and antimony-based nanocomposite alloy materials. Tin and antimony each have larger theoretical capacities than commercially available anodes, but the capacity fades dramatically in the first few cycles when metallic tin or antimony is used as the anode in a lithium-ion battery. This capacity fade is largely due to the agglomeration of particles in the anode material and the formation of a barrier layer between the surface of the anode and the electrolyte. In order to suppress agglomeration, the active anode material can be constrained by an inactive matrix of

material that makes up the nanocomposite. By controlling the surface of the particles in the nanocomposite via methods such as the addition of additives to the electrolyte, the detrimental effects of the solid-electrolyte interphase layer (SEI) can be minimized, and the capacity of the material can be maintained. Moreover, the nanocomposite alloys described in this dissertation can be used above the voltage where lithium plating occurs, thereby enhancing the safety of lithium-ion batteries.

The alloy anodes in this study are synthesized by high-energy mechanical milling and furnace heating. The materials are characterized by X-ray diffraction, scanning and transmission electron microscopies, and X-ray photoelectron spectroscopy. Electrochemical performances are assessed at various temperatures, potential ranges, and charge rates. The lithiation/delithiation reaction mechanisms for these nanocomposite materials are explored with *ex-situ* X-ray diffraction.

Specifically, three different nanocomposite alloy anode materials have been developed: Mo_3Sb_7-C, Cu_2Sb-Al_2O_3-C, and Cu_6Sn_5-TiC-C. Mo_3Sb_7-C has high gravimetric capacity and involves a reaction mechanism whereby crystalline Mo_3Sb_7 disappears and is reformed during each cycle. Cu_2Sb-Al_2O_3-C with small particles (2 - 10 nm) of Cu_2Sb dispersed in the Al_2O_3-C matrix is made by a single-step ball milling process. It exhibits long cycle life (+ 500 cycles), and the reversibility of the reaction of Cu_2Sb-Al_2O_3-C with lithium is improved when longer milling times are used for synthesis. The reaction mechanism for Cu_2Sb-Al_2O_3-C appears to be dependent upon the size of the crystalline Cu_2Sb particles. The coulombic efficiency of Cu_2Sb-Al_2O_3-C is improved through the addition of 2 % vinylethylene carbonate to the electrolyte. With a high tap density of 2.2 g/cm^3, Cu_6Sn_5-TiC-C exhibits high volumetric capacity. The reversibility of the reaction of Cu_6Sn_5-TiC-C with lithium is improved when the material is cycled above 0.2 V vs. Li/Li^+.

Table of Contents

List of Tables

List of Figures

Chapter 1: Introduction

1.1 THE NEED FOR NEW ANODE MATERIALS

Lithium-ion batteries have become the power source of choice for portable devices due to their higher energy density compared to other rechargeable systems. They are now being intensively pursued for electric vehicles (EV) and hybrid electric vehicles (HEV). Lithium-ion batteries currently use graphite as the anode due to its excellent cycling behavior. However, graphite has a limited theoretical capacity of 372 mAh/g. The formation of a solid electrolyte interphase (SEI) layer by a reaction of the graphite surface with the electrolyte and an operating voltage close to that of Li/Li^+ lead to a plating of metallic lithium on the graphite surface, which results in safety issues. These safety problems are particularly exacerbated under high rates of charge/discharge and at low temperatures as lithium-ion diffusion through the SEI layer becomes difficult. The charge rate of the batteries is a critical parameter for vehicle applications. An additional factor important for vehicle applications is volumetric energy density. When space is a concern, volumetric capacity and volumetric energy density are just as important as or more important than the gravimetric energy density. The low tap density and the limited theoretical gravimetric capacity along with the safety concerns make graphite an inadequate anode material for the batteries of the future, particularly for vehicle applications. These pitfalls of the graphite anode demand the development of alternate anode materials [1-4].

Several lithium alloy anode materials of the form Li_xM_y have attracted much attention due to their high theoretical capacity values. For example, $Li_{3.75}Si$ (3578 mAh/g) [5-8], $Li_{3.75}Ge$ (1385 mAh/g) [9], $Li_{4.4}Sn$ (993 mAh/g) [10-14], and Li_3Sb (660 mAh/g)

[15], have theoretical capacity values much higher than that of a graphite anode. Unfortunately, the use of these alloy anodes in practical lithium-ion cells has been plagued by severe capacity fade arising from a huge volume change and particle agglomeration that occurs during the charge/discharge (lithium alloying/dealloying) process. The volume change leads to lattice stress and consequent cracking and crumbling of the alloy particles during cycling, resulting in an abrupt loss of capacity within a few charge-discharge cycles. Particle agglomeration increases the diffusion distance for lithium and decreases the reversibility of the charge/discharge reaction.

Because there are a variety of applications for which lithium-ion batteries can be used, different factors of the anode materials become important depending on the application. Operating voltage range (or reduction potential) of the anode material is a critical parameter for the safety of the battery. Low-temperature and high-temperature performance are important when a battery will be used in extreme or outdoor conditions. Volumetric capacity and volumetric energy density are important when available space is limited. Gravimetric capacity and gravimetric energy density affect how light a battery can be. Rate capability and cycle life are two other factors that are important to consider for applications such as electric vehicles where the lifetime of the application is on the order of 10 years, and the battery is expected to charge quickly. Of all the properties to consider, one of the most important factors that determine the viability of a particular anode material is its compatibility with the cutting-edge commercial cathode materials. Graphite in particularly suffers from manganese poisoning when it is used with manganese-containing spinel and layered cathode materials. A variety of factors need to be considered for each material when determining its appropriateness for a particular application.

1.2 STRATEGIES FOR ENGINEERING NEW ANODE MATERIALS

In order for alloy anode materials to be accepted as an alternative to the commercial graphite anode material, the structural decomposition that occurs during cycling must be addressed. To overcome the structural problems with the alloy anode materials, significant effort has been focused on minimizing the negative effects of volume expansion by reducing the particle size of the materials into the nanoscale. The stress and strain on a nanoscale particle is less than that on larger particles, and it is possible that nanostructured materials can withstand the stresses that occur during the insertion and extraction of lithium. Although the nanostructured materials are expected to offer shorter diffusion lengths for lithium ions and accommodate the strain occurring during cycling [16,17], the large surface-to-volume ratio and the high surface reactivity of nanostructured materials can be problematic. The high surface reactivity can lead to unfavorable reactions with the electrolyte, among other negative effects.

Another strategy for improving the performance of alloy anodes is the active-inactive composite materials. The active–inactive composite strategy involves a mixture of two materials: one reacts with lithium while the other material acts as an electrochemically inactive matrix and buffers the volume change during the charge/discharge cycle. Dahn and coworkers [18] applied this strategy to several Sn-M-C systems with M = Ti, V, Cr, Mn, Fe, and Co and found an improvement in cycling performance when compared to that of pure Sn. Many other groups have established the utility of the active-inactive composite strategy when it comes to improving the performance of alloy anode materials for lithium-ion batteries [16,17,19].

1.3 TIN-BASED ANODES

Among the various possible anode alternatives pursued, Sn-based materials have been suggested as one of the most promising candidates to replace graphite due to their

high capacity, high packing density, and safer thermodynamic potential compared to the carbonaceous anode materials [17,20]. The use of Sn-based anodes in practical lithium-ion cells has generally been plagued by severe capacity fade that arises from a large volume change occurring during the charge–discharge process. The volume change leads to lattice stress and subsequent cracking and crumbling of the alloy particles during cycling, resulting in an abrupt decrease in capacity within a few charge–discharge cycles [21,22]. Many attempts have been made to overcome these problems by employing nanostructured Sn alloy particles as the active material or intermetallic alloys with a composite structure that contains an active or inactive host matrix.

In a study that was published regarding an Sn-Ti-C composite, a stable cycle life of 300 cycles at a capacity of 370 mAh/g and ~ 850 mAh/cm^3 was achieved [23]. The behavior of the Sn-Ti-C material showed that it is possible to circumvent the problem of severe capacity fade by employing a compositing strategy with Sn-based materials. Commercially, Sony Corporation is using an Sn-Co-C material in their Nexelion battery. Although the Nexelion is in production, it is not considered to be a viable anode material for widespread adoption, particularly for vehicle applications, on account of the expensive and toxic cobalt being part of the material.

It is possible to increase the amount of active Sn relative to the inactive portion of the composite, thereby increasing the capacity of the composite material. However, the challenge is to maintain the beneficial volume change buffering effects of the composite while getting as much capacity out of the material as possible. In order to create composite materials with higher, yet still stable capacities, the combination of the nanostructuring strategy and the active-inactive matrix strategy is pursued in this dissertation. In this combined approach, nanostructured Sn-based alloys are created and

embedded in an inactive matrix of Ti and C. It is anticipated that this combination might yield a material that performs even better than the published Sn-Ti-C material.

Of the potential Sn-based alloys that are available, much work has been done exploring Cu_6Sn_5 without much success in achieving stable cycle performance or high volumetric capacity [24-27]. Part of the reason for this is the significant structural change that occurs when the material transitions from Cu_6Sn_5 to Li_2CuSn to $Li_{4.4}Sn$. The transition from Li_2CuSn to $Li_{4.4}Sn$ is thought to lead to irreversibilities in the capacity, and so when Cu_6Sn_5 is cycled, it is generally kept above a potential of 200 mV at which the Li_2CuSn to $Li_{4.4}Sn$ transition occurs. By limiting the amount of lithium inserted into the material by 2.4 Li per Sn, a drastic reduction in capacity is observed [27]. Thorne *et al*. [28] published information that showed that by creating an amorphous or nanostructured material from Cu_6Sn_5 and carbon, a stable cycle life of 100 cycles at 400 mAh/g could be achieved. Because of the advances made by Yoon and Manthiram [23] and by Thorne *et al*. [27] , a Cu_6Sn_5-TiC-C composite is pursued in this dissertation with an aim to realize higher gravimetric and volumetric capacities compared to those of the Sn-Ti-C material [23] and a more stable cycle life than the previously published data on the Cu_6Sn_5 material [27]. Accordingly, the investigation of the Cu_6Sn_5-TiC-C anode material is presented in Chapter 5.

1.4 ANTIMONY-BASED ANODES

With respect to alternative anodes, antimony alloys are appealing because they offer higher theoretical capacity than graphite (gravimetric and volumetric) and an operating voltage well above that of metallic lithium. Compared to the tin-based anodes, the operating voltage is also higher for antimony-based alloys, so offering better safety. Unfortunately, the reaction of antimony with lithium to form Li_3Sb is accompanied by a

large volume change of 137 % [4-8], which results in cracking and crumbling of the alloy particles, disconnection of the electrical contact between the particles and current collectors, and consequent capacity fade during cycling [9,10]. To alleviate this problem, antimony-containing intermetallic compounds with different lithium reaction mechanisms have been pursued over the years, *e.g.*, Cu_2Sb [11], CoSb [12], CrSb [13], and MnSb [14], in which only Sb is electrochemically active, and SnSb [15,29,30], InSb [31], Zn_4Sb_3 [32], and AlSb [33], in which both the metals are electrochemically active. However, most of these intermetallic alloy anodes still exhibit capacity fade. Accordingly, a portion of the research in this dissertation is dedicated to exploring another antimony-containing intermetallic compound that had not yet been explored: Mo_3Sb_7. This material also shows significant capacity fade, but the cycle life is improved through the addition of conductive carbon to form a Mo_3Sb_7-C composite. The culmination of research on Mo_3Sb_7-C is presented in Chapter 3. The Mo_3Sb_7-C composites offer the following advantages as an anode material: (i) active antimony particles are constrained in the crystal structure of Mo_3Sb_7, which suppresses the agglomeration responsible for much of the capacity fade with antimony alloy electrodes and (ii) the carbon matrix surrounding the Mo_3Sb_7 particles acts as a buffer to alleviate the volume expansion.

In order to blend the beneficial effects of nanostructuring with the beneficial effects of preparing an active-inactive matrix composite material, Cu_2Sb-Al_2O_3-C is created and studied. Past research in Manthiram group has established Sb-Al_2O_3-C as a nanocomposite material with good cycle life and a gravimetric discharge capacity over two times that of graphite [34]. Cu_2Sb has been widely studied and is considered to have stable performance, but the most stable cycles shown in the literature is under 100 [5,8,26,27,35-42]. The only Cu_2Sb related material to show more than 100 cycles was a

hollow Cu_2Sb-C core-shell nanoparticle material synthesized via a polyol process [43]. It is possible that the inactive host phases can inhibit lithium or electron transfer [44], but the research in this dissertation research shows a reduction in impedance and an improvement in performance, following the addition of an inactive matrix component. Chapter 4 of this dissertation focuses on the synthesis, characterization, and electrochemical testing of the nano-engineered Cu_2Sb-Al_2O_3-C composite anode. The Cu_2Sb-Al_2O_3-C nanocomposite offers several advantages: (i) the Al_2O_3-C ceramic and carbon matrix act as a buffer to absorb the volume expansion that occurs in the nanosized copper-antimony metal alloy particles, (ii) the Al_2O_3 and carbon matrix keeps the Cu_2Sb particles separate during cycling, thereby reducing agglomeration, (iii) Cu_2Sb-Al_2O_3-C is prepared by a simple, one step, high-energy mechanical milling (HEMM) synthesis of Sb_2O_3 with Al, Cu and C, and (iv) an operating voltage well above that of Li/Li^+ and the presence of Al_2O_3 on the Cu_2Sb particles during the ball-milling process can suppress the formation of an SEI layer [34].

1.5 SILICON-BASED ANODES

Silicon anodes have attracted a lot of attention due to the fact that a silicon atom can accommodate 4.4 lithium atoms, forming $Li_{22}Si_5$. As a result of this, silicon has the highest theoretical capacity (4200 mAh/g) of any alloying element [45]. This means that silicon anodes could possibly have over ten times the gravimetric capacity that that can be obtained with graphite. The appeal of such a drastic increase in the capacity of a lithium-ion battery anode material has resulted in a wealth of research into this area. However, the insertion of 4.4 lithium atoms per silicon atom has some repercussions. The full lithiation of silicon results in a 400 % increase in volume from cubic silicon (20.0 $Å^3$ per silicon atom) to cubic $Li_{22}Si_5$ (82.4 $Å^3$ per silicon atom) [46]. This extreme change in

volume leads to cracking and crumbling of the electrode material, as well as delamination from the electrode substrate. The physical degradation and loss of electrical contact yields significant losses in capacity and hence, poor cycle performance. As with tin and antimony-based anode materials, different strategies for mitigating the negative effects of the volume expansion have been pursued.

The primary strategies for creating silicon-based anode materials with good cycle performance are: controlling the structure and morphology, inactive matrix compositing, active matrix compositing, blending with various binders, and creation of silicon film electrodes [47-56]. Many gains have been made in terms of improved cycle performance of silicon anodes in the past eight years, utilizing these strategies. Some researchers have been able to attain 1500 mAh g^{-1} even after 400 cycles using vacuum deposited silicon on a well-etched substrate [53]. Gravimetric capacities close to the theoretical limit have been achieved through use of silicon nanotubes. For example, Park *et al*. [55] demonstrated a capacity of 3247 mAh/g with a coulombic efficiency of 89 % through the use of silicon nanotubes. It has been suggested that the reason for the improvement in cycle performance of silicon nanostructures is due to the improved mechanical properties of silicon when the size of the particles is reduced [51,55].

Although much improvement in the capacity retention of silicon anodes has been made, silicon still has two main drawbacks. The reduction potential of silicon is relatively low (~120 mV) [49], so silicon has the same problems of lithium metal plating at low temperatures. Low temperature operation is especially important for electric vehicle applications, where the conditions of use can be extreme. Silicon also has a low tap density (< 0.5 g/cm^3), so a less compelling volumetric capacity [17]. The low tap density of silicon anodes limit their adoption in applications where space is a concern, such as electric vehicles.

1.6 Optimization of performance with electrolyte additives

Good performance in terms of cycle life and safety are important for all batteries, but because of the nature of the application, these two metrics are of even higher priority for materials that will be used in electric vehicles. The introduction of additives into the battery electrolyte is one method that has been used to improve the performance and increase the safety of lithium-ion batteries. Electrolyte additives can reduce the impact of parasitic side reactions, solvent and salt ion degradation, lithium dendrite formation, and SEI (surface electrolyte interphase) layer formation, thus extending the cycle life of the batteries [57-61]. Flame retardants have also been introduced as electrolyte additives for their ability to improve the safety of a battery in the event of fire [62-65].

Electrolyte additives rely on different chemical strategies to improve battery performance, and often it is hard to determine which ones will be effective at improving the performance of a new material. Adding complication to the optimization process, when a material has already shown stable performance of hundreds of cycles, it is not always practical to wait the length of time that it takes to gather cycle data on the long-term performance of a battery before doing another round of optimization. It is also impractical to monopolize a large number of cycling channel resources for months by simply running cells with many different additives at different volume percentages and seeing which one is the best. For materials to make the leap from hundreds to tens of thousands of stable cycles, it is critical to develop ways that can reduce the amount of time needed to see which additives are the most effective at improving the performance.

1.7 Symmetric cell testing

The process of optimization and scale-up can be lengthy for a novel material coming from a research laboratory, and one of the critical factors in the success of a new battery material is the time to market. The more techniques that are available for rapid

optimization and screening of battery materials, the shorter the time to market can be, so the better the chances for commercial success with a new material. Symmetric cell testing is one method for making the battery optimization process more efficient. Symmetric cell testing has been used by several groups for fundamental lithium-ion battery research and has been proposed as a tool for electrolyte optimization [66-71]. The symmetric cell technique eliminates variables from the battery system while magnifying the ability to observe losses from the electrode material that is being tested. In most symmetric cells, the electrodes are made of the same base material, but one of the electrodes has been pre-lithiated. Because the cell has electrodes made from the same material, any losses or improvements that are observed are only due to one electrode material. For symmetric cell testing with anode materials, the effects of the electrolyte additive on the counter electrode or the lithium metal electrode are eliminated. When lithium metal is used as the counter electrode, the losses due to the irreversible consumption of lithium may not be apparent for many cycles, whereas those losses are quickly observed in a symmetric cell arrangement. The losses are more quickly observed in a symmetric cell because the amount of lithium in the system is fixed and much more limited than in a half cell.

The electrolyte additives chosen for this research are from the carbonate family. Vinylene carbonate (VC) has been used as an additive that increases the capacity retention of graphite anodes and is recommended for achieving the best battery performance with graphite. VC forms a surface polymer on the anode that has a higher conductivity than the normal SEI layer [17]. The surface polymer layer forms by reduction of VC before the EC of the electrolyte is reduced [61]. This polymerized VC-containing SEI layer suppresses further electrolyte and salt ion reduction [57]. Chen *et al*. [59] reported that the SEI layer that contained VC was impermeable to the electrolyte. Fluoroethylene carbonate (FEC) and vinylethylene carbonate (VEC) were also chosen as

candidate additives because of their benefit to the performance of alloy anodes in the literature [73-83]. The mechanism for the beneficial effects of FEC on silicon anodes is still not well understood, but recent studies have suggested that FEC is transformed into VC, and then the VC subsequently polymerizes and provides a stable protective layer on the outside of the electrode, much like what is observed with the addition of VC to the electrolyte [74]. The influence of FEC in the electrolyte is to shift the reduction peak to a higher potential [78]. This shift to higher potential causes FEC to be reduced before the EC/DEC of the electrolyte. The reduction potential of VEC is even higher than that of FEC [78,81]. VEC has been examined as an electrolyte additive because it forms a passivating film on the electrode surface, but is more stable than VC [80-81]. Use of VEC electrolyte additives can also reduce the amount of gas evolved during cell operation [82]. The effects of the three electrolyte additives on the coulombic efficiency and voltage profile of Cu_2Sb-Al_2O_3-C nanocomposite alloy anodes were measured in conventional half-cells and symmetric cells.

1.8 OBJECTIVES

Given the shortcomings of carbon-based anodes, the main objective of this research was to create anode materials for lithium-ion batteries that would be viable alternatives to graphite. The main benefits of graphite are its stable cycle performance and low cost. In order to compete with graphite using alloy anode materials, the problems of particle agglomeration and pulverization during cycling must be addressed. Until now, very few alloy anode materials have been able to overcome those problems. A handful of researchers have used nanostructuring or an active-inactive matrix strategy to improve the performance of alloy anode materials. Because of the gains made with nanostructuring and use of an active-inactive matrix strategy, it is proposed that the two

approaches be combined. With the combination of strategies, it is believed that a reduction of agglomeration and pulverization of particles could be achieved, and a stable cycle life comparable to that of graphite could be realized.

In order to address the question of cost competitiveness with graphite, the synthesis techniques used to make the alternative anode materials must be simple and scalable. The number of steps involved in the synthesis and processing should be kept to a minimum, and if at all possible, each step should result in a high yield of good quality material. Techniques that use high-cost or precision instrumentation should be avoided when attempting to reduce the synthesis cost. Additionally, the cost of the starting materials must be considered. When expensive precursors are used for the production of materials, it is hard for the performance of the material to overshadow the increased cost when compared to what is already in use commercially.

With all of the above considerations in mind, the objective of this research is to combine the nanostructuring strategy with the active-inactive matrix strategy to synthesize nanocomposite alloy anode materials. The synthesis methods are kept simple and scalable: high-energy mechanical milling and furnace heating; also, no cost prohibitive starting materials are used. In addition, this research has laid the groundwork for an entire library of materials to be explored. For each battery application, there are different properties that are necessary, and so having a variety of alternative anode materials is extremely valuable. In order to further develop and improve the performance of the nanocomposite alloy anode materials, the use of electrolyte additives is explored. The beneficial effects of electrolyte additives have been studied primarily on graphite, and so it is of interest to see if those effects would translate to other anode materials. Because one of the limiting factors in battery material optimization is time, symmetric cell testing is explored as a technique to rapidly determine the effects of electrolyte

additives on cell performance. It is important to view battery materials research through the eyes of the end user, and so this research has been executed with commercial viability in mind. However, throughout the development of these nanocomposite alloy anode materials, several interesting basic science questions have been uncovered and therefore, this research presents a balance between applied and fundamental aspects.

Chapter 2: Experimental Procedures

2.1 MATERIALS SYNTHESIS

The procedures used to synthesize the materials in this research are described within each individual chapter.

2.2 MATERIALS CHARACTERIZATION TECHNIQUES

2.2.1 X-ray diffraction (XRD)

In X-ray diffraction, an incident beam of X-rays enters the atomic planes of crystals and is diffracted in a particular way, according to the crystal structure of the material. The X-ray diffraction (XRD) pattern is specific to each crystal structure, and this means that XRD patterns can be used for identification and analysis of structures. In this study, XRD patterns were collected with a Rigaku Ultima IV X-ray diffractometer and a Philips X-ray diffractometer with Cu Kα radiation.

To investigate the structural changes that may occur during electrochemical cycling, *ex-situ* XRD data were collected. The electrodes for *ex-situ* XRD evaluation were prepared by mixing 70 wt. % active material powder, 15 wt. % carbon black (Super P), and 15 wt. % polytetrafluoroethylene (PTFE) with several drops of 2-propanol. The electrodes were pressed into copper mesh and dried at 120 ºC overnight under vacuum before being assembled into coin cells for cycling to various potentials.

2.2.2 X-ray photoelectron spectroscopy (XPS)

X-ray photoelectron spectroscopy is a surface analysis technique whereby a sample is irradiated with X-rays and electrons escape from the top ~ 10 nm of the sample. The number of escaping electrons is counted, and the kinetic energy of the escaping electrons is measured. The XPS spectra are created by graphing the number of electrons that escape within a range of kinetic energies. Knowing the energy of the incident X-ray

and the kinetic energy, the binding energy of the electron ejected is obtained. XPS can be used to determine the composition of a material, as well as the oxidation state of the ions present in the material. For this study, the XPS was operated with a monochromatic Al Kα source. For certain samples, the surface of the XPS sample needed to be cleaned of surface oxides and other contamination through sputtering with a 4 keV beam energy and an extractor current of 75 μA. For the air-sensitive electrode samples studied in this work, the electrode samples were transferred from an Ar-filled glovebox into the XPS chamber via an argon-filled capsule built at the Surface Analysis Laboratory of the Texas Materials Institute (TMI) at UT-Austin.

2.2.3 Scanning electron microscopy (SEM)

Scanning electron microscopy (SEM) uses a high energy electron beam to raster across a sample and creates greyscale images of an object by detecting the secondary electrons that are scattered by the interaction of the primary electron beam with the surface atoms of the sample. In this work, the SEM analyses were carried out with a JEOL JSM – 5610 SEM system.

2.2.4 Transmission electron microscopy (TEM)

In TEM, a beam of electrons is passed through an ultra thin specimen. The electrons in the beam interact with the specimen, and an image is formed based on that interaction. The transmitted beam is magnified and focused onto an imaging device. TEM analysis in this study was performed with a JEOL 2010 TEM operating at 300 kV.

2.2.5 Scanning transmission electron microscopy (STEM)

An STEM is a type of TEM where the electron beam is focused on a narrow spot that is rastered across a sample. The STEM used in this research was a Hitachi S-5500 STEM system.

2.2.6 Charge-discharge measurements

Cycle testing was performed on an Arbin cycler at various temperatures and current ratings.

The electrodes for the electrochemical evaluation were prepared by mixing 70 wt. % active material powder, 15 wt. % carbon black (Super P), and 15 wt. % polyvinylidene fluoride (PVDF) in N-methylpyrrolidone (NMP) to form a slurry. The slurry was spread onto a copper foil and dried at 120 ºC for 2 h under vacuum.

For half cell cycle testing, the electrodes were then assembled into CR2032 coin cells in an Ar-filled glove box with Celgard polypropylene separator, and lithium foil as the counter electrode. Unless otherwise stated, the electrolyte used in all cells was 1 M $LiPF_6$ in ethylene carbonate (EC)/diethyl carbonate (DEC) (1 : 1 v/v) electrolyte. For full cell testing, three-electrode, coffee-bag type cells were constructed with commercial materials for the cathode and lithium metal as the reference electrode. Full cells were assembled in an Ar-filled glove box with Celgard polypropylene separator. For symmetric cell testing, a conventional half cell was assembled using an electrode with approximately twice the area of a normal half cell. This half cell with a larger electrode was then subjected to one conditioning cycle, followed by full lithiation. After full lithiation, the large electrode was removed from its half cell in an Ar-filled glovebox and used as the counter electrode in a coin cell with a pristine electrode and a layer of blown micro fiber polypropylene (BMF, 3M) and Celgard separator material.

2.2.7 Electrochemical impedance spectroscopy (EIS)

The electrochemical impedance of a cell is measured by applying a small amplitude AC potential to an electrochemical cell and measuring the current that flows through the cell. The current is measured over a broad frequency range, and the current response within certain frequency ranges is used to determine the resistive, capacitive,

and inductive behavior of an electrochemical cell. The behavior in the different frequency ranges can be associated with various polarization losses. Electrochemical impedance spectroscopy (EIS) measurements were carried out with a two electrode coin cell assembly at room temperature with a Solartron SI1260 impedance analyzer by applying a 10 mV amplitude signal in the frequency range of 10 kHz to 0.001 Hz. In the EIS measurements, lithium foil served as the counter and reference electrodes. The impedance response was measured after zero, one, and 20 charge-discharge cycles at 2 V vs. Li/Li^+.

2.2.8 Tap density measurements

Tap density is a practical measurement of the volume that will be occupied per unit weight of the material. In a tap density test, a known weight of material is placed in a graduated cylinder, and then the graduated cylinder is tapped on a sturdy surface. After thousands of taps, the volume of material in the graduated cylinder is measured. Once the volume of material in the graduated cylinder stops changing, the final volume is recorded and the tap density is calculated knowing the weight of the material used. For this research, tap density measurements were made with a Quantachrome AT-4 Autotap equipment.

Chapter 3: Mo_3Sb_7-C Composite Anode Material

3.1 Introduction

With an aim to improve the cycle life of Sb-containing intermetallics, composites consisting of Mo_3Sb_7 and C were explored. The Mo_3Sb_7-C composites offer the following advantages as an anode material: (i) active antimony particles are constrained in the crystal structure of Mo_3Sb_7, which suppresses the agglomeration responsible for much of the capacity fade with antimony alloy electrodes and (ii) the carbon matrix surrounding the Mo_3Sb_7 particles acts as a buffer to alleviate the volume expansion. The Mo_3Sb_7-C composites are prepared by heating first antimony and molybdenum metals in a furnace to obtain Mo_3Sb_7 and then high-energy mechanical milling (HEMM) of the resulting Mo_3Sb_7 with carbon. Optimization of the cycle performance of Mo_3Sb_7-C was attempted through varying the type and wt. % of carbon present in the composite, as well as through the addition of MoO_2 into the composite. The ultrafine Mo_3Sb_7 particles dispersed in the carbon matrix are characterized by X-ray diffraction (XRD), transmission electron microscopy (TEM), scanning transmission electron microscopy (STEM), and electrochemical charge-discharge measurements including impedance analysis.

3.2 Experimental

The Mo_3Sb_7-C composite was prepared as described below. First, the Mo_3Sb_7 alloy powders were obtained by heating a mixture of required amounts of Sb (99.9 %, Aldrich) and Mo (99.8 %, Aldrich) powders at 780 ºC in a flowing 5 % H_2 atmosphere for 18 h. The Mo_3Sb_7 alloy obtained was then ground and sieved to eliminate particles over 100 μm. The Mo_3Sb_7 powder with particle size < 100 μm was then mixed with 20 wt. % acetylene black and subjected to high energy mechanical milling (HEMM) for 12 h at a speed of 500 rpm in a vibratory mill at ambient temperature under argon atmosphere

to obtain the Mo_3Sb_7-C composite. For a comparison, Mo_3Sb_7-C was also made with 20 wt. % Super P in place of acetylene black. The wt. % of carbon present in the Mo_3Sb_7-C composite was also varied between 20 and 30 wt. % Super P. The experiments to incorporate MoO_2 into the Mo_3Sb_7-C composite were carried out by heating a mixture of required amounts of Sb (99.9 %, Aldrich) and Mo (99.8 %, Aldrich), plus a 4 atom % excess of molybdenum powder at 780 ºC in a flowing argon atmosphere for 18 h. The Mo_3Sb_7 alloy obtained was then ground and sieved to eliminate particles over 100 μm. The Mo_3Sb_7 powder with particle size < 100 μm was then mixed with 20 wt. % acetylene black and subjected to high energy mechanical milling (HEMM) for 12 h at a speed of 500 rpm in a vibratory mill at ambient temperature under argon atmosphere.

The samples were characterized with a Phillips X-ray diffractometer with Cu Kα radiation, Hitachi S-5500 STEM, and JEOL 2010 TEM operating at 300 kV. The STEM and TEM samples were prepared by dispersing the sample in ethanol, depositing it dropwise onto a carbon-coated copper grid, and removing the ethanol at ambient temperature. Surface characterization was performed on Mo_3Sb_7-C powder made with 20 wt. % Super P with a Kratos X-ray photoelectron spectrometer (XPS) with a monochromatic Al Kα source. The electrodes for the electrochemical evaluation were prepared and tested according to details listed in chapter 2.2.6. Pouch lithium-ion cells consisting of the Mo_3Sb_7-C anode and a spinel manganese oxide cathode were also assembled and cycled at room temperature. To investigate the structural changes that may occur during electrochemical cycling, XRD data were collected on electrodes that had been cycled and then extracted from their cells.

Electrochemical impedance spectroscopic analysis (EIS) was conducted according to details contained in Chapter 2.2.7.

3.3 RESULTS AND DISCUSSION

3.3.1 Structural, morphological, and surface characterization

Figure 3.1 shows the XRD patterns of the Mo_3Sb_7 and Mo_3Sb_7-C samples. Both samples exhibit sharp peaks corresponding to crystalline Mo_3Sb_7 (JCPDS No. 019-0807), with a small peak corresponding to a trace amount of MoO_2 (JCPDS No. 032-0671), but without any peaks corresponding to Mo (JCPDS No. 004-0809), Sb (JCPDS No. 005-0562), or Sb_2O_3 (JCPDS No. 005-0543), confirming the formation of Mo_3Sb_7. Figure 3.2(a) shows the XRD pattern of the Mo_3Sb_7 sample that was synthesized in argon with 4 atom % excess molybdenum powder. The pattern clearly shows the characteristic peaks for Mo_3Sb_7 as well as prominent peaks for MoO_2. Figure 3.2(b) shows the Mo_3Sb_7-MoO_2 material after it has been ballmilled with 20 wt. % acetylene black. The MoO_2 phase is still present in the material, but the Mo_3Sb_7 phase has decomposed into Sb metal, and Mo metal. The decomposed product of Mo_3Sb_7-MoO_2 and carbon, following ballmilling, will be referred to as Sb-Mo-MoO_2-C, and is discussed in section 3.3.3.

The unit cell consists of four Mo_3Sb_7 groups with a total of 12 Mo, 12 Sb1, and 16 Sb2 atoms and a lattice parameter a = 9.5713 ± 0.0008 Å. Mo_3Sb_7 has the cubic Ir_3Ge_7 structure consisting of two interlocking face-condensed antiprisms [84], as shown in Figure 3.3. One of the interlocking antiprisms is formed by eight Sb2 atoms that surround each Sb1 atom. Each Sb1 atom is also surrounded by two tetrahedra; one tetrahedron is made up of four Mo atoms, and the other is made up of four Sb1 atoms. The other interlocking antiprism is a distorted square antiprism composed of a Mo atom coordinated to four Sb1 and four Sb2 atoms at the corners. In this structure, the Sb2 atoms are coordinated to three Mo atoms, one Sb2 atom, and six Sb1 atoms [85].

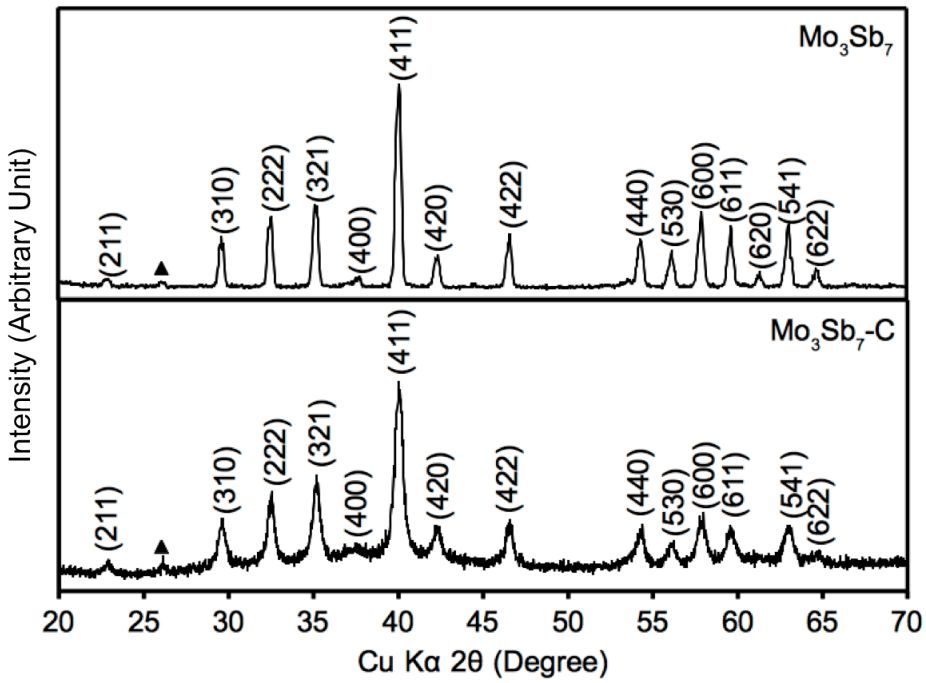

Figure 3.1. XRD patterns of the Mo_3Sb_7 and the Mo_3Sb_7-C composite. The reflections marked with a closed triangle correspond to the MoO_2 impurity phase.

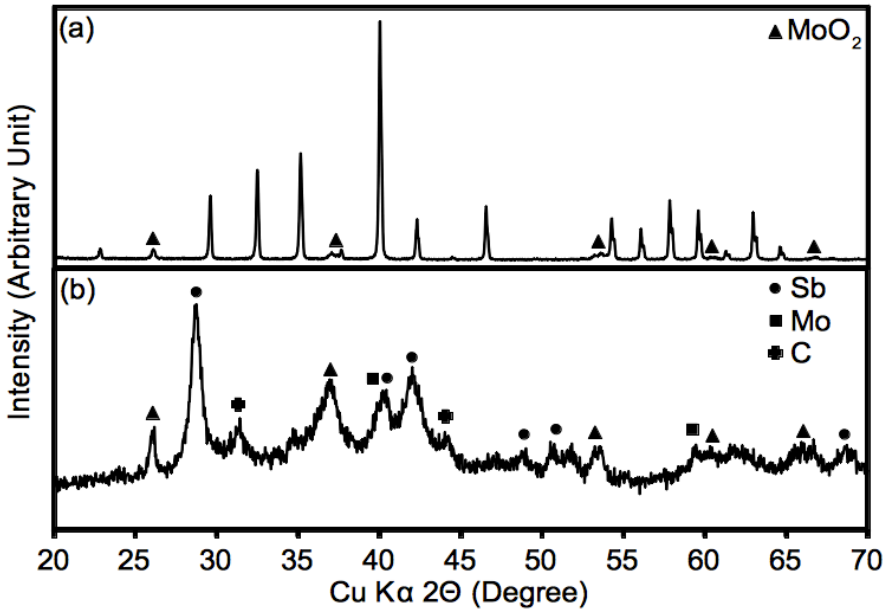

Figure 3.2. XRD patterns of the (a) Mo_3Sb_7-MoO_2 and (b) Sb-Mo-MoO_2-composites.

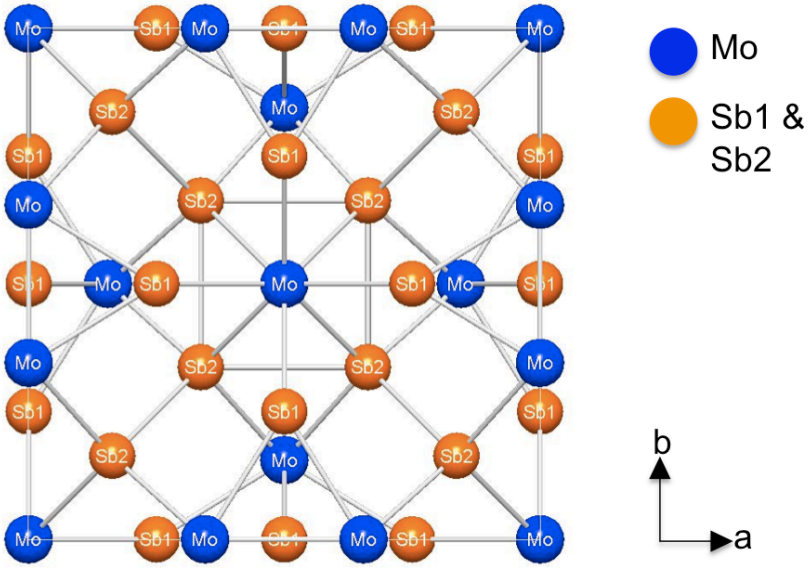

Figure 3.3. Crystal structure of Mo_3Sb_7. The three types of atoms in the structure are labeled as Sb1, Sb2, and Mo.

Figure 3.4 shows the TEM images of the Mo_3Sb_7-C composite. The TEM images and diffraction pattern of Mo_3Sb_7-C show the highly crystalline nature of the material. The STEM images shown in Figure 3.5 reveal the sub-micron particle size and a homogeneous distribution of Sb, Mo, and C in the Mo_3Sb_7–C composite. The SEM images of Mo_3Sb_7-C and acetylene in Figure 3.6 show the sub-micron particle size distribution in the composite material, as well as the homogenous distribution of carbon and Mo_3Sb_7.

In order to better characterize the Mo_3Sb_7-C material, XPS analysis was performed on the Mo_3Sb_7-C powder prepared with 20 wt. % Super P, and the results are shown in Figure 3.7. The binding energies of the $Sb_{5/2}$ and $Sb_{3/2}$ for Mo_3Sb_7-C are 530.9

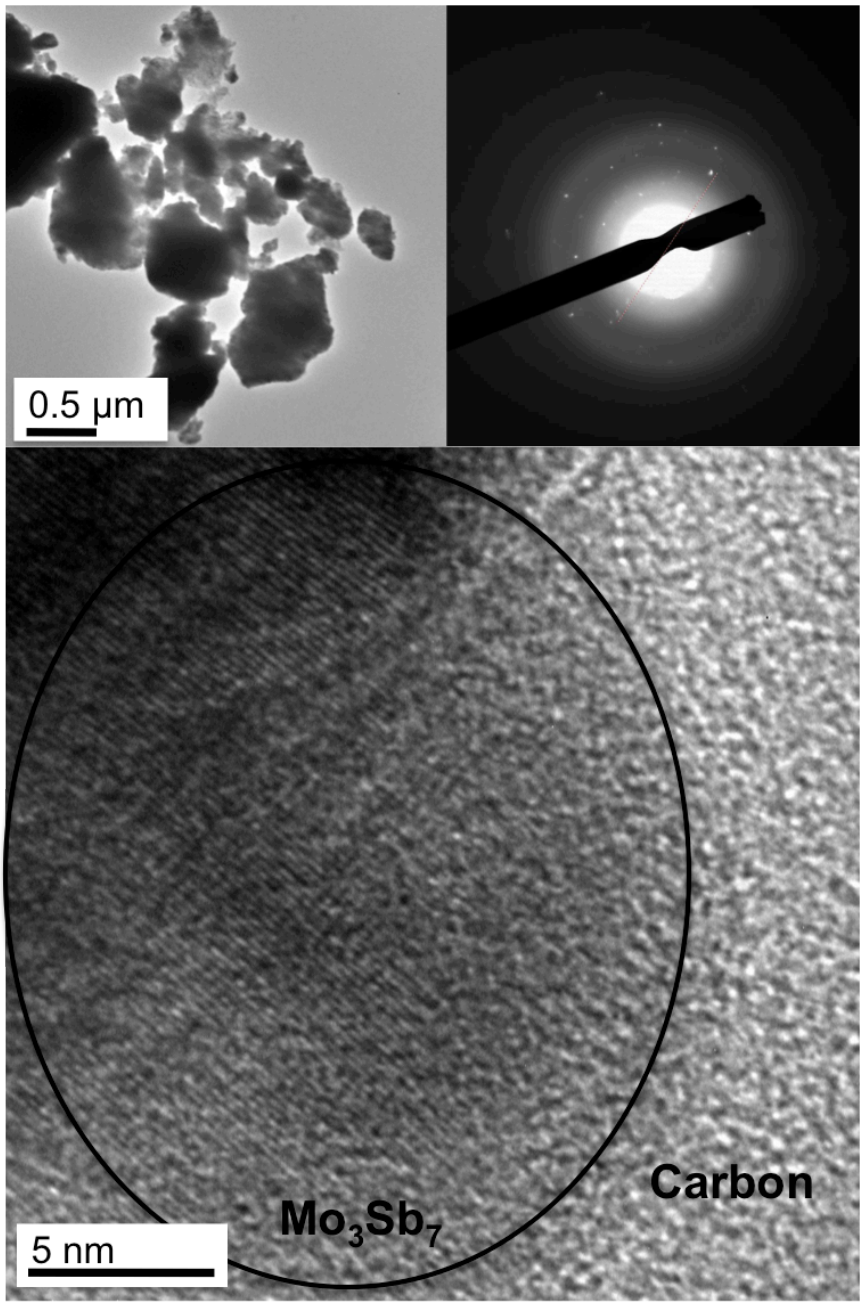

Figure 3.4. High-resolution TEM images of Mo_3Sb_7-C, showing the highly-crystalline nature of the material.

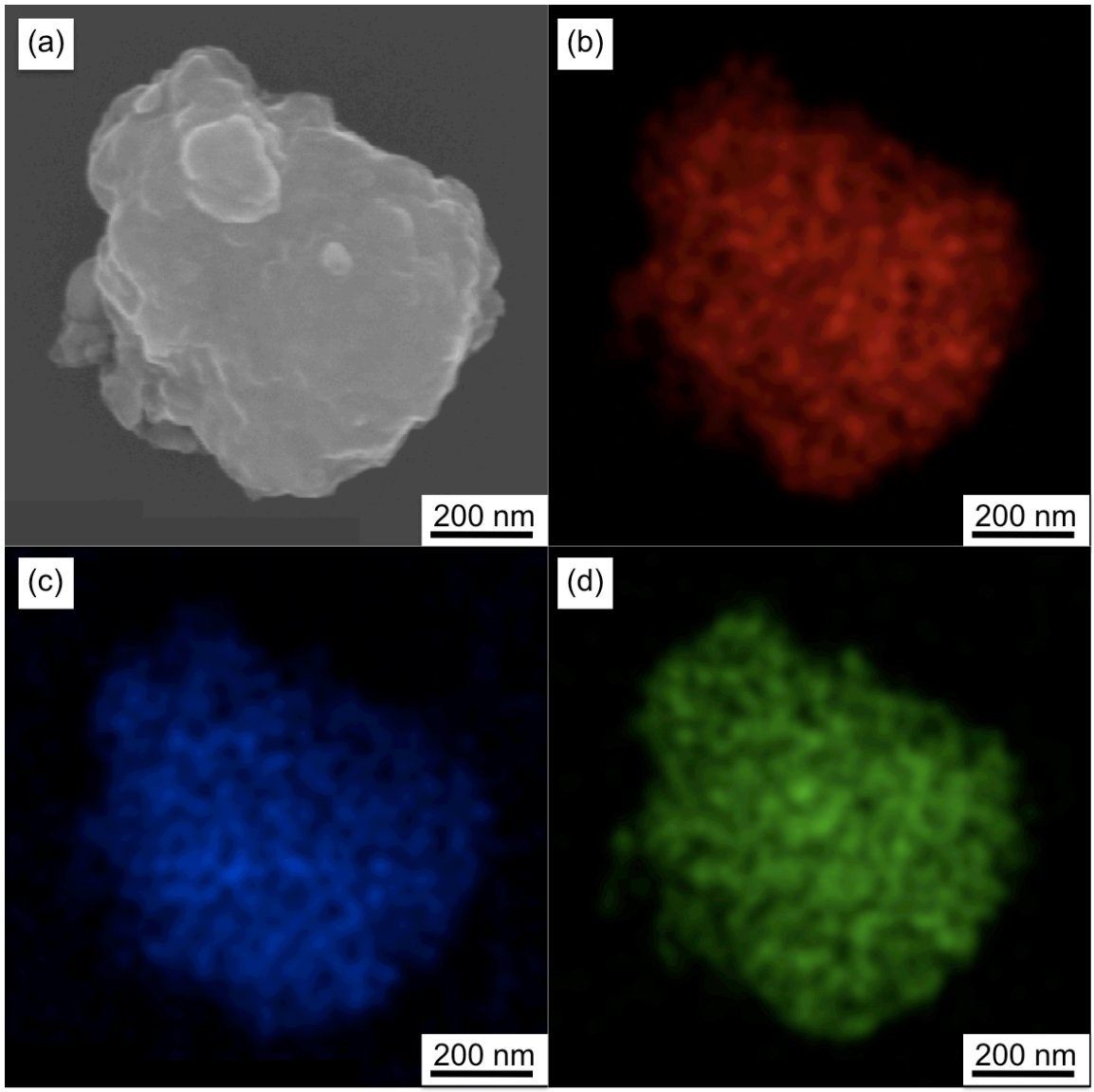

Figure 3.5. STEM image and elemental distribution in a Mo_3Sb_7-C particle: (a) SEM image, (b) distribution of Sb, (c) distribution of C, and (d) distribution of Mo.

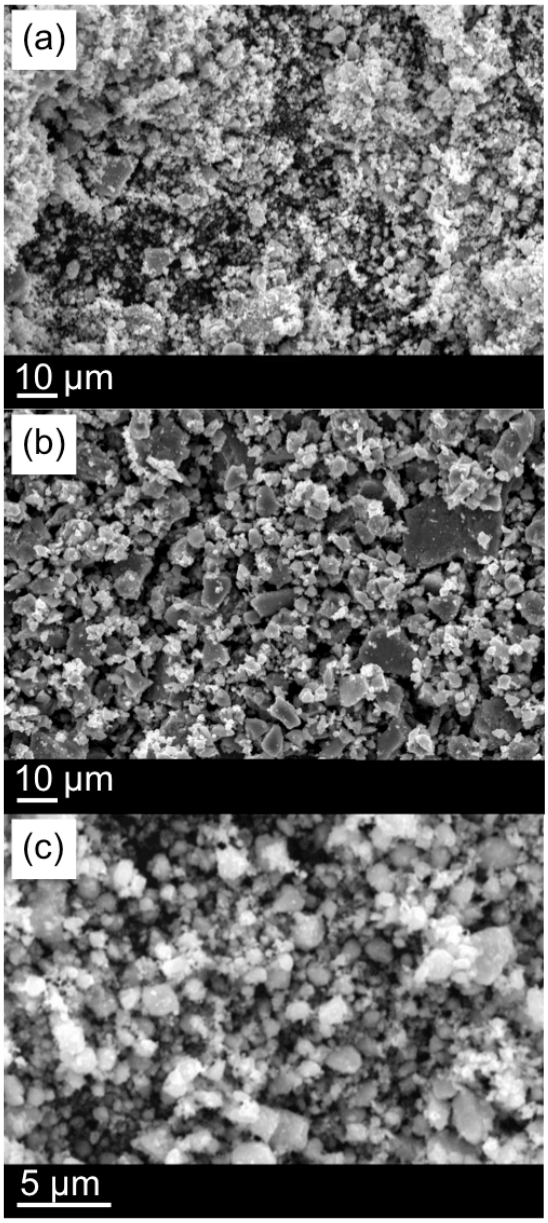

Figure 3.6. SEM images of (a) Mo_3Sb_7-C, (b) acetylene black, and (c) Mo_3Sb_7-C.

eV and 540.4 eV, respectively. This compares to the $Sb_{5/2}$ peak for Sb metal, which is 528.3 eV. The shift in the $Sb_{5/2}$ binding energy indicates the absence of free metallic Sb. The Sb 3d spectrum overlaps with the O 1s spectrum region, but any oxygen present

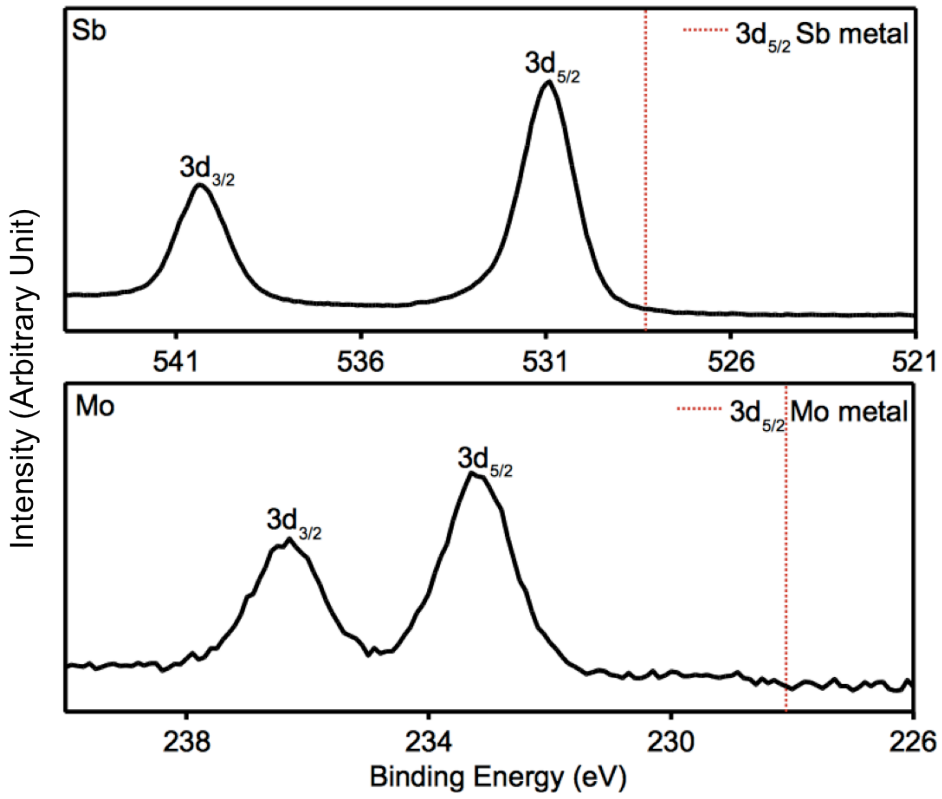

Figure 3.7. Sb 3d and Mo 3d XPS spectra of the Mo_3Sb_7-C powder.

would be observed around 532 eV, so this sample does not seem to show the presence of any oxygen. The binding energies of the $Mo_{5/2}$ and $Mo_{3/2}$ for Mo_3Sb_7-C are 232.8 eV and 235.8 eV, respectively. This compares to the $Mo_{5/2}$ peak for Mo metal, which is 228.1 eV. Because there is only one set of peaks for both Sb and Mo, the material appears to be single-phase Mo_3Sb_7. Mo_3Sb_7 has not been studied extensively, and so the XPS information obtained about this single-phase sample is useful as part of the standard body of data on Mo_3Sb_7.

3.3.2 Electrochemical characterization

The voltage profile and differential capacity plot of the Mo_3Sb_7-C composite are shown in Figure 3.8. The composite exhibits first discharge and charge capacities of 736 and 606 mAh/g, respectively, implying an irreversible capacity loss of 130 mAh/g and a coulombic efficiency of 82% in the first cycle for the composite. The irreversible capacity loss may be largely associated with the reduction of the electrolyte on the active material surface and the formation of solid-electrolyte interfacial (SEI) layer [1]. The major peaks in the differential capacity plot (Fig. 3.8(b)), around 0.8 V vs. Li/Li^+ for alloying and around 1.0 V vs. Li/Li^+ for dealloying, correspond to the reaction of lithium with antimony. The electrochemical reaction between amorphous carbon and lithium appears as a broad peak below 0.2 V vs. Li/Li^+ [14].

In order to investigate the structural changes that occur during electrochemical cycling, XRD data were collected on electrodes that had been cycled and then extracted from the cells. XRD patterns recorded with electrodes discharged to 0.45 V vs. Li/Li^+, fully discharged electrodes, and fully charged electrodes are shown in Figure 3.9. The data indicate the complete disappearance of the crystalline Mo_3Sb_7 phase at 0.45 V vs. Li/Li^+, followed by the appearance of Li_3Sb when the electrode is in the fully-discharged state. When the electrode is then fully-charged, the crystalline Mo_3Sb_7 phase reappears. If the Mo is extruded as Mo metal from Mo_3Sb_7 during the discharge process as with other antimony-based alloy anode materials [35,86], then the XRD pattern would be expected to show peaks for Mo metal along with that for Li_3Sb in Figure 3.9(c). However, Figure 3.9(c) does not show any peaks for Mo metal, suggesting either the Mo atoms remain in the framework of Li_3Sb or extruded as amorphous Mo metal.

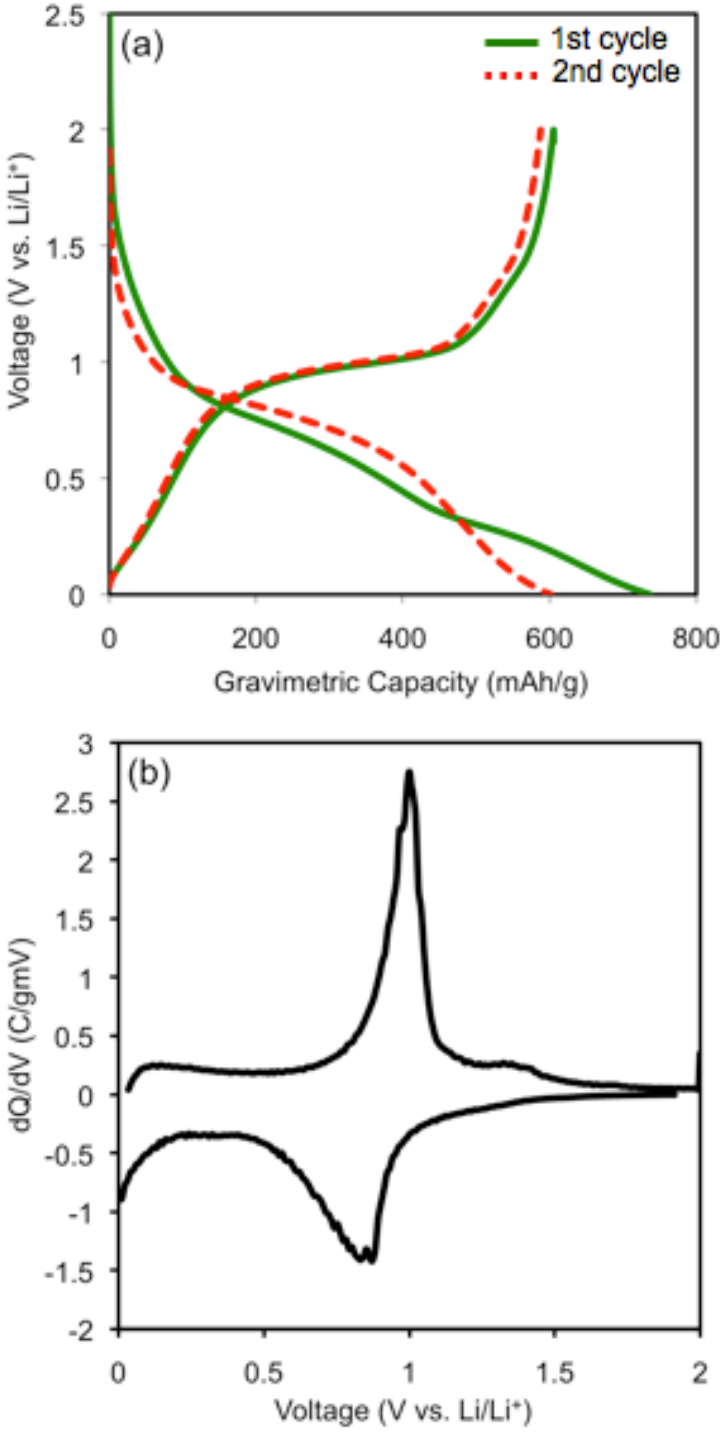

Figure 3.8. (a) Voltage profile and (b) differential capacity plot for Mo_3Sb_7-C.

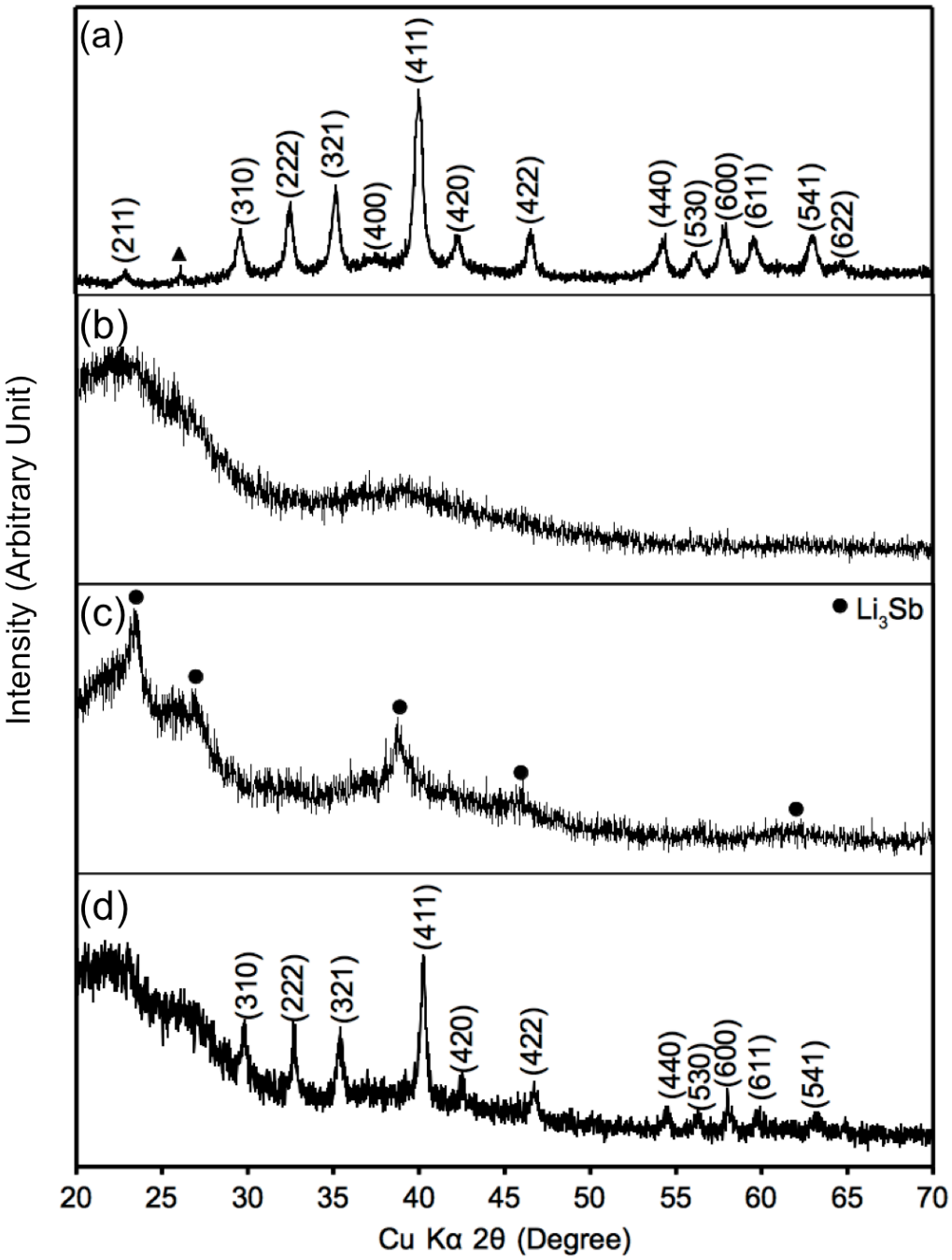

Figure 3.9. XRD patterns of (a) pristine Mo_3Sb_7-C, and electrodes that have been (b) discharged to 0.45 V vs. Li/Li^+, (c) fully discharged (Li-insertion), and (d) fully charged (Li-extraction). The reflections marked with a closed triangle correspond to the MoO_2 impurity phase.

Figure 3.10 compares the cyclability of Mo_3Sb_7, Mo_3Sb_7-C, and graphite at 0 – 2 V vs. Li/Li^+, at a current of 100 mA/g active material. While Mo_3Sb_7 exhibits drastic capacity fade after 20 cycles, the Mo_3Sb_7-C composite exhibits excellent cyclability to 70 cycles. Clearly, the addition of carbon to the Mo_3Sb_7 alloy improves the cycle performance significantly by acting as a conductive buffer to the volume changes during cycling. However, the capacity of the sample begins to fade around 70 cycles. Although the gravimetric capacity of the Mo_3Sb_7-C anode is less than two times of commercially available graphite (Figure 3.10), the volumetric capacity is approximately three times that of graphite due to the much higher tap density (1.75 g/cm^3) compared to that of graphite

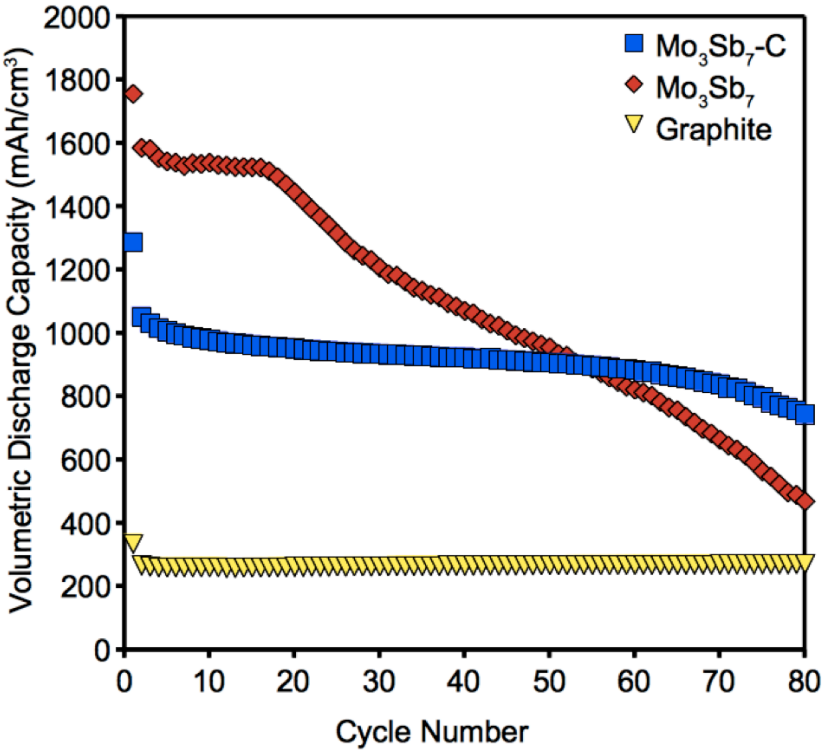

Figure 3.10. Comparison of the cyclability of Mo_3Sb_7, Mo_3Sb_7-C, and graphite at 0 - 2 V vs. Li/Li^+ at a current of 100 mA/g active material.

(~ 1 g/cm^3). Figure 3.11 compares the rate capability of the Mo_3Sb_7-C composite with that of graphite. Although the volumetric capacity is higher, the Mo_3Sb_7-C composites exhibit lower rate capability than graphite. Nevertheless, further optimization could improve the rate capability.

Full pouch cells were also assembled with the Mo_3Sb_7-C composite as the anode and the spinel manganese oxide cathode. The objective of testing Mo_3Sb_7-C with spinel manganese oxide cathode is to determine the resistance of the Mo_3Sb_7-C electrode to

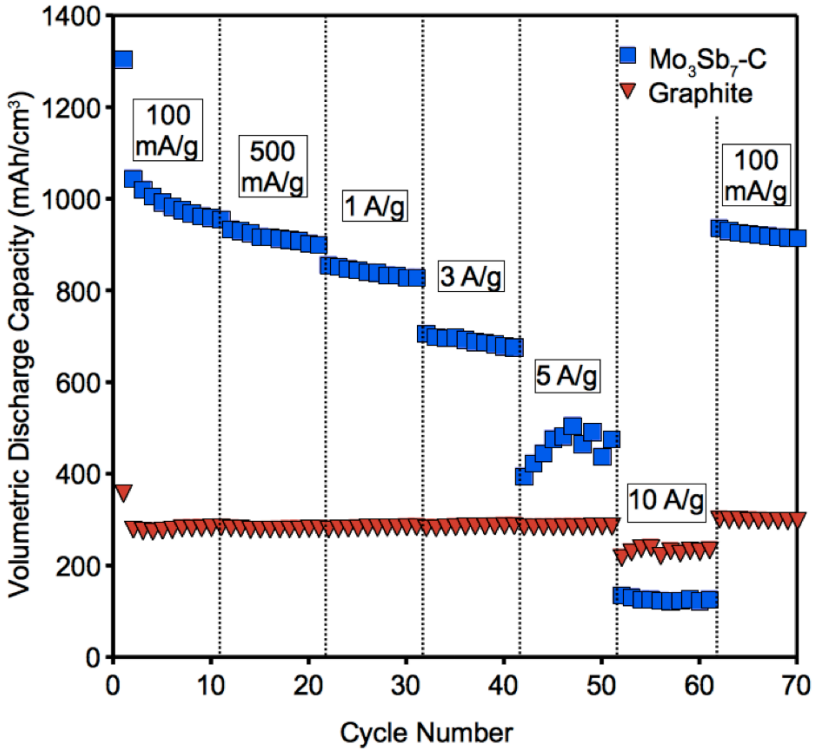

Figure 3.11. Rate capability data of Mo_3Sb_7-C as compared to that of graphite. Charge rates are calculated as current per gram of active electrode material. Cycling was performed at 0 - 2 V vs. Li/Li$^+$.

poisoning by the dissolved Mn from the spinel cathode. Manganese poisoning of the carbon anodes is one of the major issues of spinel manganese cathodes. The full cell with the Mo_3Sb_7-C anode and manganese oxide spinel cathode shows good cyclability over 100 cycles, indicating the resistance of the Mo_3Sb_7-C composite to manganese poisoning (Fig. 3.12). The slight difference in performance between the coin cell and the full pouch

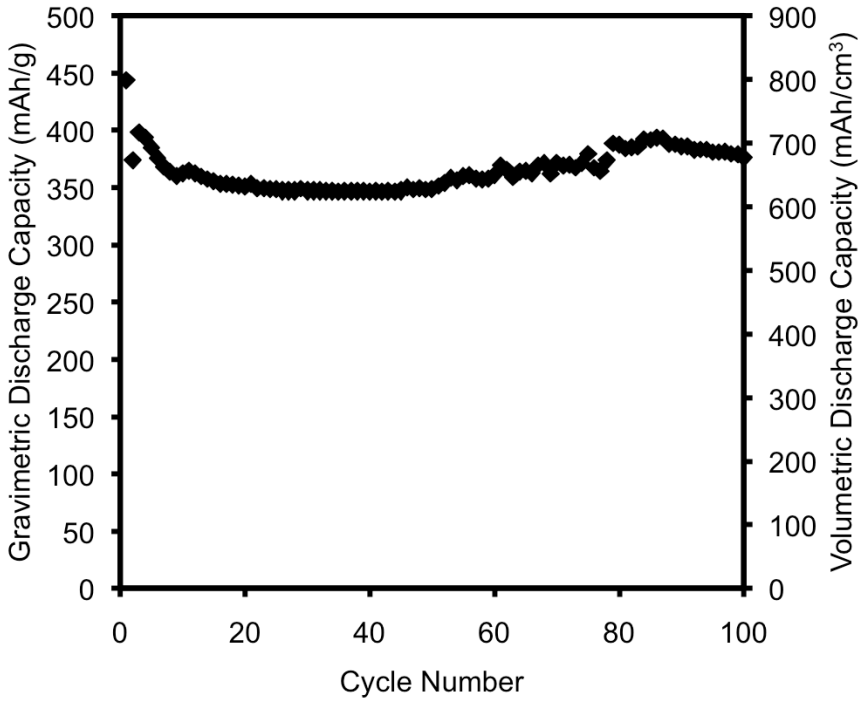

Figure 3.12. Cycle performance of a full cell with Mo_3Sb_7-C anode and the spinel manganese oxide cathode at a current rate of 30 mA/g active material.

cell after 70 - 80 cycles could be related to the differences in our construction of the cells and the extent of compression and contact.

In an effort to improve the cycle performance of the Mo_3Sb_7-C composite material, the type of carbon used in the composite and the amount of carbon used in the composite was varied. Super P has been used quite extensively to improve the electrical

conductivity of anode materials in electrode preparation, and so it was chosen as a substitute for acetylene black in the ballmilling preparation of Mo_3Sb_7-C. Figure 13 shows the cycle performance of Mo_3Sb_7-C made with 20 % acetylene black as compared with the cycle performance of Mo_3Sb_7-C made with 20 % Super P. The introduction of

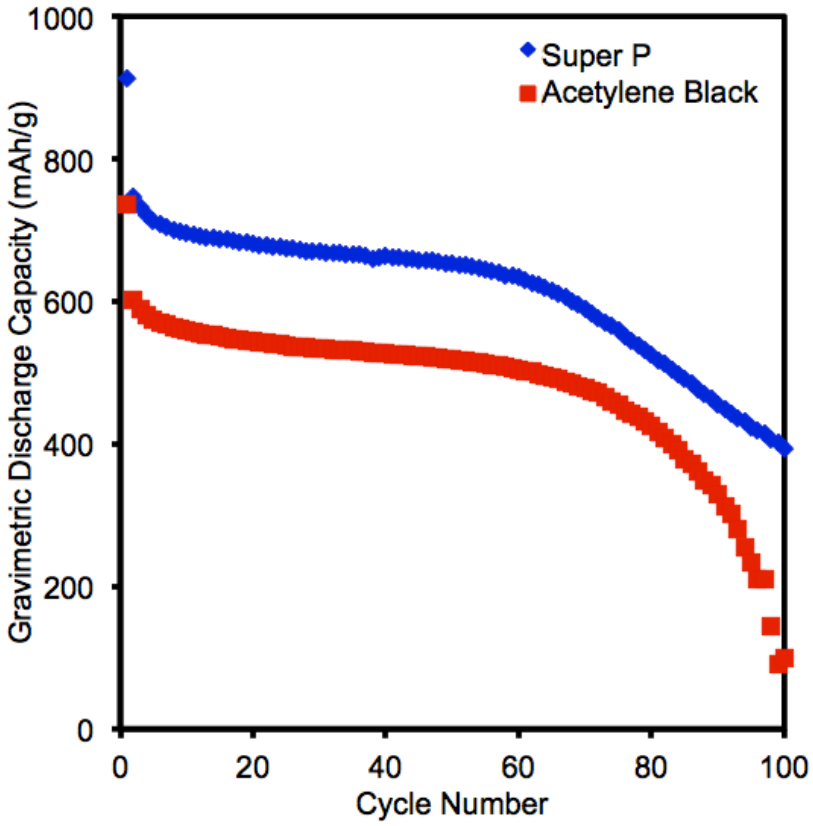

Figure 3.13. Comparison of the cyclability of Mo_3Sb_7-C with Super P and acetylene black as the carbon from 0 - 2 V vs. Li/Li^+ at a current of 100 mA/g active material.

Super P into the composite rather than acetylene black had a significant impact on the cycle performance. The Mo_3Sb_7-C made with 20 % Super P showed a 25 % increase in gravimetric discharge capacity, and a leveling out of the severe capacity fade that begins around cycle 80 with the Mo_3Sb_7-C made with 20 % acetylene black. Based upon this

result, it is thought that the improved electrical conductivity of the Mo_3Sb_7-C made with 20 % Super P is contributing to the electrochemical efficiency of the reaction with lithium.

To further build upon the gains made by substituting Super P for acetylene black, a comparison in cycle performance was made between Mo_3Sb_7-C made with 20 % Super P and Mo_3Sb_7-C made with 30 % Super P. Though an increase in carbon content was expected to decrease the density and capacity of the material, an improvement in the long-term cyclability of the Mo_3Sb_7-C electrode would be worth the detrimental effects on the discharge capacity. Figure 3.14 shows the comparison of Mo_3Sb_7-C made with 20 % Super P and Mo_3Sb_7-C made with 30 % Super P. The effect of increasing the amount of Super P present in the Mo_3Sb_7-C is significant. Mo_3Sb_7-C made with 20 % Super P experiences dramatic capacity fade upon extended cycling and only retains 14 % of its second cycle discharge capacity by the 200th cycle. Mo_3Sb_7-C made with 30 % Super P retains 59 % of its second cycle discharge capacity at the 200th cycle. The gravimetric discharge capacity of the Mo_3Sb_7-C made with 30 % Super P (520 mAh/g) is lower than when only 20 % Super P is used, but the gains in cycle performance far outweigh the decrease in capacity. It is possible that with further experimentation and testing, an optimal amount of Super P could be chosen so that the reduction in discharge capacity is minimized, while the cycle life improvement is maintained. Additionally, there are many other types of conductive carbon that could be chosen to replace Super P in the Mo_3Sb_7-C composite. Further exploration into the optimization of Mo_3Sb_7-C is needed, as there is still room for improvement.

In order to further improve the performance of the Mo_3Sb_7-C, the incorporation of MoO_2 was attempted. Mo_3Sb_7-MoO_2 was made by changing the synthesis conditions and

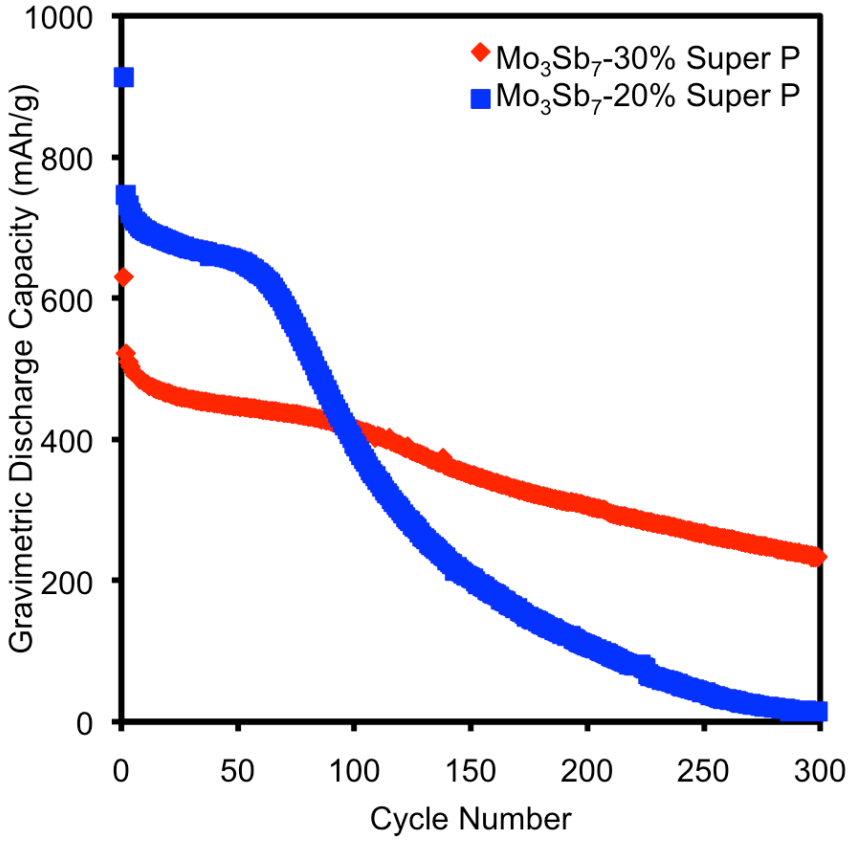

Figure 3.14. Comparison of the cyclability of Mo_3Sb_7-C with 20 and 30 wt. % Super P from 0 - 2 V vs. Li/Li^+ at a current of 100 mA/g active material.

introducing a 4 atom % excess of molybdenum metal powder into the precursors. Although the Mo_3Sb_7-MoO_2 composite decomposes on ballmilling with carbon, the cycle performance of the resultant Sb-Mo-MoO_2-C material is more stable than that of Mo_3Sb_7-C. Figure 3.15 shows a comparison of the room temperature cycle performance of Sb-Mo-MoO_2-C, Mo_3Sb_7-C, and commercial graphite. After 200 cycles, the Sb-Mo-MoO_2-C material has retained 60 % of the second cycle volumetric discharge capacity, and still has more than twice the volumetric capacity of commercial graphite. To explore the differences between the Sb-Mo-MoO_2-C material and Mo_3Sb_7-C, the voltage profile and corresponding differential capacity plot for Sb-Mo-MoO_2-C were examined (Fig. 3.16).

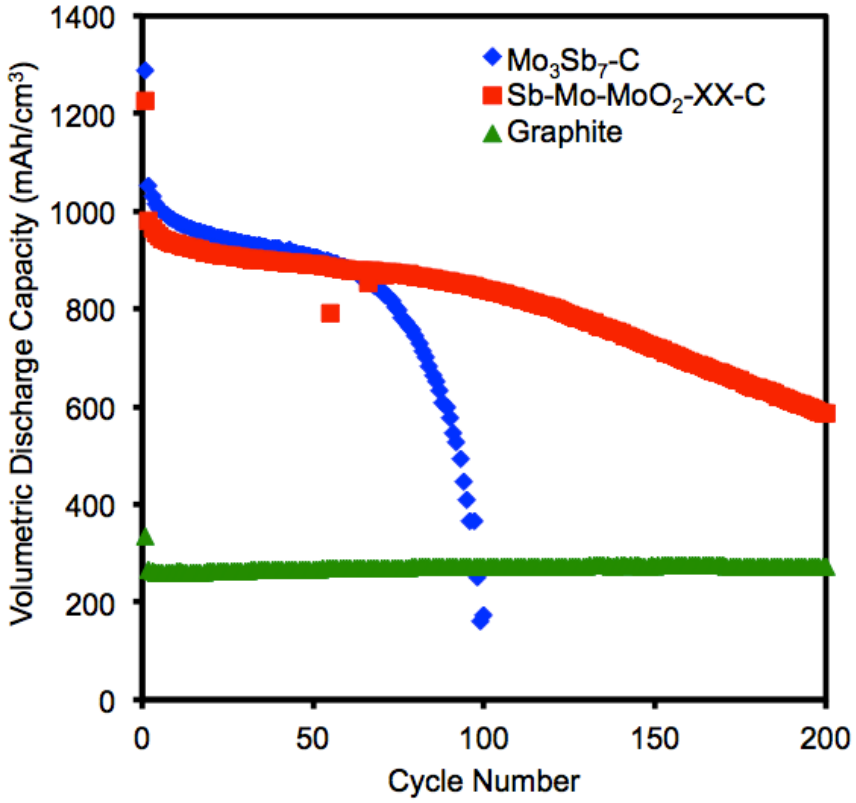

Figure 3.15. Comparison of the cyclability of Mo_3Sb_7-C, Sb-Mo-MoO_2-C, and graphite from 0 - 2 V vs. Li/Li^+ at a current of 100 mA/g active material.

The differential capacity plot for Sb-Mo-MoO_2-C shows a feature that is not present on the differential capacity plot for Mo_3Sb_7-C. The discharge portion of the first cycle curve in Figure 3.16(b) shows one peak at 0.77 V vs. Li/Li^+. During the second cycle, there are two peaks present in the discharge portion of the curve. The second cycle discharge peaks occur at 0.87 and 0.74 V vs. Li/Li^+. The presence of two peaks indicates two separate reactions occurring between Sb-Mo-MoO_2-C and lithium during the first cycle. However during extended cycling, the peak at around 0.74 V vs. Li/Li^+ begins to decrease in area and has disappeared by the 100^{th} cycle. During each charge cycle, only

one peak is present in the charge portion of the differential capacity plot at 1.03 V vs. Li/Li^+. Because the discharge curve contains an extra peak that disappears during cycling, and the charge curve only contains one peak, it was concluded that an irreversible reaction takes place between Sb-Mo-MoO_2-C and lithium after the first cycle. Since the SEI layer can form around 0.8 V vs. Li/Li^+ and Sb reacts with lithium between 0.7 – 0.9 V vs. Li/Li^+, it is possible that during the first cycle, the DCP peaks associated with lithiation of Sb are masked by the DCP peak due to the decomposition of the electrolyte and SEI layer formation.

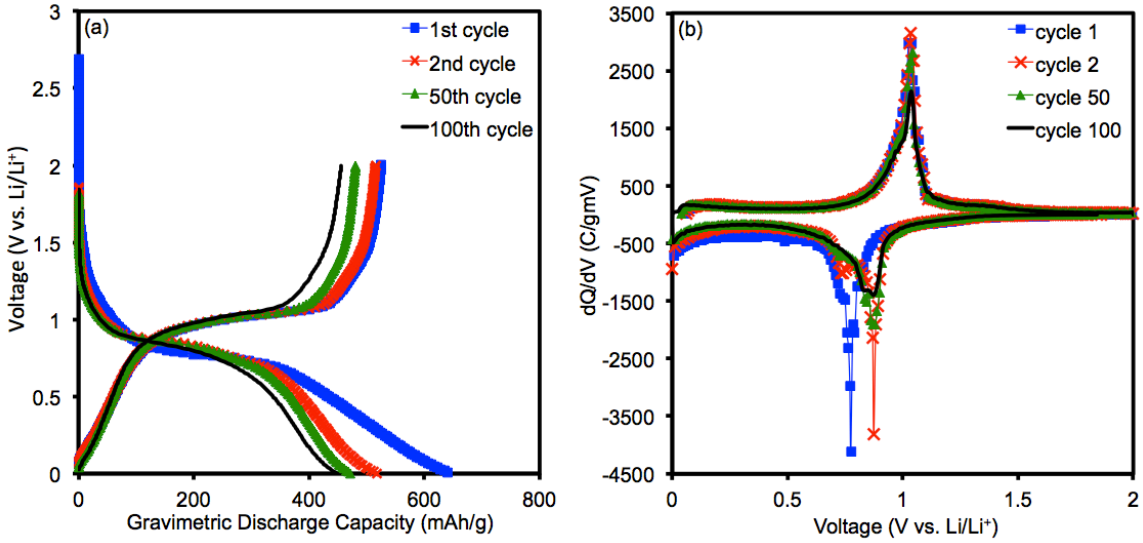

Figure 3.16. (a) Voltage profile and (b) differential capacity plot for Sb-Mo-MoO_2-C.

To gain insight into the electrochemical performance of Mo_3Sb_7 and Mo_3Sb_7-C, EIS measurements were conducted at 2 V vs. Li/Li^+ before cycling, after the 1st cycle, and after the 20th cycle. The EIS data were analyzed based on an equivalent circuit given in Figure 3.17 [87]. In Figure 3.17, R_u refers to uncompensated resistance between the working electrode and the lithium reference electrode, CPE_s refers to the constant phase

element of the surface layer, R_s refers to the resistance of the SEI layer, CPE_{dl} refers to the constant phase element of the double layer, R_{ct} refers to the charge-transfer resistance, and Z_w refers to the Warburg impedance. Generally, the EIS spectrum can be divided into three frequency regions, *i.e.*, low-frequency, medium-to-low- frequency, and high-

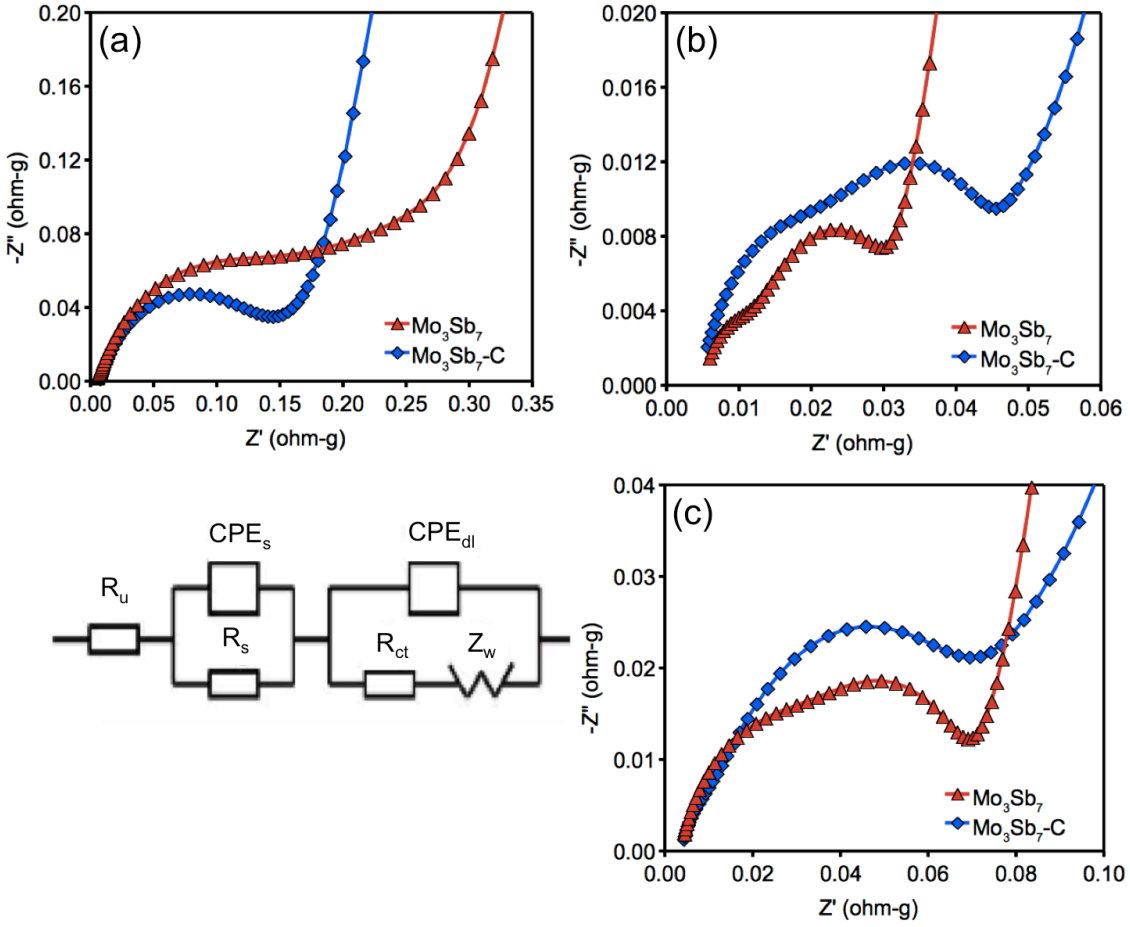

Figure 3.17. The equivalent circuit used for the Mo_3Sb_7 and Mo_3Sb_7-C composites and EIS plots of the Mo_3Sb_7 and Mo_3Sb_7-C composite materials: (a) before cycling, (b) after the 1st cycle, and (c) after the 20th cycle.

frequency regions, which correspond, respectively, to the geometric capacitance of the cell, the charge-transfer reaction, and the lithium-ion diffusion through the surface layer.

The EIS spectra recorded before cycling in Figure 3.17 consists of one semicircle and a line. After the 1st cycle and the 20th cycle, the EIS spectra in Figure 3.17 consist of two semicircles and a line. The diameter of the semicircle in the high-frequency region (lowest Z' values) is a measure of the resistance R_s of the SEI layer, but is not observed for either material before cycling has been performed. The diameter of the semicircle in the medium-frequency region (middle Z' values) is a measure of the charge-transfer resistance R_{ct}, which is related to the electrochemical reaction between the particles or between the electrode and the electrolyte. The portion of the impedance curve that has a linear slope is related to lithium-ion diffusion in the bulk of the active material.

Before cycling, the Mo_3Sb_7 sample exhibits a higher R_{ct} and bulk diffusion resistance than the Mo_3Sb_7-C sample. The semicircle corresponding to R_s cannot be observed in the impedance measurements before cycling. After the first cycle, both the samples exhibit two distinct semicircles, corresponding to R_s and R_{ct}. The Mo_3Sb_7-C sample shows higher R_s than Mo_3Sb_7, due to the development of the SEI layer. The growth of the SEI layer is more pronounced in the Mo_3Sb_7-C sample, most likely because of the carbon. The effects of a more significant SEI layer can also be seen in the larger first cycle irreversible capacity loss for Mo_3Sb_7-C compared to that for the Mo_3Sb_7 sample (Figure 3.10). R_{ct} and the bulk diffusion resistance of the Mo_3Sb_7-C sample are higher than those of Mo_3Sb_7 after the first cycle, presumably because the Mo_3Sb_7 particles are not separated from one another by carbon. After the 20^{th} cycle, the bulk diffusion resistance of the Mo_3Sb_7 sample becomes greater than that of the Mo_3Sb_7-C sample because the Mo_3Sb_7 electrode has already begun breaking down and encountering significant capacity fade.

3.3.3 TEM and XRD of cycled electrodes

In order to better understand the source of the capacity fade in the Mo_3Sb_7-C sample, XRD and high-resolution TEM were performed on electrode materials that had been cycled for greater than 100 cycles and showed severe capacity fade. Figure 3.18 shows the XRD patterns of Mo_3Sb_7-C after one cycle and after 111 cycles. After one cycle (Figure 3.18(a)), peaks for crystalline Mo_3Sb_7 are present in the XRD pattern. After 111 cycles (Figure 3.18(b)), no peaks for crystalline Mo_3Sb_7 are observed. From the TEM images in Figure 3.19, small regions of crystalline Mo_3Sb_7 are detected, but are smaller and more isolated from one another than in the uncycled Mo_3Sb_7-C sample. It is suggested that the capacity fade observed with Mo_3Sb_7-C at higher number of cycles is

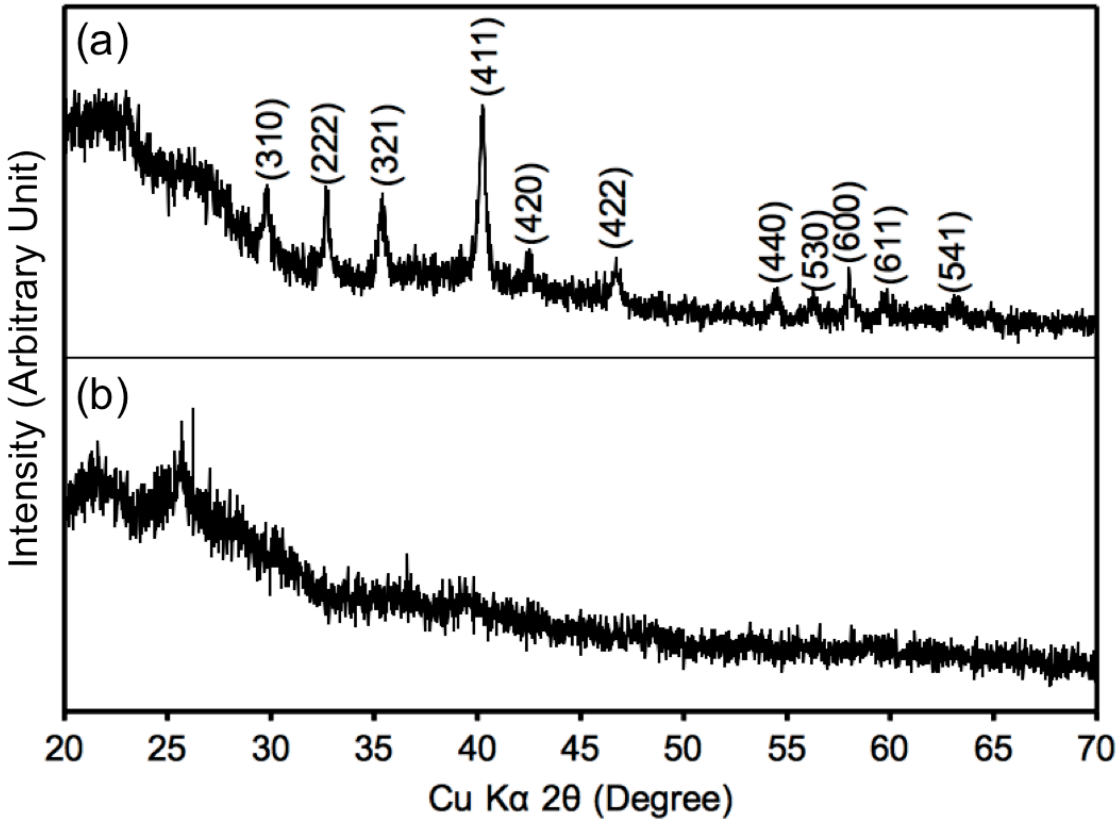

Figure 3.18. XRD patterns of Mo_3Sb_7-C after (a) 1 cycle and (b) 111 cycles.

due to the breaking and separation of the large crystalline Mo_3Sb_7 particles that are present before cycling.

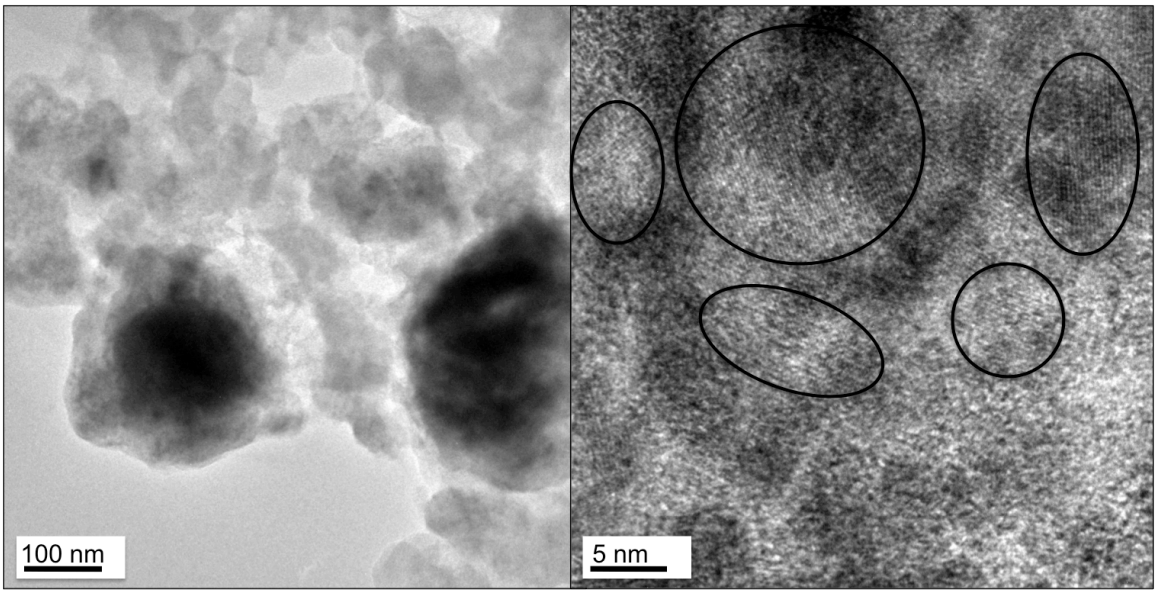

Figure 3.19. High-resolution TEM images of Mo_3Sb_7-C after 111 charge-discharge cycles. The circles highlight isolated regions of crystalline Mo_3Sb_7 that are smaller than the crystalline regions present in the uncycled Mo_3Sb_7-C material.

3.4 CONCLUSIONS

Mo_3Sb_7-C composite has been investigated as an anode material for lithium-ion batteries. Characterization data collected on Mo_3Sb_7-C with XRD, TEM, and STEM reveal a highly crystalline Mo_3Sb_7 dispersed within the conductive carbon matrix. The presence of carbon greatly improves the cycle performance of Mo_3Sb_7 by buffering the volume changes occurring during charge-discharge cycling. The Mo_3Sb_7-C composite anode exhibits higher discharge capacity (518 mAh/g and 907 mAh/cm^3) than graphite anode. With a higher discharge capacity and a tap density of 1.75 g/cm^3, the Mo_3Sb_7-C composite offers nearly three times higher volumetric energy density than graphite.

However, the Mo_3Sb_7-C composite begins to exhibit capacity fade at around 70 cycles. During the optimization work with Mo_3Sb_7-C, it was determined that the performance could be improved through the use of 30 wt. % Super P. The discharge capacity of the Mo_3Sb_7-C material with 30 wt. % Super P was lower than other samples, but the material had better cycle performance than any other Mo_3Sb_7-C that was synthesized. Building on prior research findings that showed the benefit of adding oxides to antimony-based composites [34], Mo_3Sb_7-MoO_2 was synthesized. However, Mo_3Sb_7-MoO_2 decomposes during ballmilling with carbon. The result of the decomposition is Sb-Mo-MoO_2-C, a multi-phase material that shows exceptional volumetric capacity and good cycle life. More investigation into the exact composition and properties of the Sb-Mo-MoO_2-C material may enable materials with performance that is even more applicable for use in lithium-ion batteries.

Chapter 4: Cu_2Sb-Al_2O_3-C Nanocomposite Anode Material

4.1 INTRODUCTION

This chapter focuses on the synthesis, characterization, and electrochemical testing of the nano-engineered Cu_2Sb-Al_2O_3-C composite anode. The Cu_2Sb-Al_2O_3-C nanocomposite offers several advantages: (i) the Al_2O_3-C ceramic and carbon matrix act as a buffer to absorb the volume expansion that occurs in the nanosized copper-antimony metal alloy particles, (ii) the Al_2O_3 and carbon matrix keeps the Cu_2Sb particles separate during cycling, thereby reducing agglomeration, (iii) Cu_2Sb-Al_2O_3-C is prepared by a simple, one step, high-energy mechanical milling (HEMM) synthesis of Sb_2O_3 with Al, Cu and C, and (iv) an operating voltage well above that of Li/Li^+ and the presence of Al_2O_3 on the Cu_2Sb particles during the ball-milling process can suppress the formation of an SEI layer [34]. Additionally, the higher operating voltage and the suppression of SEI layer formation prevent lithium plating and enhance safety. Accordingly, the Cu_2Sb-Al_2O_3-C material is investigated here by X-ray diffraction (XRD), transmission electron microscopy (TEM), X-ray photoelectron spectroscopy (XPS), scanning electron microscopy (SEM), and electrochemical charge/discharge measurements including impedance analysis.

4.2 EXPERIMENTAL

The Cu_2Sb-Al_2O_3-C nanocomposite was synthesized by a reduction of Sb_2O_3 (99.6 %, Alfa) with aluminum (99.97 %, 17 μm, Alfa) and formation of Cu_2Sb with copper (99 %, 45 μm Acros Organics) metal powder in the presence of carbon (acetylene black) by a high-energy mechanical milling process, as illustrated below by reaction 1:

$$Sb_2O_3 + 2Al + 4Cu \rightarrow 2Cu_2Sb + Al_2O_3 \quad (\Delta G^o = -1023 \text{ kJ/mol}) \qquad (4.1)$$

The overall negative free-energy change makes the reduction reaction (4.1) spontaneous. The required quantities of Sb_2O_3, Al, and Cu were mixed with acetylene black in an Sb_2O_3-Al-Cu : C weight ratio of 80 : 20. The Cu_2Sb-C nanocomposite material without Al_2O_3 was obtained through a two-step process: (i) stoichiometric amounts of Cu and Sb were ball milled to form Cu_2Sb, and (ii) the resultant Cu_2Sb powder was ball milled with 20 wt. % acetylene black to form the Cu_2Sb-C nanocomposite. In order to determine the optimum amount of carbon in the composite, reactions were also performed with Sb_2O_3-Al-Cu : C in weight ratios of 85 : 15 and 90 : 10. Cu_2Sb-Al_2O_3 was synthesized by milling Sb_2O_3, Al, and Cu in the proper stoichiometric ratio. All HEMM steps were carried out in a planetary ball mill (Fritsch Pulverisette 6 planetary mill) at a speed of 500 rpm at ambient temperature under argon atmosphere in hardened steel vials having an 80 cm^3 capacity with steel balls (diameter: 1/2 and 1/4 in.) in a ball : powder weight ratio of 20 : 1. The vials were sealed inside an argon-filled glovebox prior to milling. The standard milling time was 12 h, but for one set of experiments on Cu_2Sb-Al_2O_3-C with 20 wt. % acetylene black, the milling time was 24 h.

The phase analysis of the synthesized samples was performed with a Phillips XRD system with Cu Kα radiation. The morphology, microstructure, and composition of the synthesized powders were examined with a JEOL JSM – 5610 scanning electron microscope (SEM) system and a JEOL 2010F transmission electron microscopy (TEM) system. Surface characterization was performed on an uncycled Cu_2Sb-Al_2O_3-C electrode and Cu_2Sb-Al_2O_3-C powder that had been milled for 12 h and 24 h. The surface characterization was carried out with a Kratos X-ray photoelectron spectrometer (XPS) with a monochromatic Al Kα source. The uncycled Cu_2Sb-Al_2O_3-C electrode was extracted from a coin cell in an argon-filled glovebox and transferred into the XPS

chamber via an argon-filled capsule built at the Surface Analysis Laboratory of the Texas Materials Institute (TMI) at UT-Austin. The surface of the electrode was cleaned of surface oxides and electrolyte salts by sputtering with a 4 keV beam energy and an extractor current of 75 μA for 5.5 min.

The electrodes for the electrochemical evaluation were prepared and tested according to details listed in chapter 2.2.6. The majority of the charge/discharge experiments were performed galvanostatically at a constant current density of 100 mA/g of active electrode material within a desired voltage range. Some charge/discharge experiments were carried out at 5 mA/g of active electrode material in order to allow for equilibrium in the reaction mechanism. Additionally, multi-rate testing was performed at currents in the range of 100 mA/g to 5 A/g of active electrode material. Cycle testing was also performed in various voltage ranges in order to determine if any of the reactions taking place during lithiation/delithiation were irreversible. In order to investigate any structural changes that occurred during electrochemical cycling, XRD data were collected from electrodes that had been detached from cycled cells and covered with polyimide tape as a protective film. TEM was used to observe changes in crystallinity and morphology of cycled electrodes.

Electrochemical impedance spectroscopic analysis (EIS) was conducted according to the methods listed in chapter 2.2.7. The impedance response was measured after different numbers of charge-discharge cycles (after 0, 1, and 20 cycles) at 2 V vs. Li/Li^+. Tap density measurements were made with a Quantachrome AT-4 Autotap machine. Electrochemical cycle testing at 25 ºC was also performed with full, coffee-bag type cells with 4 V manganese spinel material as the cathode and lithium metal as the reference electrode. Electrochemical cycle testing at 55 ºC was performed with full, coffee-bag type cells with spinel manganese oxide cathodes and layered nickel-

manganese-cobalt oxide cathodes with lithium metal as the reference electrode at a constant current density of 100 mA/g of active material within the voltage range of 0 – 3.0 vs. Li/Li^+.

4.3 RESULTS AND DISCUSSION

4.3.1 Structural, morphological, and surface characterization

XRD patterns of the Cu_2Sb-Al_2O_3-C and Cu_2Sb-C nanocomposites that were obtained via the mechanochemical reduction are given in Figure 4.1. Both nanocomposites show broad reflections corresponding to Cu_2Sb (JCDPS Powder Diffraction File Card No. 22-601). No reflections corresponding to Al_2O_3 were observed in the case of Cu_2Sb-Al_2O_3-C, possibly due to an amorphous or poorly crystalline character of Al_2O_3. XRD data on the samples of Cu_2Sb-Al_2O_3-C with 0 wt. % and 10 wt. % carbon show a trend of increasing crystallinity as the amount of carbon in the composite is reduced. Figure 4.2 shows the XRD patterns of Cu_2Sb-Al_2O_3-C with 20, 10, and 0 wt. % carbon. Figure 4.2(a) is of the Cu_2Sb-Al_2O_3 material. No Al_2O_3 is observed, but the pattern for crystalline Cu_2Sb is present. The sharpness of the peaks decreases when 10 wt. % carbon is present (Fig 4.2(b)), and all but the main Cu_2Sb peak disappears when 20 wt. % carbon is present in the Cu_2Sb-Al_2O_3-C composite material. This difference in the XRD pattern reflects a difference in morphology, either larger particles are formed when less carbon is present, or the particles are more crystalline when less carbon is present. It is possible that the effect of the carbon during the synthesis process is one of a buffer and separator of reactants. Analogous to micelle-based synthesis methods where the size of the reactive region is constrained for creation of nanoscale particles, it is possible that the carbon keeps the Cu and Sb_2O_3 in discrete regions and therefore limits the final size of the particles. The increased amount of carbon could also

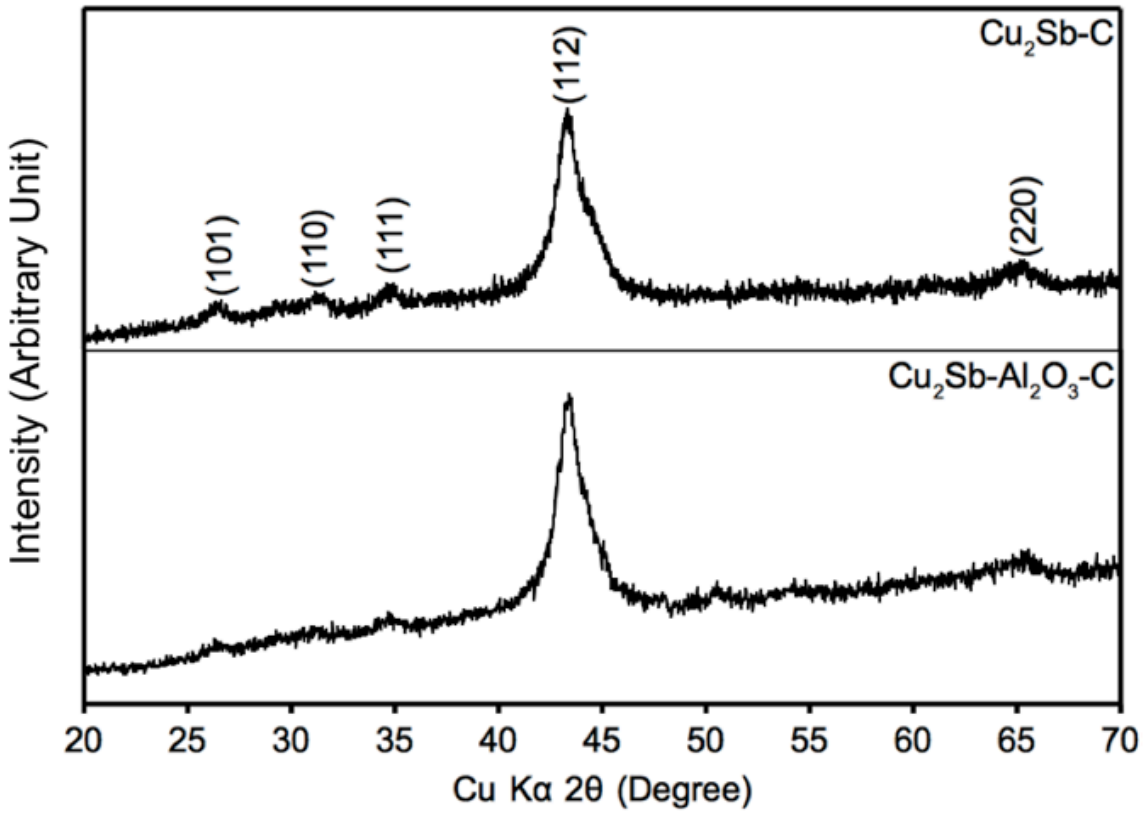

Figure 4.1. XRD patterns of Cu_2Sb-C and Cu_2Sb-Al_2O_3-C nanocomposites obtained by the mechanochemical reduction reaction.

absorb heat during the reaction, allowing the reaction between Cu and Sb to occur at a slower rate and hence, reduce the final average particle size of the Cu_2Sb crystals in the composite. The difference in morphology is reflected in the cycle performance and reaction mechanism of each of the materials as well. The electrochemical differences between the composite materials with varied carbon content are presented in detail in section 4.3.2.

Figure 4.3 shows a comparison between the XRD pattern of Cu_2Sb-Al_2O_3-C milled for 12 h and Cu_2Sb-Al_2O_3-C milled for 24 h. The Cu_2Sb-Al_2O_3-C with the 24 h milling time (Fig. 4.3(a)) shows a XRD pattern similar to Cu_2Sb-Al_2O_3-C with the 12 h

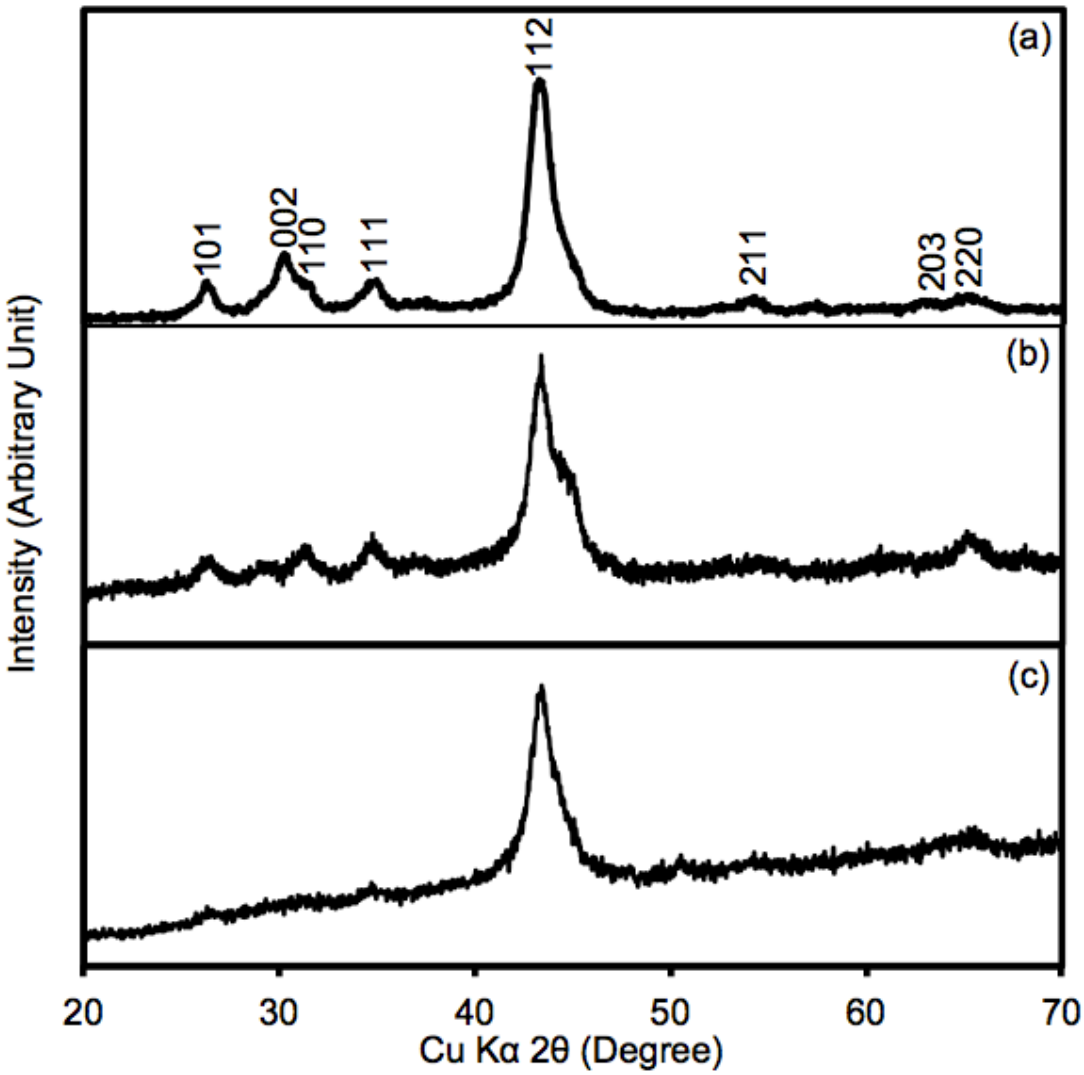

Figure 4.2. XRD patterns of (a) Cu_2Sb-Al_2O_3, (b) Cu_2Sb-Al_2O_3-C with 10 wt. % acetylene black, and (c) Cu_2Sb-Al_2O_3-C with 20 wt. % acetylene black.

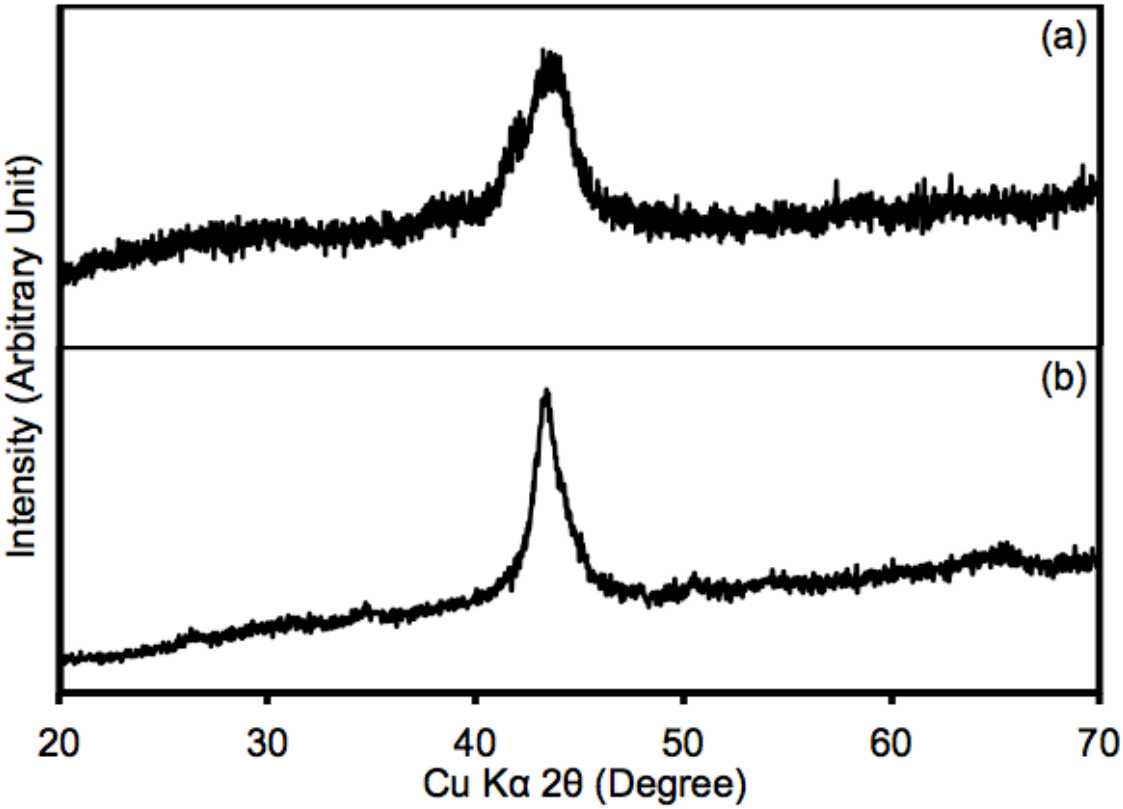

Figure 4.3. XRD patterns of (a) Cu_2Sb-Al_2O_3-C synthesized for 24 h and (b) Cu_2Sb-Al_2O_3-C synthesized for 12 h.

milling time (Fig. 4.3(b)), indicating an initial comparability in crystallinity between the two materials.

In order to better characterize the Cu_2Sb-Al_2O_3-C sample, XPS analysis was performed on an uncycled Cu_2Sb-Al_2O_3-C electrode and the results are shown in Figure 4.4. There are two peaks in the Al 2p region. The peak at 75.2 eV corresponds to Al 2p in Al_2O_3[19] while the other peak at 77 eV corresponds to Cu $3p_{1/2}$. The Cu $2p_{3/2}$ peak in the Cu_2Sb-Al_2O_3-C sample occurs at 933.5 eV compared to 932.7 eV expected for metallic copper. This shift in the Cu $2p_{3/2}$ binding energy indicates the absence of free metallic Cu and the presence of Cu to Sb bonding. The Sb 3d spectrum overlaps with the O 1s

spectrum from Al_2O_3. There are two pairs of peaks present for Sb 3d. The binding energies of the Sb(2) peaks match closely with that of metallic Sb, suggesting the presence of an amount of metallic Sb impurity although the XRD data did not indicate metallic Sb. The Sb(1) peaks are at higher binding energies than the Sb(2) peaks and are attributed to the antimony that is bound to Cu in the Cu_2Sb alloy.

XPS was also performed on the Cu_2Sb-Al_2O_3-C powders that were synthesized for 24 h and 12 h. Figure 4.5 shows the Sb spectra for Cu_2Sb-Al_2O_3-C synthesized with different milling times. The dotted vertical lines indicate the position for metallic Sb peaks. The Cu_2Sb-Al_2O_3-C with the 12 h synthesis has only one type of Sb, that of Cu_2Sb. The Cu_2Sb-Al_2O_3-C with the 24 h synthesis shows the presence of trace amounts of metallic antimony.

The morphology of Cu_2Sb-Al_2O_3-C and Cu_2Sb-C was investigated with SEM and TEM. SEM images of Cu_2Sb-Al_2O_3-C and Cu_2Sb-C in Figures 4.6(a) and 4.6(b) show the morphology of the composite material. The overall morphology of the Cu_2Sb-Al_2O_3-C and the Cu_2Sb-C materials is similar. Figure 4.7 shows a comparison between SEM images of Cu_2Sb-Al_2O_3-C with a 12 h synthesis and a 24 h synthesis. There is no observable difference between the two materials on the level that is visible through SEM. Both materials appear to have homogenous mixing of Cu_2Sb-Al_2O_3 and larger acetylene black particles. The TEM images of Cu_2Sb-Al_2O_3-C (Fig. 4.8(a)) show that the material is composed of 2 – 10 nm sized, crystalline Cu_2Sb particles mixed with carbon. The Al_2O_3 in the Cu_2Sb-Al_2O_3-C material could not be observed with TEM. When compared to the Cu_2Sb-Al_2O_3-C nanocomposite, the TEM of the Cu_2Sb-C material shows crystalline particles with boundaries that are more defined (Fig. 4.8(b)).

The tap density of Cu_2Sb-Al_2O_3-C was measured in order to get an idea of the practical volumetric capacity of this material. With a tap density of $\sim$ 1.4 g/cm^3, Cu_2Sb-

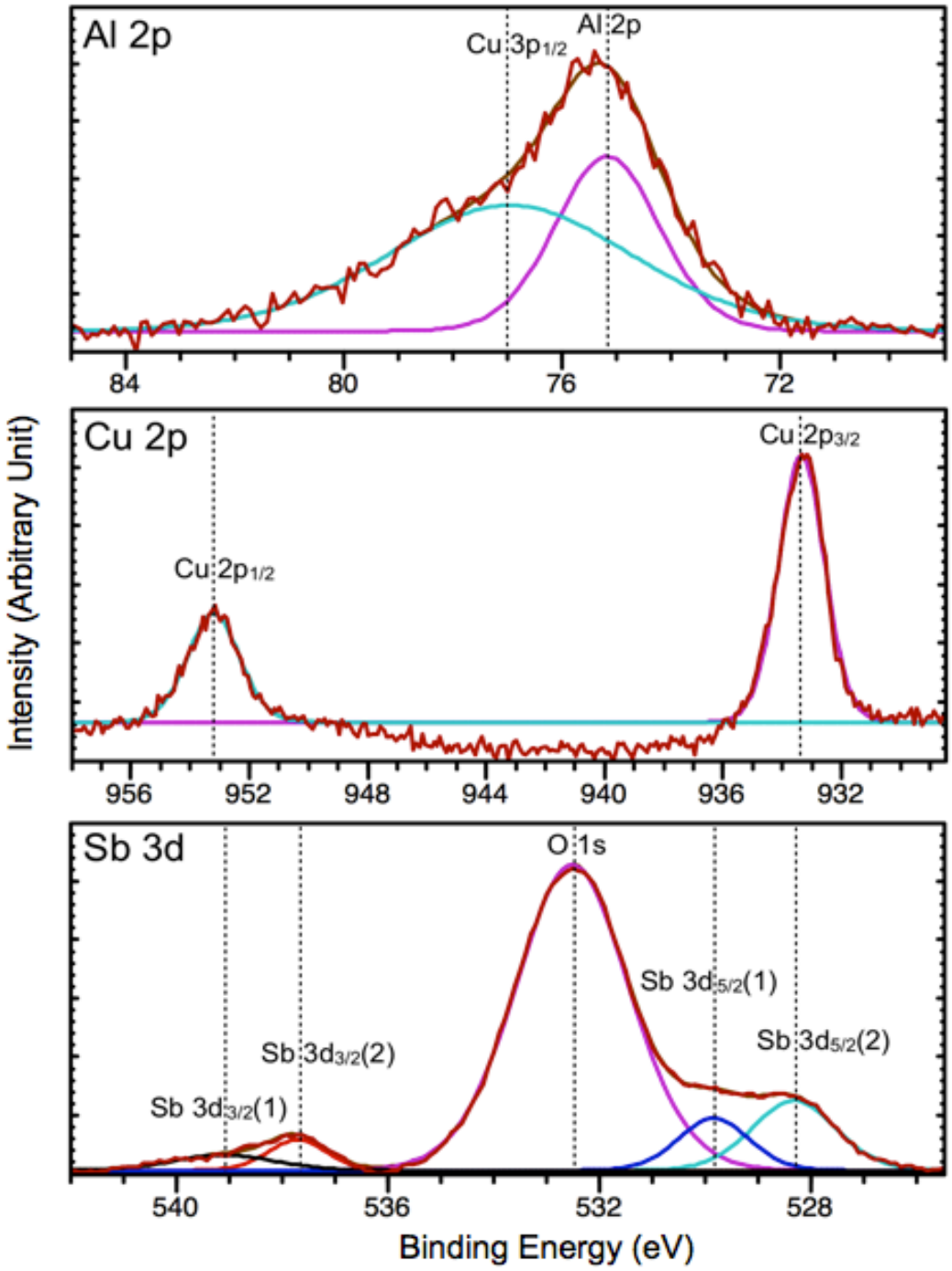

Figure 4.4. Al 2p, Cu 2p, and Sb 3d XPS spectra of an uncycled Cu_2Sb-Al_2O_3-C electrode.

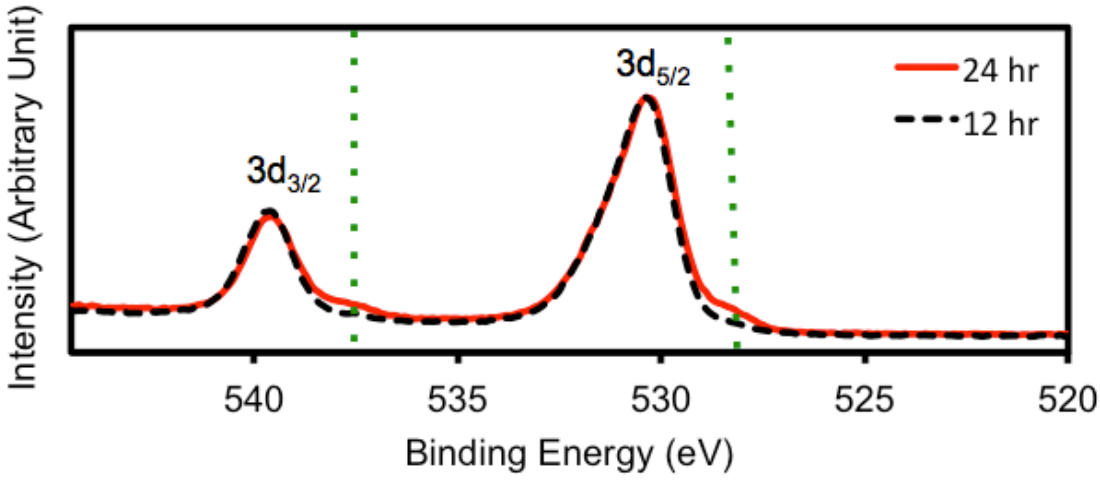

Figure 4.5. Sb 3d XPS spectra of Cu_2Sb-Al_2O_3-C powders after 24 and 12 h milling times.

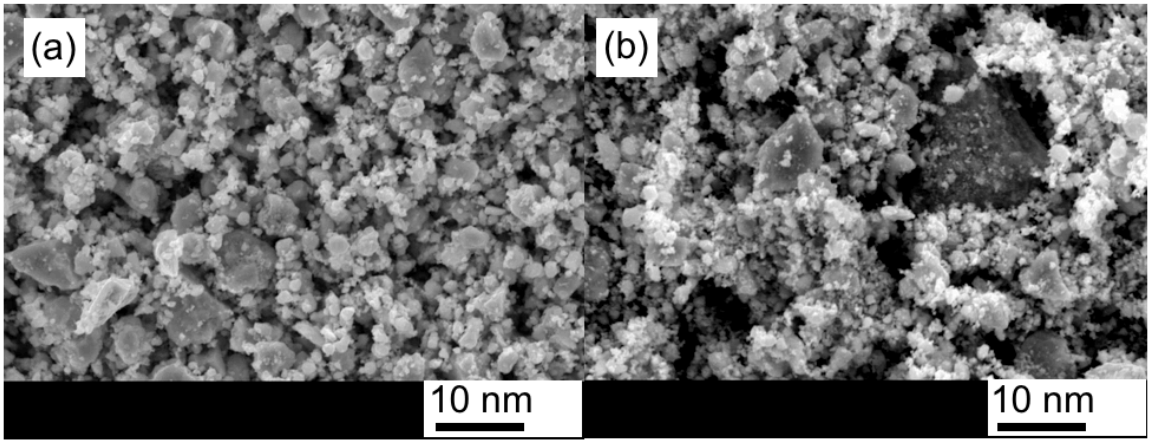

Figure 4.6. SEM images of (a) Cu_2Sb-C and (b) Cu_2Sb-Al_2O_3-C.

Al_2O_3-C offers significantly higher volumetric capacity than the commonly used graphite anode. The volume fraction of Cu_2Sb-Al_2O_3-C that is carbon has a large impact on the

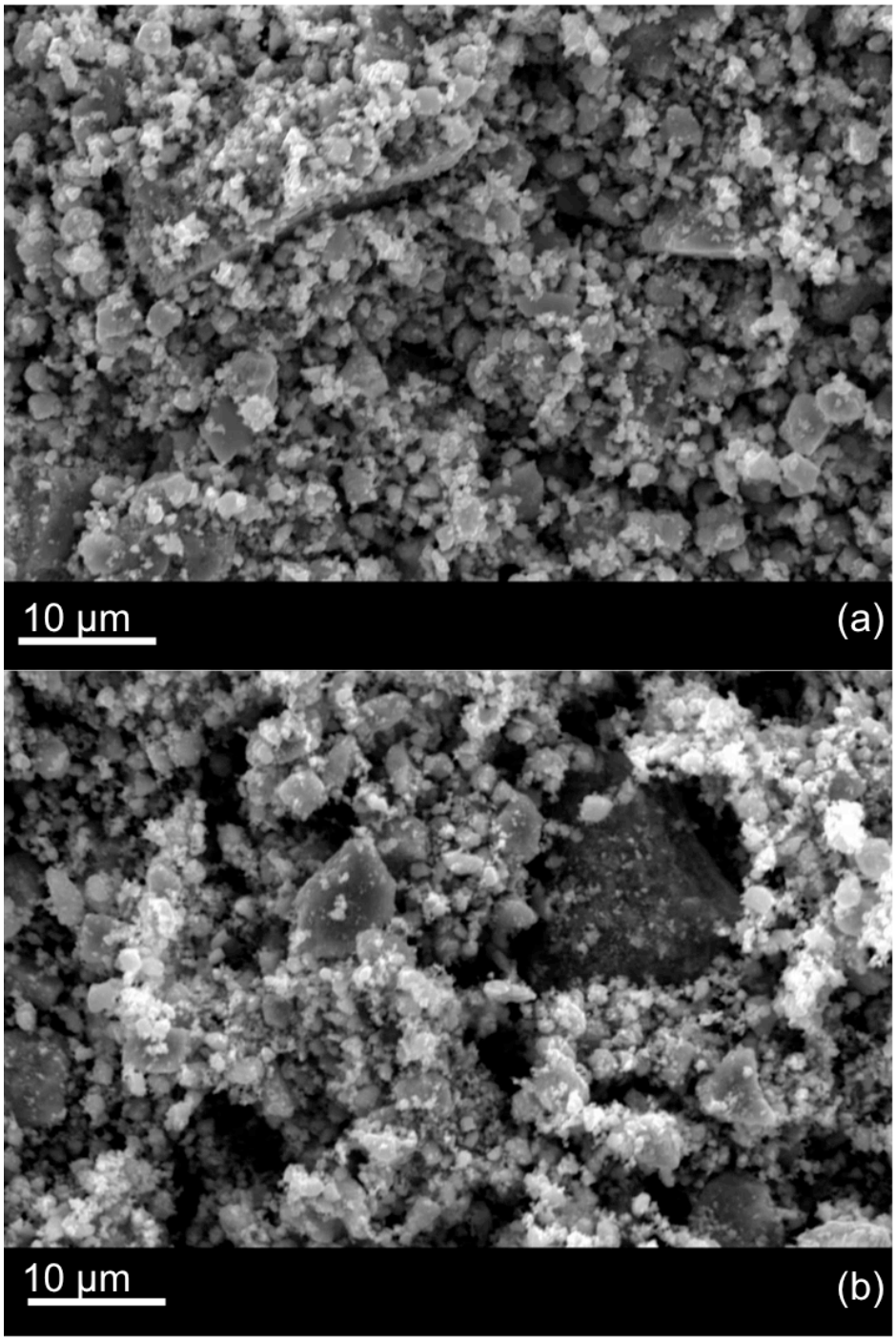

Figure 4.7. SEM images of Cu_2Sb-Al_2O_3-C (a) 24 h and (b) 12 h milling time.

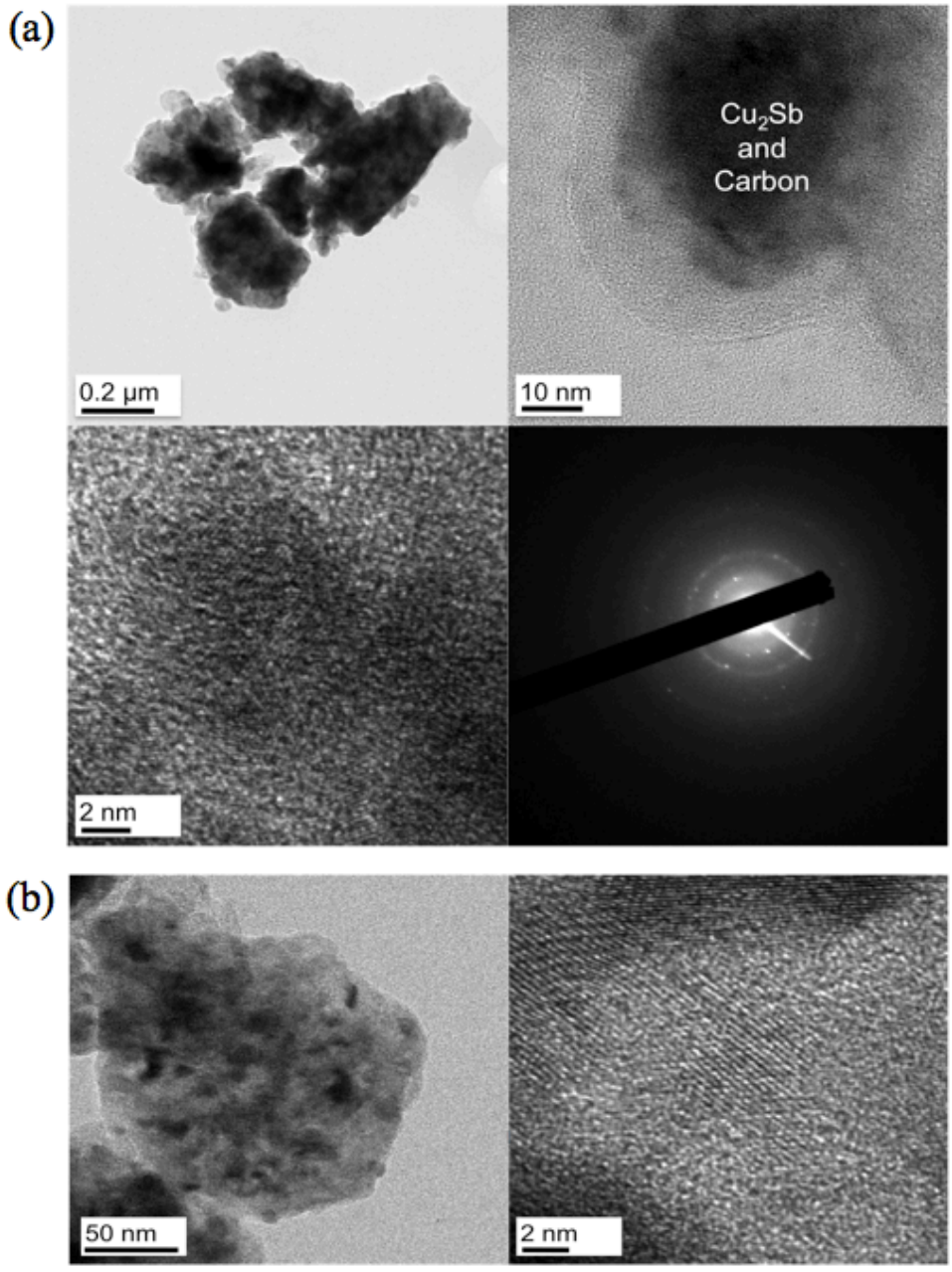

Figure 4.8. TEM images of (a) Cu_2Sb-Al_2O_3-C powder and (b) Cu_2Sb-C powder.

overall tap density of the composite. The more carbon that is present, the lower the tap density and volumetric capacity will be. Improvements were made to the tap density of Cu_2Sb-Al_2O_3-C by reducing the amount of carbon in the composite. Cu_2Sb-Al_2O_3 had a

tap density of 3.61 g/cm^3, which is over two and a half times the tap density of Cu_2Sb-Al_2O_3-C with 20 wt. % acetylene black. This increase in tap density shows the potential of Cu_2Sb-Al_2O_3-C composites to have extremely high volumetric capacities, if the negative effects of reducing the amount of carbon can be overcome.

4.3.2 Electrochemical characterization

Figure 4.9 shows the voltage profile and differential capacity plot (DCP) for the Cu_2Sb-Al_2O_3-C nanocomposite. The Cu_2Sb-Al_2O_3-C nanocomposite exhibits first cycle discharge and charge capacities of 633 and 434 mAh/g, respectively, implying an irreversible capacity loss of 199 mAh/g and a coulombic efficiency of 68 % in the first cycle. A feature of the DCP, shown in Figure 4.9(b), is that there are three peaks on the discharge portion of the plot and four peaks in the charge portion of the plot. This suggests that either there may be an irreversible reaction that takes place during the charging of the Cu_2Sb-Al_2O_3-C electrode or the reaction mechanism that takes place during lithiation of Cu_2Sb-Al_2O_3-C is different from the reaction mechanism that takes place during delithiation of Cu_2Sb-Al_2O_3-C. If there was an irreversible reaction taking place during cycling of Cu_2Sb-Al_2O_3-C, the stable cycle performance that is observed with this material would not be present. Because stable cycle performance is observed, it is more likely that the DCP is indicating an asymmetric reaction mechanism between lithium and Cu_2Sb-Al_2O_3-C. In order to better understand the reactions that take place during cycling, XRD was performed on electrodes that had been cycled to different points in the charge/discharge cycle. However, because the Cu_2Sb-Al_2O_3-C material is weakly crystalline, distinct phases could not be observed in the cycled electrodes (Fig. 4.10).

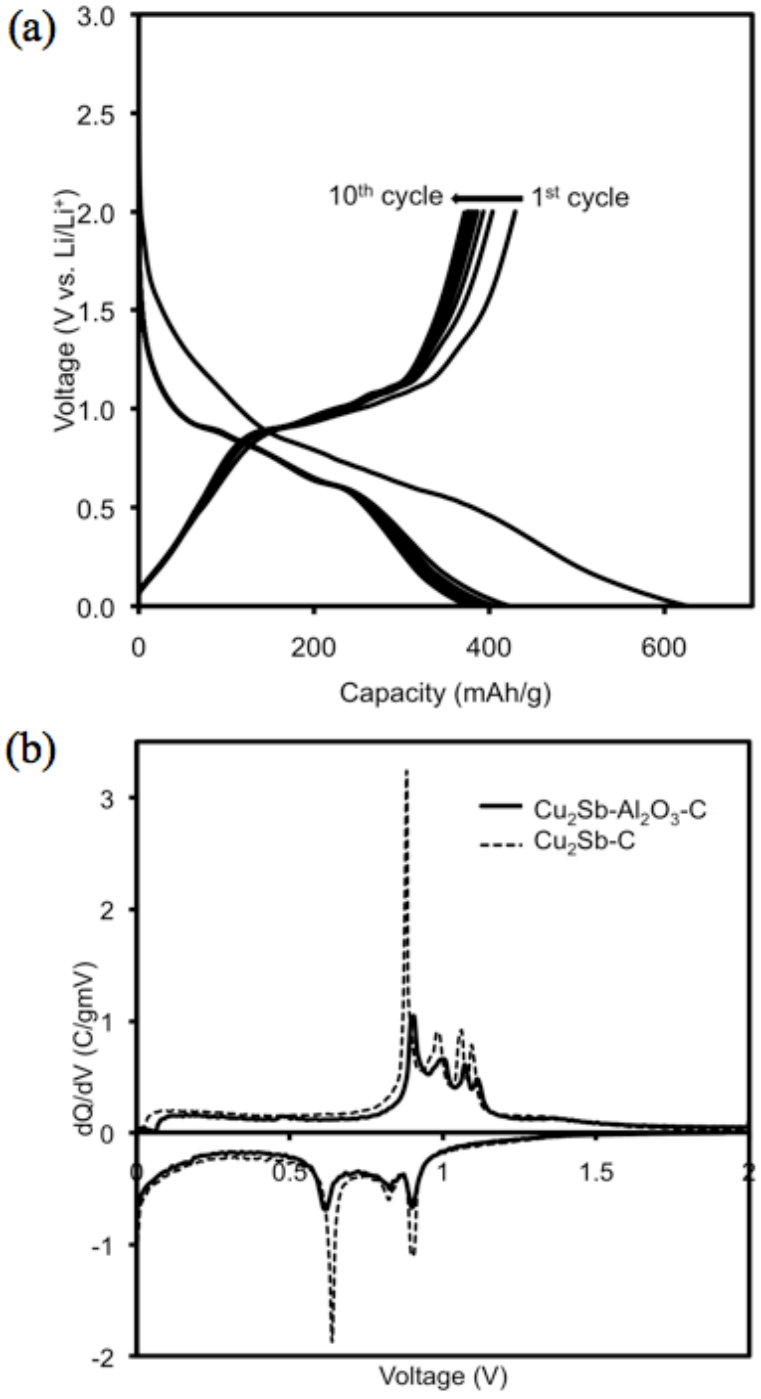

Figure 4.9. (a) Voltage profile of Cu_2Sb-Al_2O_3-C and (b) differential capacity plot comparison of Cu_2Sb-Al_2O_3-C and Cu_2Sb-C at a current rate of 100 mA/g of active electrode material.

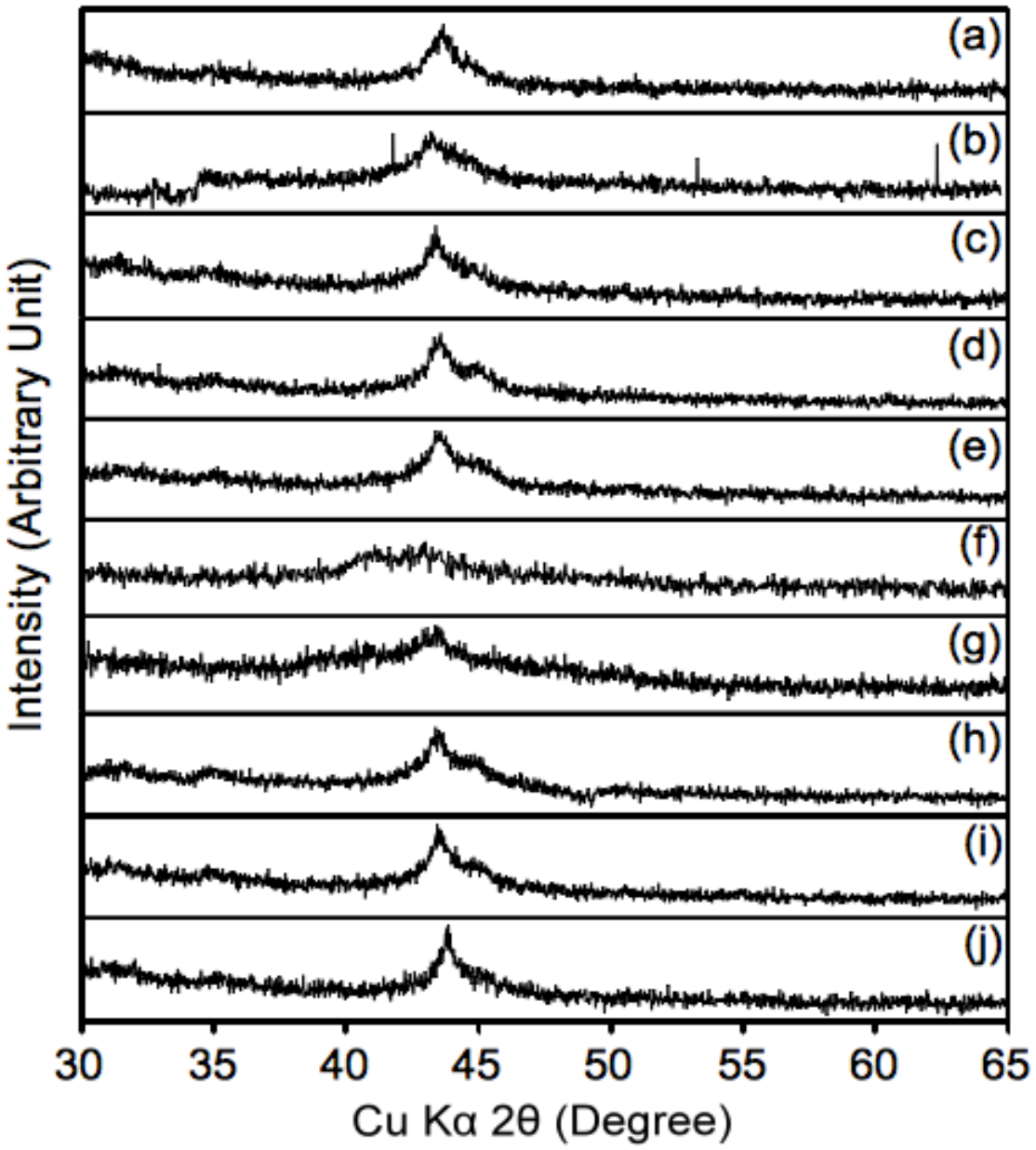

Figure 4.10. *Ex-situ* XRD patterns for Cu_2Sb-Al_2O_3-C electrodes (a) uncycled, discharged to (b) 0.76 V, (c) 0.65 V, (d) 0.33 V, and (e) 0.0 V, and charged to (f) 0.93 V (g) 1.03 V, (h) 1.1 V, (i) 1.29 V, and (j) 2.0 V. All voltages are vs. Li/Li^+.

Because the rate of charge can affect the reaction mechanism for an electrode, cells were made with Cu_2Sb-Al_2O_3-C and cycled at 5 mA/g of active electrode material. 5 mA/g is 20 times slower than the other cycling performed in this research. At such a low rate, it was thought that any irreversible or diffusion limited steps in the reaction would be allowed to go to completion. The result of the 5 mA/g cycling is shown in Figure 4.11. Figure 4.X(a) is Cu_2Sb-Al_2O_3-C at a current rate of 5 mA/g, during the second cycle. Figure 4.X(b) is Cu_2Sb-Al_2O_3-C at a current rate of 5 mA/g, during the fourth cycle. The DCP for both the second and the fourth cycles is significantly noisy, but just as was observed in the DCP for Cu_2Sb-Al_2O_3-C at a current rate of 100 mA/g (Fig. 4.9(b)), three peaks are present in the discharge cycle and four peaks are present in the charge cycle. The low-rate cycling has given further evidence of the reversibility and asymmetry of the reaction between Cu_2Sb-Al_2O_3-C and lithium.

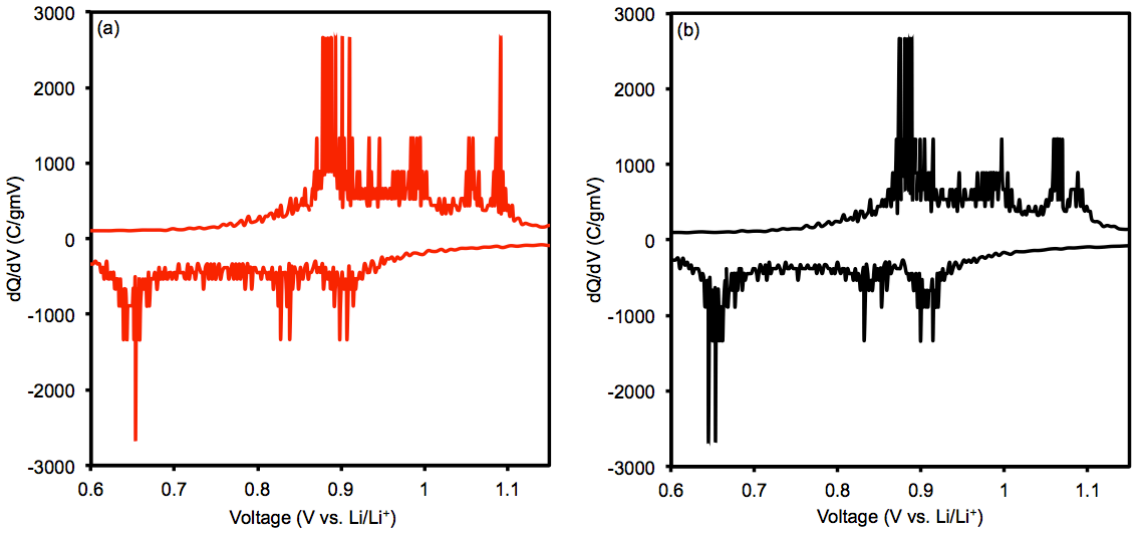

Figure 4.11. Differential capacity plots of Cu_2Sb-Al_2O_3-C cycled at a current rate of 5 mA/g of active electrode material in the (a) 2nd and (b) 4th cycle.

The main significance of Cu_2Sb-Al_2O_3-C as an anode material lies in the cycle life. Figure 4.12(a) shows the cyclability of Cu_2Sb-Al_2O_3-C over 500 cycles.

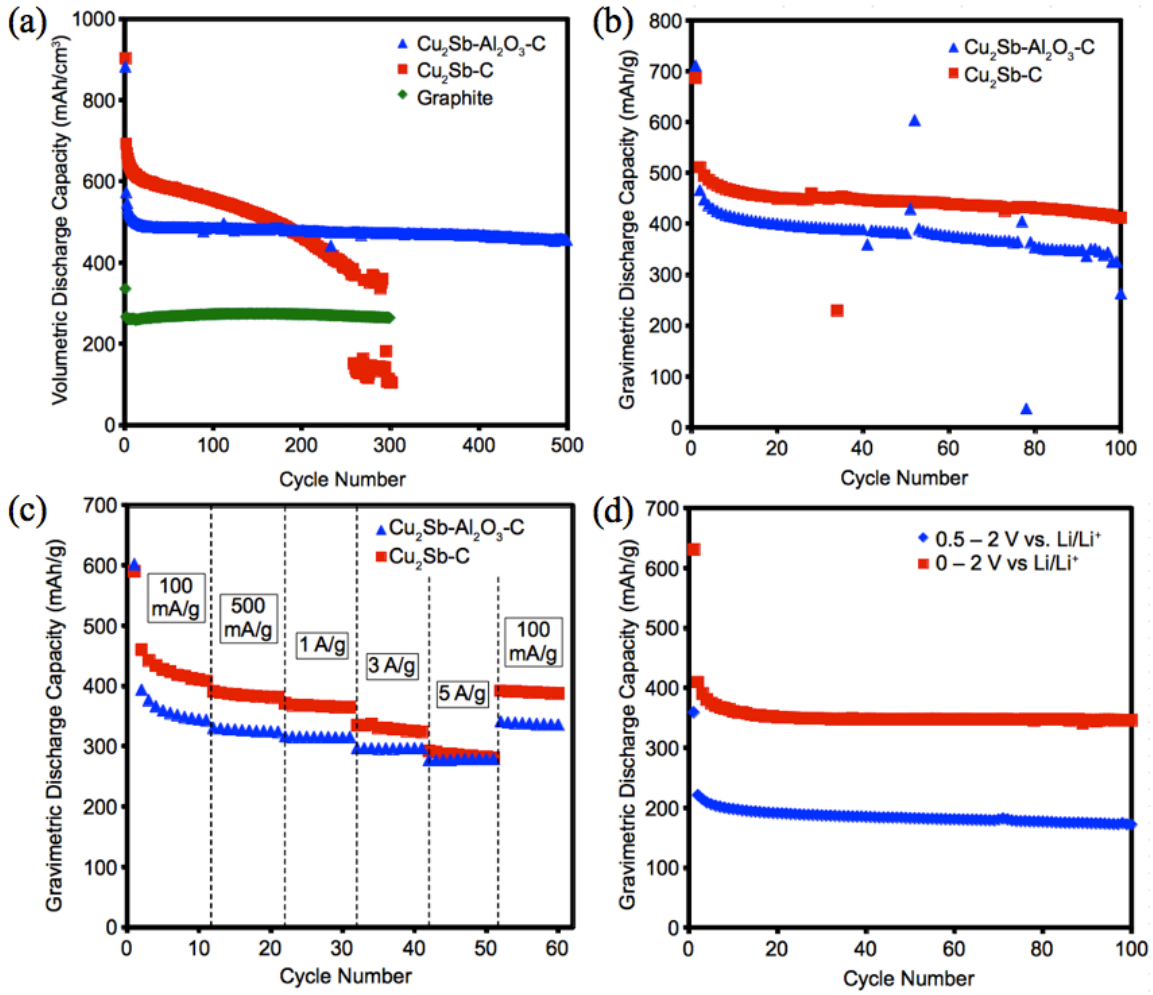

Figure 4.12. Cycle performance of (a) Cu_2Sb-Al_2O_3-C from 0 – 2.0 V vs. Li/Li^+ at 25 °C, (b) Cu_2Sb-Al_2O_3-C and Cu_2Sb-C at 55 °C and a current of 100 mA/g of active electrode material between 0 – 2 V vs. Li/Li^+, (c) rate capability comparison of Cu_2Sb-Al_2O_3-C and Cu_2Sb-C at 25 °C between 0 – 2 V vs. Li/ Li^+, and (d) Cu_2Sb-Al_2O_3-C discharged to 0 V and 0.5 V vs. Li/Li^+ at 25 °C. All current rates were at a current rate of 100 mA/g of active electrode material unless otherwise stated.

Cu_2Sb-Al_2O_3-C cycles well for 500 cycles and retains 80 % of its capacity after the first cycle. The presence of Al_2O_3 in the nanocomposite has a significant impact on the cycle performance of Cu_2Sb-Al_2O_3-C as compared with that of Cu_2Sb-C. As seen in Figure 4.12(a), Cu_2Sb-C alloy anodes are only stable for approximately 100 cycles. The dramatic improvement in volumetric capacity of Cu_2Sb-Al_2O_3-C over graphite is shown in Figure 4.12(a). The high-temperature performance of Cu_2Sb-C was slightly better than that of Cu_2Sb-Al_2O_3-C. Both Cu_2Sb-based materials were stable for 100 cycles at high temperature (Fig. 4.12(b)). When cycled at different charge rates, Cu_2Sb-C performs comparably to Cu_2Sb-Al_2O_3-C, but yields a higher discharge capacity. A higher initial discharge capacity was observed for Cu_2Sb-C cells during all other cycle tests as well. Both Cu_2Sb-C and Cu_2Sb-Al_2O_3-C materials showed excellent rate capability. The cycle performance of Cu_2Sb-Al_2O_3-C and Cu_2Sb-C at different charge rates is shown in Figure 4.12(c). One of the advantages of Cu_2Sb-Al_2O_3-C over graphite is that it reacts with lithium well above 0 V vs. Li/Li^+. The cycle performance of Cu_2Sb-Al_2O_3-C between 0.5 – 2.0 V vs. Li/Li^+ is not as stable as the cycle performance of Cu_2Sb-Al_2O_3-C between 0.0 – 2.0 V vs. Li/Li^+ (Fig. 4.12(d)), yet the performance of Cu_2Sb-Al_2O_3-C between 0.5 – 2.0 V vs. Li/Li^+ decays slowly over many cycles rather than failing catastrophically. When Cu_2Sb-Al_2O_3-C is cycled between 0.5 – 3.0 V vs. Li/Li^+ on an aluminum substrate, the first cycle irreversible capacity loss is reduced to 95 mAh/g. The cycle performance between 0.5 – 3.0 V vs. Li/Li^+ demonstrates that first cycle irreversible capacity loss that is observed with Cu_2Sb-Al_2O_3-C is largely dependent upon the voltage window that is chosen for operation.

Figure 4.13 shows the room temperature cycle performance of Cu_2Sb-Al_2O_3-C made with 0, 10, 15, and 20 w. % acetylene black. Two things happen when the amount of carbon in the composite is reduced: the first-cycle irreversible capacity loss decreases,

and the cycle performance becomes poor. When the amount of carbon is increased from 15 to 20 w. % acetylene black, the number of stable cycles is doubled. It is possible that between 15 and 20 wt. % acetylene black, there is an optimal amount of carbon, and further testing is needed to determine that percentage.

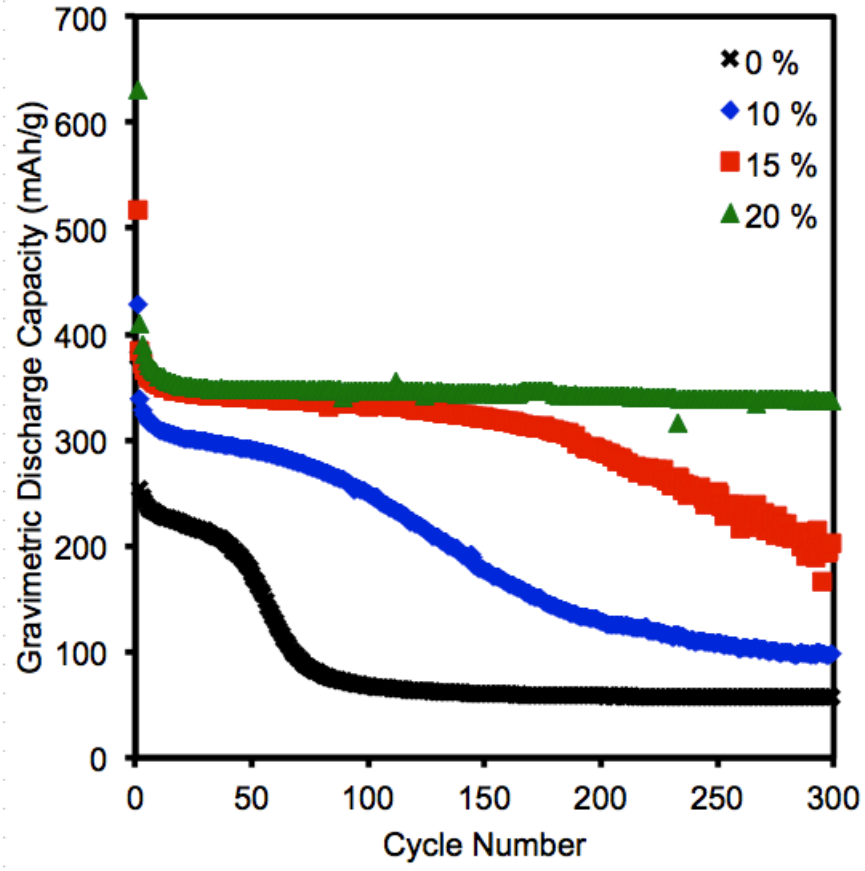

Figure 4.13. Cycle performance of Cu_2Sb-Al_2O_3-C with different carbon contents from 0 – 2.0 V vs. Li/Li^+ at 25 °C at a current rate of 100 mA/g of active electrode material.

In order to shed light on the differences in performance for composites with decreased amounts of carbon, comparisons between the DCP's were made. The DCP comparisons give further information about the significance of particle size and

crystallinity on the reversibility of the reactions between Cu_2Sb-Al_2O_3-C and lithium. Figure 4.14 shows the DCP of Cu_2Sb-Al_2O_3-C made with 10 wt. % acetylene black. The

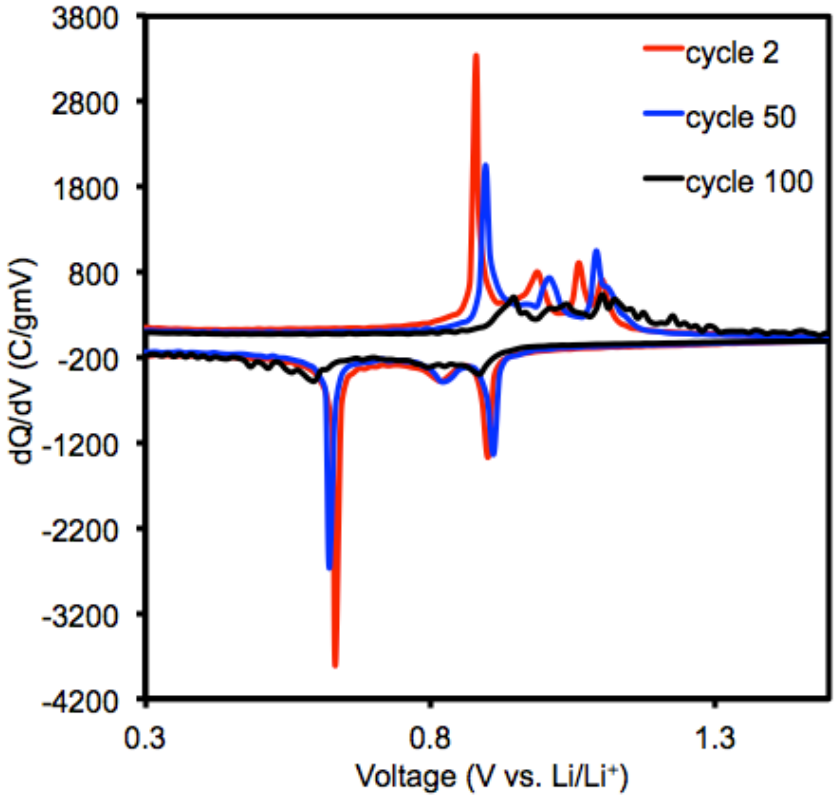

Figure 4.14. Differential capacity plot of Cu_2Sb-Al_2O_3-C with 10 wt. % acetylene black cycled 0 – 2.0 V vs. Li/Li^+ at 25 °C at a current rate of 100 mA/g of active electrode material.

DCP of Cu_2Sb-Al_2O_3-C made with 10 wt. % acetylene black shows the disappearance of the fourth charge peak when the material is cycled from cycle 2 to cycle 50. By cycle 100, the cycle performance has degraded completely and the peaks of the DCP are no longer prominent. The disappearance of the fourth charge peak, along with the failure of the material hints at the importance of the four distinct steps in the reaction mechanism between Cu_2Sb-Al_2O_3-C and lithium. Figure 4.15 is the DCP of Cu_2Sb-Al_2O_3; this

material showed the least stable performance of any of the Cu_2Sb-Al_2O_3-based materials. The DCP of Cu_2Sb-Al_2O_3 shows three discharge peaks and two charge peaks during the second cycle. By the 50th cycle, Cu_2Sb-Al_2O_3 only has one discharge peak and one charge peak. Clearly, the distinct separation of steps in reaction mechanism plays a significant role in the cycle life of Cu_2Sb-Al_2O_3-based composites.

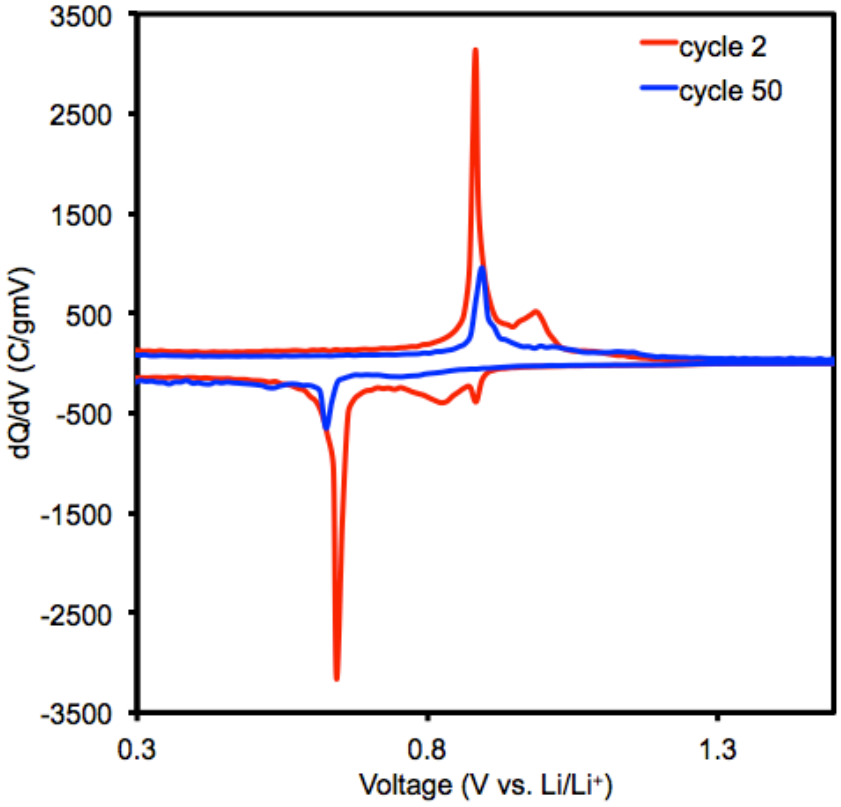

Figure 4.15. Differential capacity plots of Cu_2Sb-Al_2O_3 cycled at 0 – 2.0 V vs. Li/Li^+ at 25 °C at a current rate of 100 mA/g of active electrode material.

A comparison between the cycle performance of Cu_2Sb-Al_2O_3-C milled for 12 and 24 h is shown in Figure 4.16. The discharge capacity was virtually the same for both samples, with the 24 hr milled Cu_2Sb-Al_2O_3-C having a slightly lower capacity. The 24 h

milled Cu_2Sb-Al_2O_3-C showed less first-cycle irreversible capacity loss than the 12 h milled Cu_2Sb-Al_2O_3-C, which corresponded to a first-cycle coulombic efficiency of 75 % vs. 67 % for the 12 h milled Cu_2Sb-Al_2O_3-C sample. Any reduction in the first-cycle irreversible capacity loss is viewed as a significant improvement in the viability of these alloy anodes as commercial alternatives to graphite.

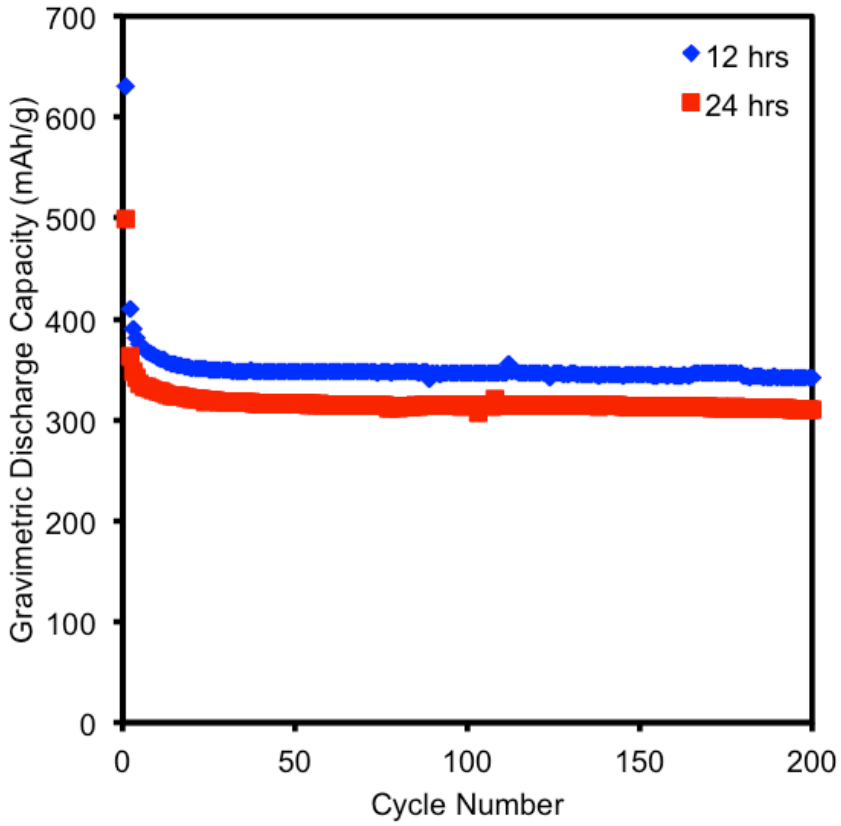

Figure 4.16. Cycle performance of Cu_2Sb-Al_2O_3-C with 24 and 12 h milling times from 0 – 2.0 V vs. Li/Li^+ at 25 °C at a current rate of 100 mA/g of active electrode material.

The differential capacity plot comparison between Cu_2Sb-Al_2O_3-C milled for 12 and 24 h shows evidence of greater reversibility in the cycle performance of Cu_2Sb-Al_2O_3-C milled for 24h (Fig. 4.16). Figure 4.17(a) shows that even over 200 cycles, the

DCP peaks for the discharging and charging of Cu_2Sb-Al_2O_3-C milled for 24 h have not changed significantly in area or location. Figure 4.17(b) is the DCP for 12 h milled Cu_2Sb-Al_2O_3-C, and in particular, it is data from a cell that showed 500 cycles of stable capacity. Significant changes in the shape and location of the peaks are observed in the

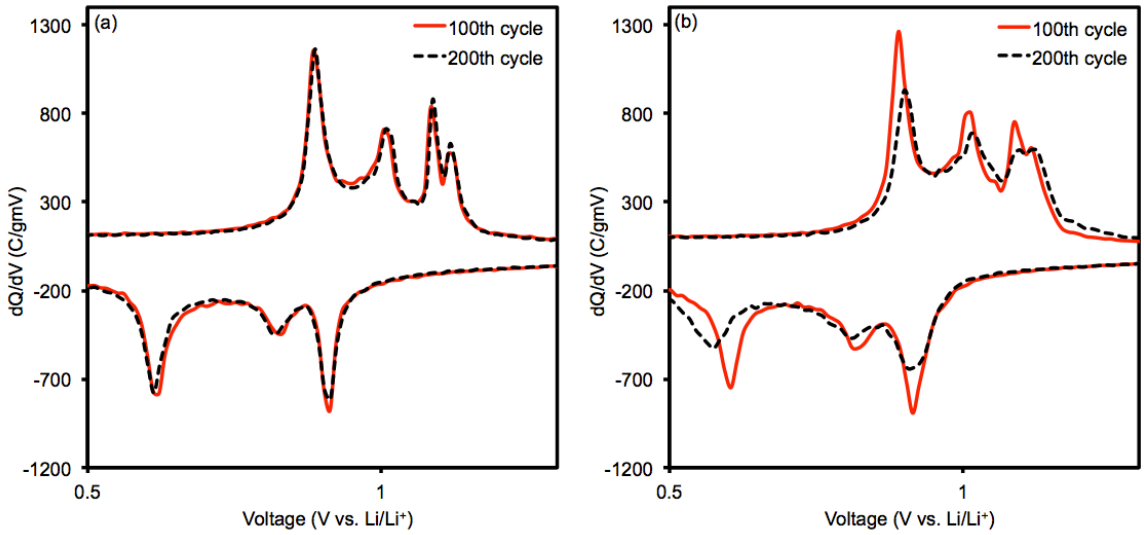

Figure 4.17. Differential capacity plots of Cu_2Sb-Al_2O_3-C with (a) 24 h and (b) 12 h milling times cycled at 0 – 2.0 V vs. Li/Li^+ at 25 °C at a current rate of 100 mA/g of active electrode material.

DCP for 12 h milled Cu_2Sb-Al_2O_3-C. The discharge peaks shift to lower potentials and the charge peaks drift toward higher potentials on the DCP for 12 h milled Cu_2Sb-Al_2O_3-C when cycled from 100 to 200 cycles. Additionally, the third and fourth charge peaks have essentially combined into one peak during the 200^{th} cycle for the 12 h milled Cu_2Sb-Al_2O_3-C material. This combination of charge peaks is similar to what was observed for Cu_2Sb-Al_2O_3-C when the amount of carbon in the composite was reduced. The reason for the improvement in the reversibility of the reaction between Cu_2Sb-Al_2O_3-C and lithium when the composite is milled for 24 h could be a further reduction in particle size.

Further investigation into the character of Cu_2Sb-Al_2O_3-C milled for 24 h is necessary to determine the cause. Because of the reduction in first-cycle irreversible capacity loss and the improved reversibility of the reaction mechanism of Cu_2Sb-Al_2O_3-C milled for 24 h, it is concluded that increasing the milling time of Cu_2Sb-Al_2O_3-C is an important step in optimization towards commercial viability.

In order to determine the irreversibility of any steps in the reaction mechanism, cells were cycled in various ranges of voltage, with and without conditioning cycles. Because cycling over full depth of discharge can also affect the cell performance, tests were also performed to compare delithiation up to the open circuit voltage (2.6 – 3.0 V vs. Li/Li^+) with delithiation to the standard 2.0 V vs. Li/Li^+. The standard peaks for lithium insertion into Cu_2Sb-Al_2O_3-C occur at 0.90, 0.84, and 0.62 V vs. Li/Li^+. The standard peaks for lithium extraction from Cu_2Sb-Al_2O_3-C occur at 0.90, 1.00, 1.07, and 1.10 V vs. Li/Li^+. If cells are cycled to the minima in between these peaks, then each of the steps in the reaction sequence can be isolated. The first peak to be isolated was the 0.90 V vs. Li/Li^+ peak in the discharge cycle.

Speculation was made as to the reaction mechanism for lithiation/delithiation of Cu_2Sb-Al_2O_3-C, based upon other reaction mechanisms in the literature for Cu_2Sb [8,27,39,41]. The proposed asymmetric reaction mechanism for Cu_2Sb-Al_2O_3-C is as follows:

Insertion:	$Cu_2Sb + Li^+ \rightarrow LiCu_2Sb$	(4.2)
	$LiCu_2Sb + Li^+ \rightarrow Li_2CuSb + Cu$	(4.3)
	$Li_2CuSb + Li^+ \rightarrow Li_3Sb + Cu$	(4.4)
Extraction:	$Li_3Sb + Cu \rightarrow Li_2CuSb + Li^+$	(4.5)
	$Li_2CuSb \rightarrow LiCuSb + Li^+$	(4.6)
	$LiCuSb + Cu \rightarrow LiCu_2Sb$	(4.7)

$$LiCu_2Sb \rightarrow Cu_2Sb + Li^+ \quad (4.8)$$

The dQ/dV minimum following the lithium insertion peak at 0.90 V vs. Li/Li^+ occurs at 0.869 V vs. Li/Li^+. The four cycling tests performed on the 0.90 V vs. Li/Li^+ lithium insertion peak were: cycling between the OCV and 0.869 V vs. Li/Li^+ (Fig. 4.18), cycling between the 2 V vs. Li/Li^+ and 0.869 V vs. Li/Li^+ (Fig. 4.19), cycling between OCV vs. Li/Li^+ and 0.869 V vs. Li/Li^+ following a full conditioning cycle (Fig. 4.20), and cycling between the 2 V vs. Li/Li^+ and 0.869 V vs. Li/Li^+ with a conditioning cycle (Fig. 4.21). When Cu_2Sb-Al_2O_3-C does not undergo a conditioning cycle, and is cycled

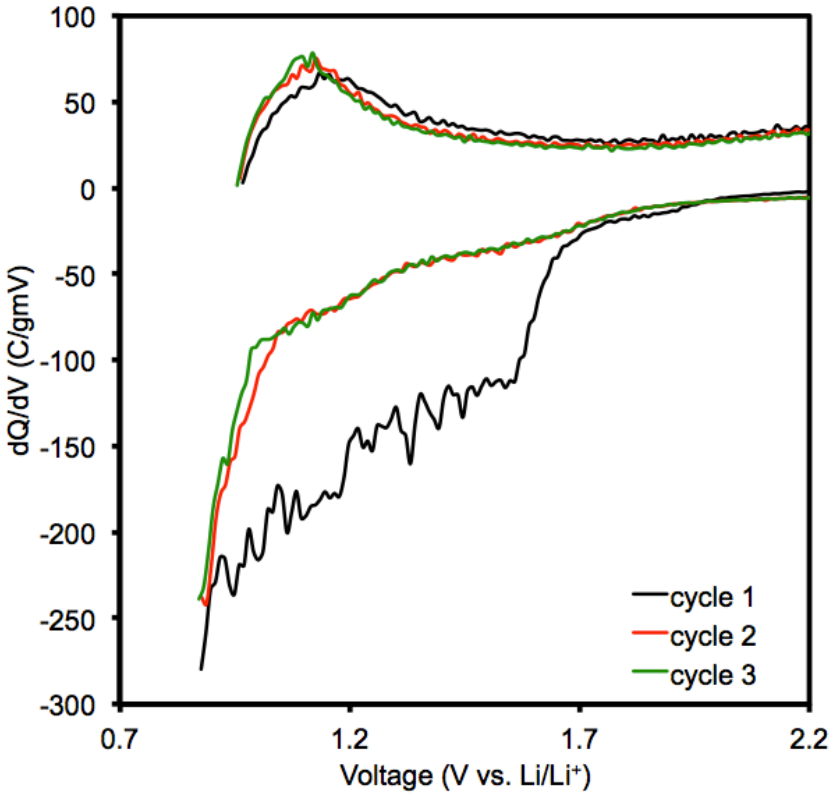

Figure 4.18. Differential capacity plot of Cu_2Sb-Al_2O_3-C cycled between OCV and 0.869 V vs. Li/Li^+ at 25 °C at a current rate of 100 mA/g of active electrode material.

between the OCV and 0.869 V vs. Li/Li^+ (Fig. 4.18), there does not appear to be any peak in the lithium insertion portion of the curve. In the first cycle, there is an onset of a reduction peak around 1.56 V vs. Li/Li^+, but that reaction does not go to completion. This onset could be the beginning stages of reduction of the electrolyte to form the SEI layer. The first step of lithium insertion into Cu_2Sb-Al_2O_3-C would be the formation of $LiCu_2Sb$, but this does not occur. In the first cycle lithium extraction curve, there is one rounded peak that occurs at ~ 1.14 V vs. Li/Li^+, which is at a potential close to the standard charge peak for Cu_2Sb-Al_2O_3-C that normally occurs at 1.10 V vs. Li/Li^+. The peak in the charge curve also shifts towards lower voltages, ending up at 1.10 V vs.

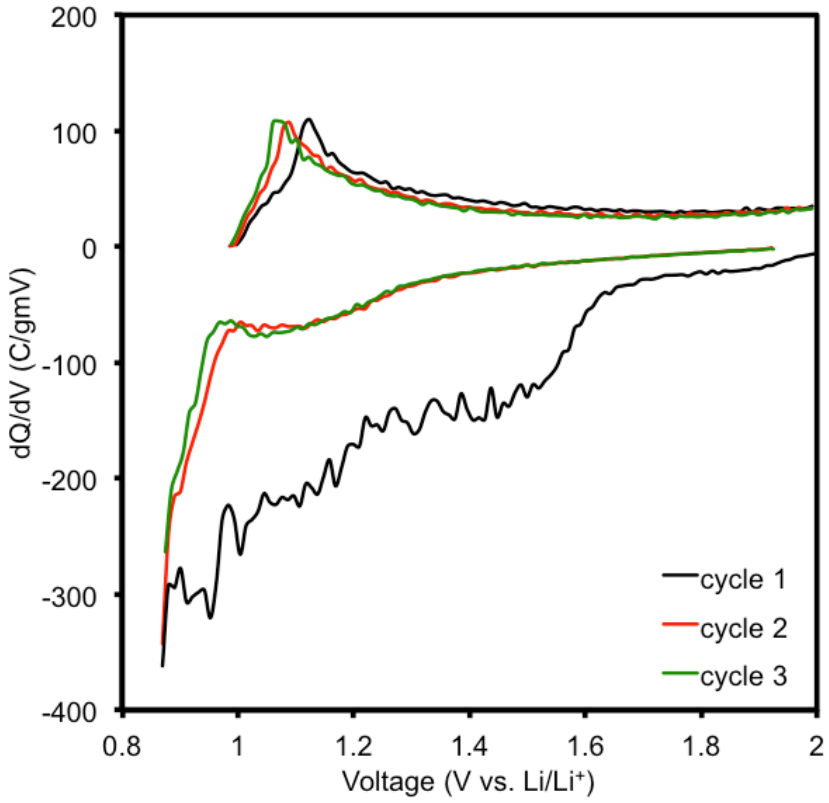

Figure 4.19. Differential capacity plot of Cu_2Sb-Al_2O_3-C cycled between 2.0 and 0.869 V vs. Li/Li^+ at 25 °C at a current rate of 100 mA/g of active electrode material.

Li/Li$^+$ by the third cycle. However, because there was no observable peak in the discharge portion of the curve, the peak in the charge portion is likely not due to lithium extraction from $LiCu_2Sb$.

When Cu_2Sb-Al_2O_3-C is cycled between 2 V and 0.869 V vs. Li/Li$^+$ (Fig. 4.19), rather than the OCV and 0.869 V vs. Li/Li$^+$, two main differences are observed. First, a small hump appears in the second cycle discharge curve around 1.05 V vs. Li/Li$^+$. Second, the peak in the charge portion of the curve is more sharp, has more area under it, and occurs at 1.10 V vs. Li/Li$^+$ in the first cycle and 1.06 V vs. Li/Li$^+$ in the third cycle.

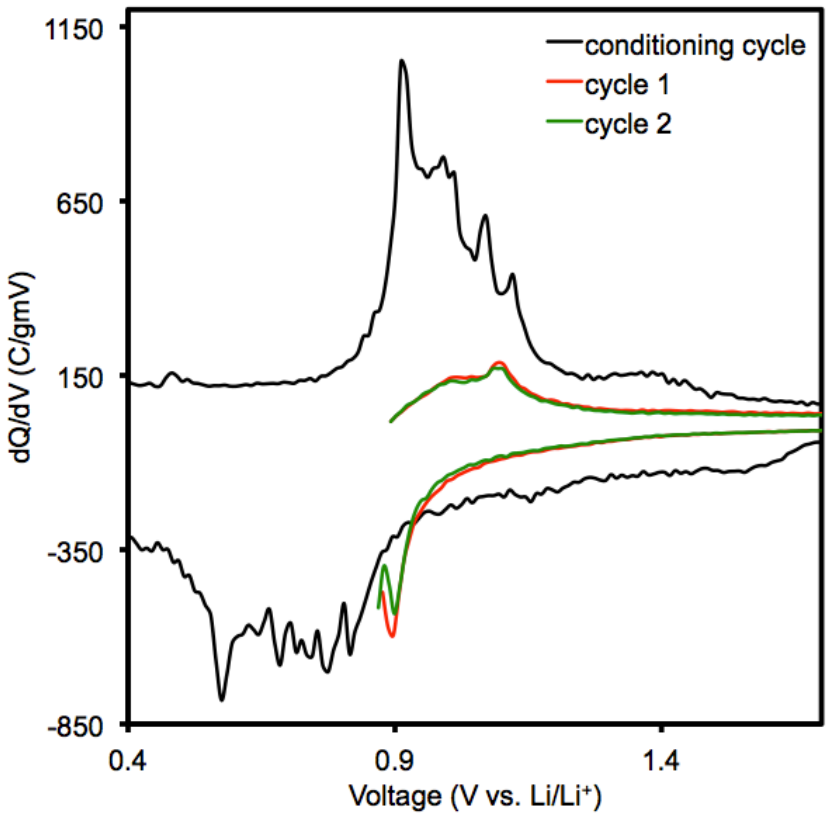

Figure 4.20. Differential capacity plot of Cu_2Sb-Al_2O_3-C cycled between OCV vs. Li/Li$^+$ and 0.869 V vs. Li/Li$^+$ following a full conditioning cycle at 25 °C at a current rate of 100 mA/g of active electrode material.

These differences indicate that cycling Cu_2Sb-Al_2O_3-C up to the OCV vs. Li/Li^+ may have a different effect on the lithium insertion/extraction reaction than cycling up to 2.0 V vs. Li/Li^+.

The effect of a conditioning cycle on the reaction mechanism was significant. When Cu_2Sb-Al_2O_3-C was cycled between OCV vs. Li/Li^+ and 0.869 V vs. Li/Li^+ following a full conditioning cycle (Fig. 4.20), a distinct peak was observed in the discharge portion of the curve at 0.9 V vs. Li/Li^+. This discharge peak is thought to

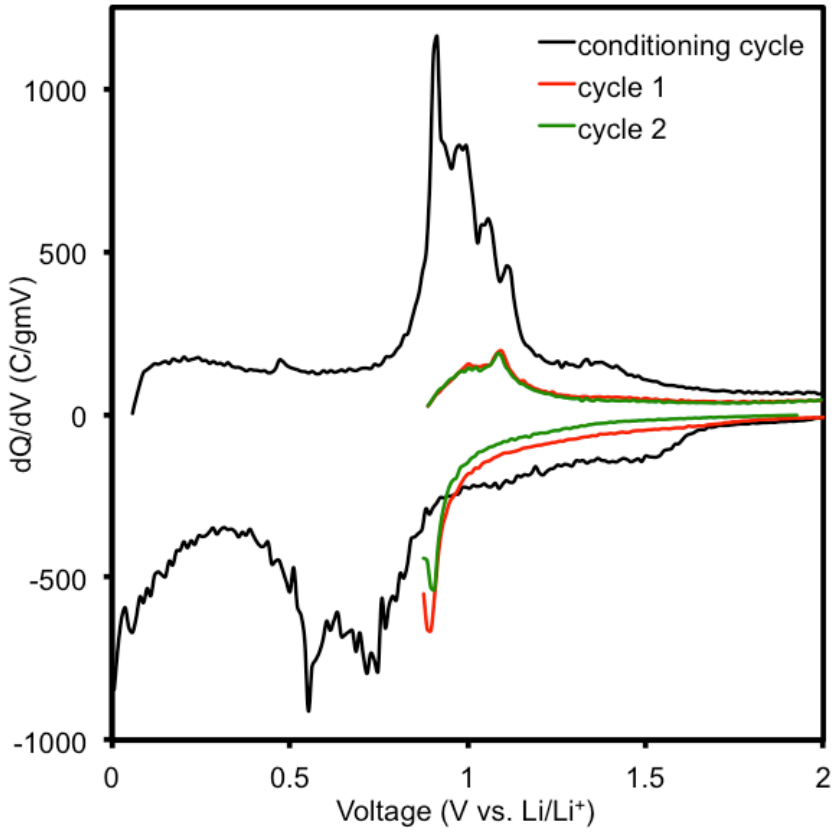

Figure 4.21. Differential capacity plot of Cu_2Sb-Al_2O_3-C cycled between 2 V vs. Li/Li^+ and 0.869 V vs. Li/Li^+ with a conditioning cycle at 25 °C at a current rate of 100 mA/g of active electrode material.

correspond to the first step of the reaction mechanism: $Cu_2Sb + Li^+ \rightarrow LiCu_2Sb$. In the first charge cycle following the conditioning cycle, one peak is also observed at 1.08 V vs. Li/Li^+. This charge peak is thought to be the last step of the reaction mechanism: $LiCu_2Sb \rightarrow Cu_2Sb + Li^+$. When Cu_2Sb-Al_2O_3-C was cycled between the 2 V vs. Li/Li^+ and 0.869 V vs. Li/Li^+ with a conditioning cycle (Fig. 4.21), the same discharge and charge peaks are observed as when Cu_2Sb-Al_2O_3-C was cycled between OCV vs. Li/Li^+ and 0.869 V vs. Li/Li^+ following a full conditioning cycle. The conditioning cycle causes changes in the material that allow the first step in the reaction mechanism to occur reversibly during subsequent cycles. These morphological and structural changes that occur during cycling are investigated further in section 4.3.3 through TEM performed on cycled Cu_2Sb-Al_2O_3-C electrodes.

The second discharge peak in the standard Cu_2Sb-Al_2O_3-C DCP occurs at 0.84 V vs. Li/Li^+. In order to determine the reversibility of the second peak, cells were cycled in the following manner: between the 2.0 and 0.77 V vs. Li/Li^+ without a conditioning cycle (Fig. 4.22), between the OCV and 0.77 V vs. Li/Li^+ without a conditioning cycle (Fig. 4.23), and between the 2.0 and 0.77 V vs. Li/Li^+ with a conditioning cycle (Fig. 4.24).

When Cu_2Sb-Al_2O_3-C is cycled between 2 V and 0.77 V vs. Li/Li^+ (Fig. 4.22) without a conditioning cycle, two peaks are present in the discharge curve during the second cycle (0.89 and 0.79 V vs. Li/Li^+), but only one discharge peaks is present in the third cycle (0.89 V vs. Li/Li^+). During the charge cycle, two peaks are present at 1.01 and 1.1 V vs. Li/Li^+. When Cu_2Sb-Al_2O_3-C is cycled between OCV and 0.77 V vs. Li/Li^+ (Fig. 4.23) without a conditioning cycle, the peak in the discharge cycle is not well defined, but occurs at around 0.9 V vs. Li/Li^+. During the charge cycle, two peaks are present at 1.01 and 1.1 V vs. Li/Li^+, similar to when the material was cycled to 2.0 V rather than OCV V vs. Li/Li^+.

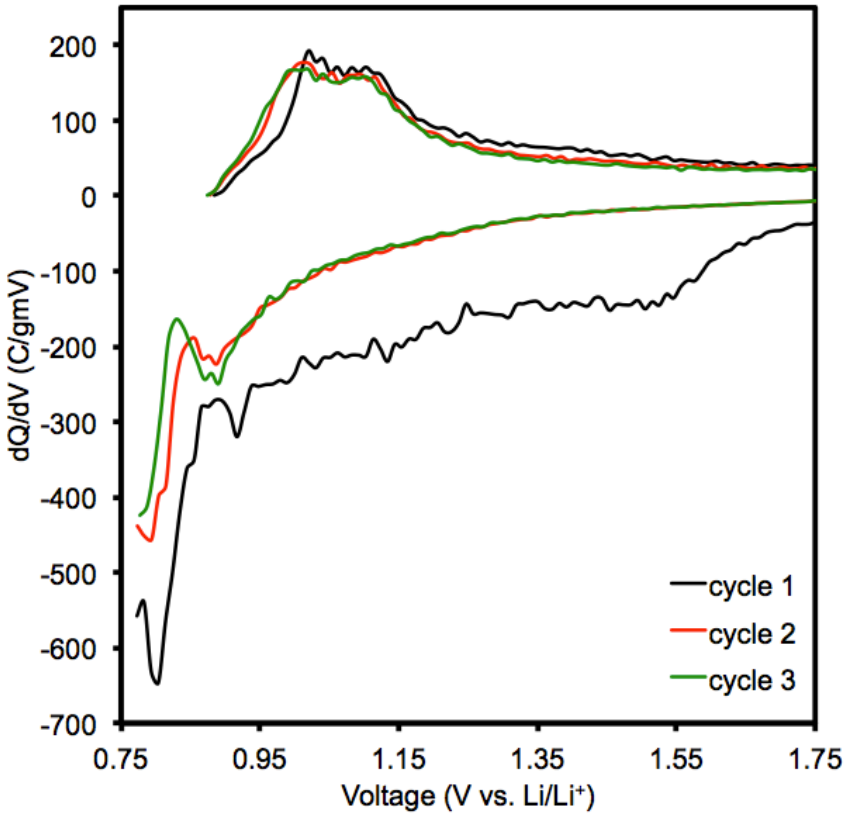

Figure 4.22. Differential capacity plot of Cu_2Sb-Al_2O_3-C cycled between the 2.0 and 0.77 V vs. Li/Li^+ without a conditioning cycle at 25 °C at a current rate of 100 mA/g of active electrode material.

When Cu_2Sb-Al_2O_3-C is cycled between 2 and 0.77 V vs. Li/Li^+ (Fig. 4.24) without a conditioning cycle, the DCP is substantially different from when no conditioning cycle was performed. Between 2 and 0.77 V vs. Li/Li^+ with a conditioning cycle, two distinct peaks are observed in the second discharge cycle (0.89 and 0.82 V vs. Li/Li^+), and three are observed in the charge cycle (0.93, 1.04, and 1.11 V vs. Li/Li^+). The peak at 0.93 V vs. Li/Li^+ is small, but clearly present. The appearance of one additional peak in the discharge curve and a corresponding appearance of two peaks in the charge curve indicate that the second step in the lithiation of Cu_2Sb-Al_2O_3-C proceeds in a different manner upon extraction. It is proposed that this asymmetric reaction is as

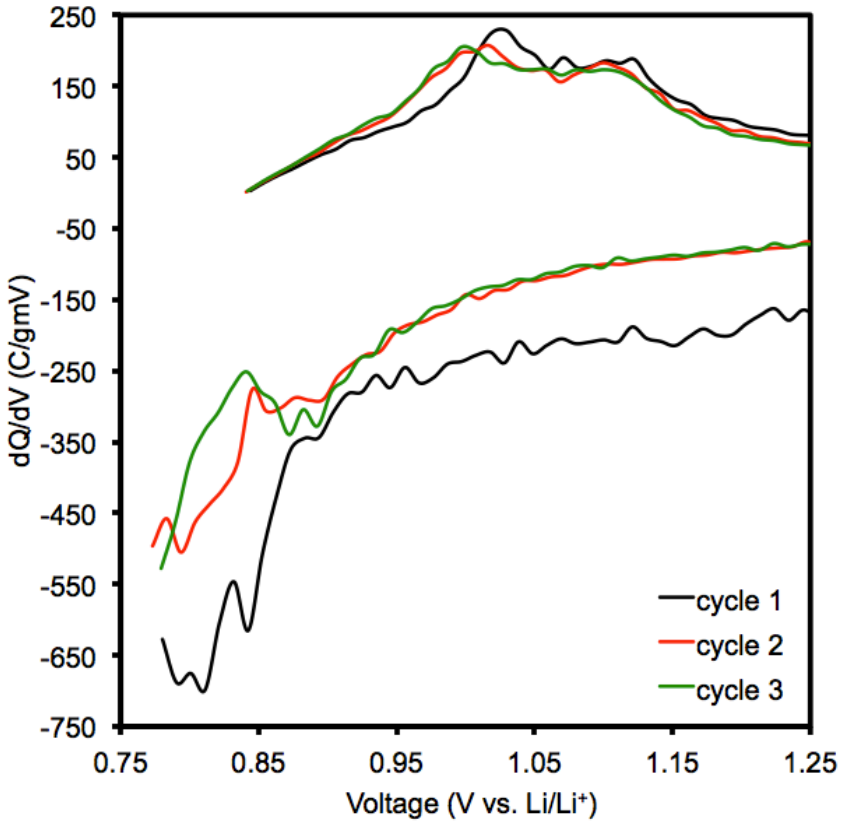

Figure 4.23. Differential capacity plot of Cu_2Sb-Al_2O_3-C cycled between the OCV and 0.77 V vs. Li/Li^+ without a conditioning cycle at 25 °C at a current rate of 100 mA/g of active electrode material.

follows: $LiCu_2Sb + Li^+ \rightarrow Li_2CuSb + Cu$ is separated into a two part reaction $Li_2CuSb \rightarrow LiCuSb + Li^+$ and $LiCuSb + Cu \rightarrow LiCu_2Sb$. In the asymmetric charge reactions, the removal of the Li^+ atom happens in a step that is distinct from the insertion of the Cu atom. Further analysis with more sophisticated techniques is necessary to support this claim.

The third reaction peak in the standard discharge cycle for Cu_2Sb-Al_2O_3-C occurs at 0.62 V vs. Li/Li^+. Judging from the standard DCP for Cu_2Sb-Al_2O_3-C, the third

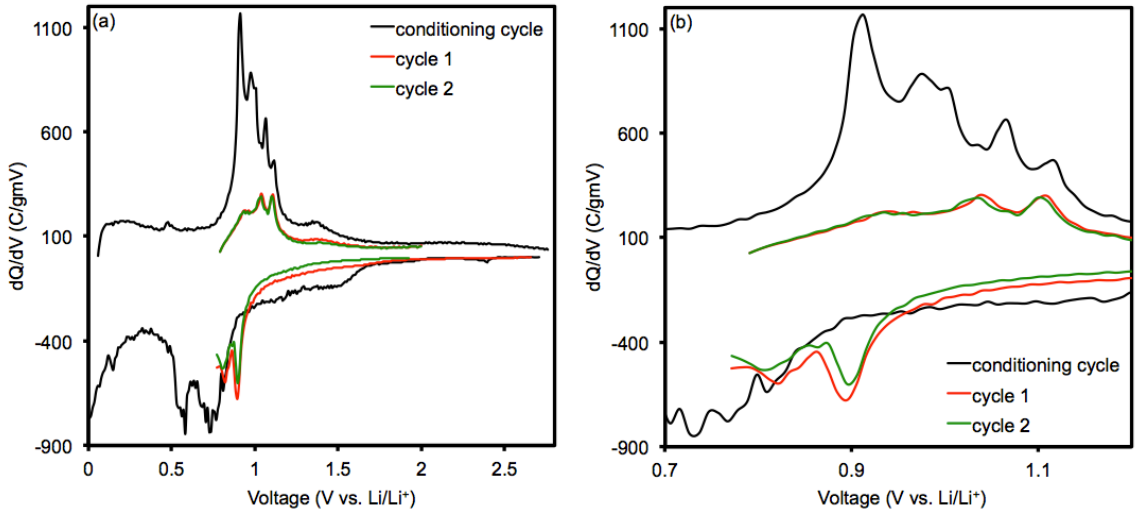

Figure 4.24. Differential capacity plot of Cu_2Sb-Al_2O_3-C cycled between the 2.0 and 0.77 V vs. Li/Li^+ with a conditioning cycle 25 °C at a current rate of 100 mA/g of active electrode material.

reaction is complete by 0.358 V vs. Li/Li^+, so cycle tests were performed between the 2.0 and 0.358 V vs. Li/Li^+ with (Fig. 4.24) and without (Fig. 4.25) a conditioning cycle. The cycle test between 2.0 and 0.358 V vs. Li/Li^+ with a conditioning cycle (Fig. 4.26) reveals the presence of the third discharge peak at 0.61 V vs. Li/Li^+, and the fourth charge peak at 0.89 V vs. Li/Li^+. The area under the third discharge and fourth charge peaks is greater than any of the other peaks, indicating that more energy is required to make that step in the reaction mechanism. This observation correlates well the fact that the third step in the proposed reaction mechanism ($Li_2CuSb + Li^+ \rightarrow Li_3Sb + Cu$) is a structural transformation, rather than a simple insertion of a lithium atom.

Figure 4.24 shows the DCP from cycling that was performed between 2.0 and 0.358 V vs. Li/Li^+ without a conditioning cycle. The peak locations of the cell that did not undergo a conditioning cycle closely match the peak locations from the cell that underwent a conditioning cycle. The peak locations are 0.90, 0.83, 0.61 V for discharge and 0.88, 1.00, 1.01, 1.11 V for charge for the cells without a conditioning cycle and 0.9,

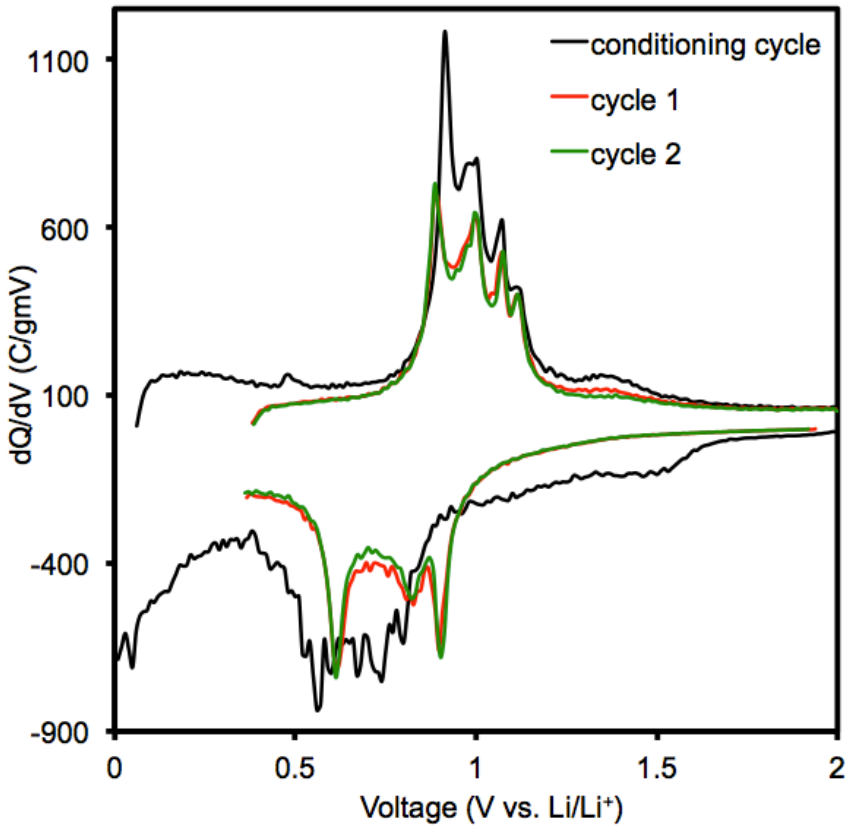

Figure 4.25. Differential capacity plot of Cu_2Sb-Al_2O_3-C cycled between the 2.0 and 0.358 V vs. Li/Li^+ with a conditioning cycle at 25 °C at a current rate of 100 mA/g of active electrode material.

0.83, 0.61 V for discharge and 0.89, 1.00, 1.08, 1.11 V for charge for the cell with a conditioning cycle. The similar peak locations for material discharged to 0.358 V vs. Li/Li^+ indicates that whatever morphological or structural changes that are happening to encourage reversibility of the reaction have already occurred by 0.358 V vs. Li/Li^+. This result means that Cu_2Sb-Al_2O_3-C can be effectively used as an anode material above 0.358 V vs. Li/Li^+. This voltage is significantly higher than the voltage at which graphite and silicon react with lithium and has implications for the inherent safety of the material.

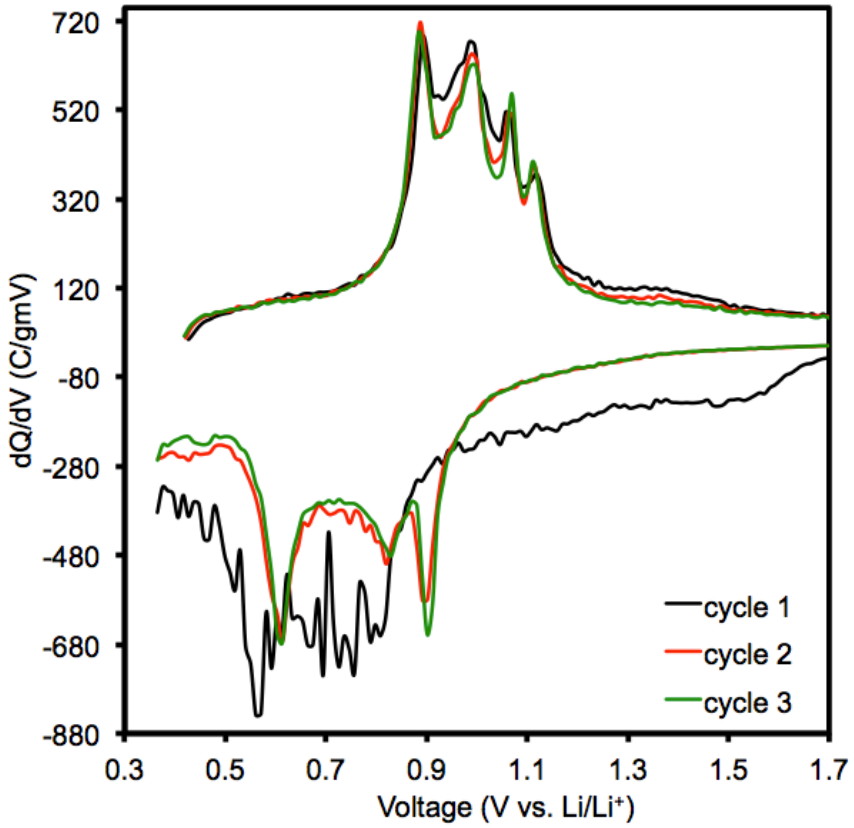

Figure 4.26. Differential capacity plot of Cu_2Sb-Al_2O_3-C cycled between the 2.0 and 0.358 V vs. Li/Li^+ without a conditioning cycle at 25 °C at a current rate of 100 mA/g of active electrode material.

Since *ex-situ* XRD was not effective at establishing the reaction mechanism for Cu_2Sb-Al_2O_3-C and lithium, but the DCPs show a clear correlation between cycle performance and reaction mechanism, the reaction mechanism must be studied more closely. For materials that are weakly crystalline or amorphous, Mössbauer, NMR, or X-ray absorption spectroscopy must be performed during cycling. Elucidation of the sequence of reactions during cycling could provide some important information about a material that shows a significant improvement in cycle performance over all other antimony-based alloy anode materials.

One of the drawbacks to using carbon anode materials alongside commercial $LiMn_2O_4$ spinel cathodes is the poisoning of the anode by the Mn^{2+} ions that dissolve from the cathode lattice during cycling. In order to test the resistance of Cu_2Sb-Al_2O_3-C to manganese poisoning, 3-electrode pouch cells were constructed with Cu_2Sb-Al_2O_3-C as the working electrode, a 4 V manganese spinel material as the counter electrode, and lithium metal as the reference electrode. The cycle performance of the Cu_2Sb-Al_2O_3-C material at 25 °C in the pouch cell does not change significantly from that of the coin cell, suggesting that Cu_2Sb-Al_2O_3-C anodes may be resistant to Mn^{2+} poisoning and can be used with manganese spinel cathodes in lithium-ion cells. The performance of the Cu_2Sb-Al_2O_3-C pouch cell at 25 °C is shown in Figure 4.27.

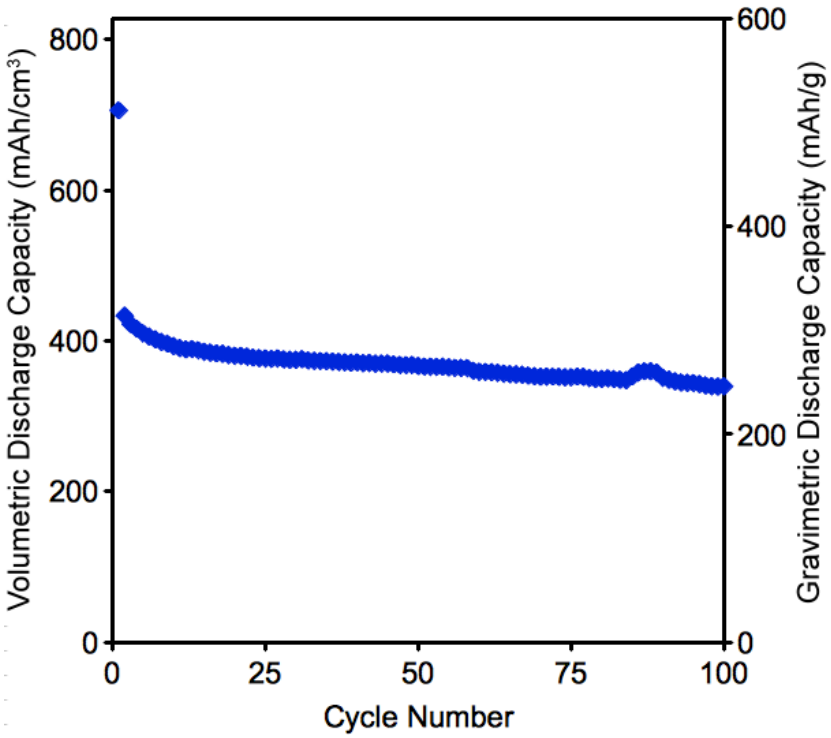

Figure 4.27. Cycle performance of a Cu_2Sb-Al_2O_3-C and $LiMn_2O_4$ spinel pouch cell at 25 °C between 0 – 2 V vs. Li/Li^+ at a current of 100 mA/g of active electrode material.

A test that is considered to be more representative of an anode compatibility with manganese-containing cathodes is the full cell performance at high temperature and 100% depth of discharge (DOD). The compatibility of Cu_2Sb-Al_2O_3-C with commercial manganese-containing spinel and layered cathode materials at 55 °C, 100 mA/g of active electrode material, cycled between 0 – 3.0 V vs. Li/Li^+ is shown in Figure 4.28. The issue of manganese dissolution and subsequent poisoning of graphite is one of the factors that inhibit the use of graphite anodes with many commercially viable Mn-based cathode materials. Figure 4.28 shows that even at high temperatures, Cu_2Sb-Al_2O_3-C has a stable

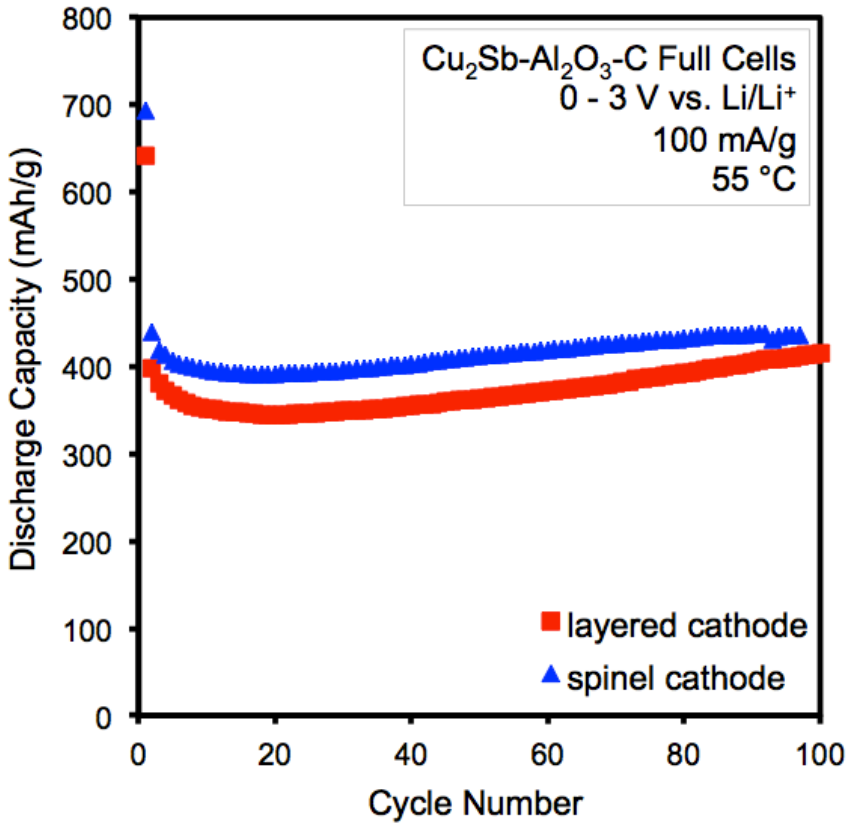

Figure 4.28. Cycle performance of full cells made with Cu_2Sb-Al_2O_3-C and layered manganese or manganese spinel cathode material at 55 °C between 0 – 3 V vs. Li/Li^+ at a current of 100 mA/g of active electrode material.

capacity for 100 cycles and is compatible with commercial manganese-containing cathode materials. The discharge capacity improves slightly over the course of 100 cycles. One possible reason for this is changes in pressure of the pouch cell. Much of the performance of a pouch cell depends upon creating good contact between all components of the cell. The full cell is cycled under compression of a hard plastic jig. The evolved gas from electrolyte decomposition could increase the pressure within the pouch cell over time, creating better contact between cell components and improving the cycle performance.

EIS measurements of Cu_2Sb-Al_2O_3-C and Cu_2Sb-C after 0, 1, and 20 cycles were performed in order to further understand the electrochemical performance, and the results are presented in Figure 4.29. The EIS data were analyzed based on the equivalent circuit and variables shown in Figure 4.29 [87]. R_u refers to uncompensated resistance between the working electrode and the lithium reference electrode, CPE_s refers to the constant phase element of the surface layer, R_s refers to the resistance of the SEI layer, CPE_{dl} refers to the CPE of the double layer, R_{ct} refers to the charge-transfer resistance, and Z_w refers to the Warburg impedance. Generally, the EIS spectrum can be divided into three frequency regions: low frequency, medium-to-low frequency, and high frequency, which correspond to cell geometric capacitance, charge transfer reaction, and lithium-ion diffusion through the surface layer, respectively. The slope of the impedance curve in the low frequency region is related to lithium-ion diffusion in the bulk of the active material.

Prior to cycling, Cu_2Sb-C has lower impedance than Cu_2Sb-Al_2O_3-C in all three ranges of frequency (Fig. 4.29(a)). This behavior is expected due to the fact that a larger weight percent of the Cu_2Sb-C electrode material is made up of a copper-containing species and the Al_2O_3 in the Cu_2Sb-Al_2O_3-C material is electronically insulating. Before either material is cycled, the curved portion of the impedance measurement is dominated

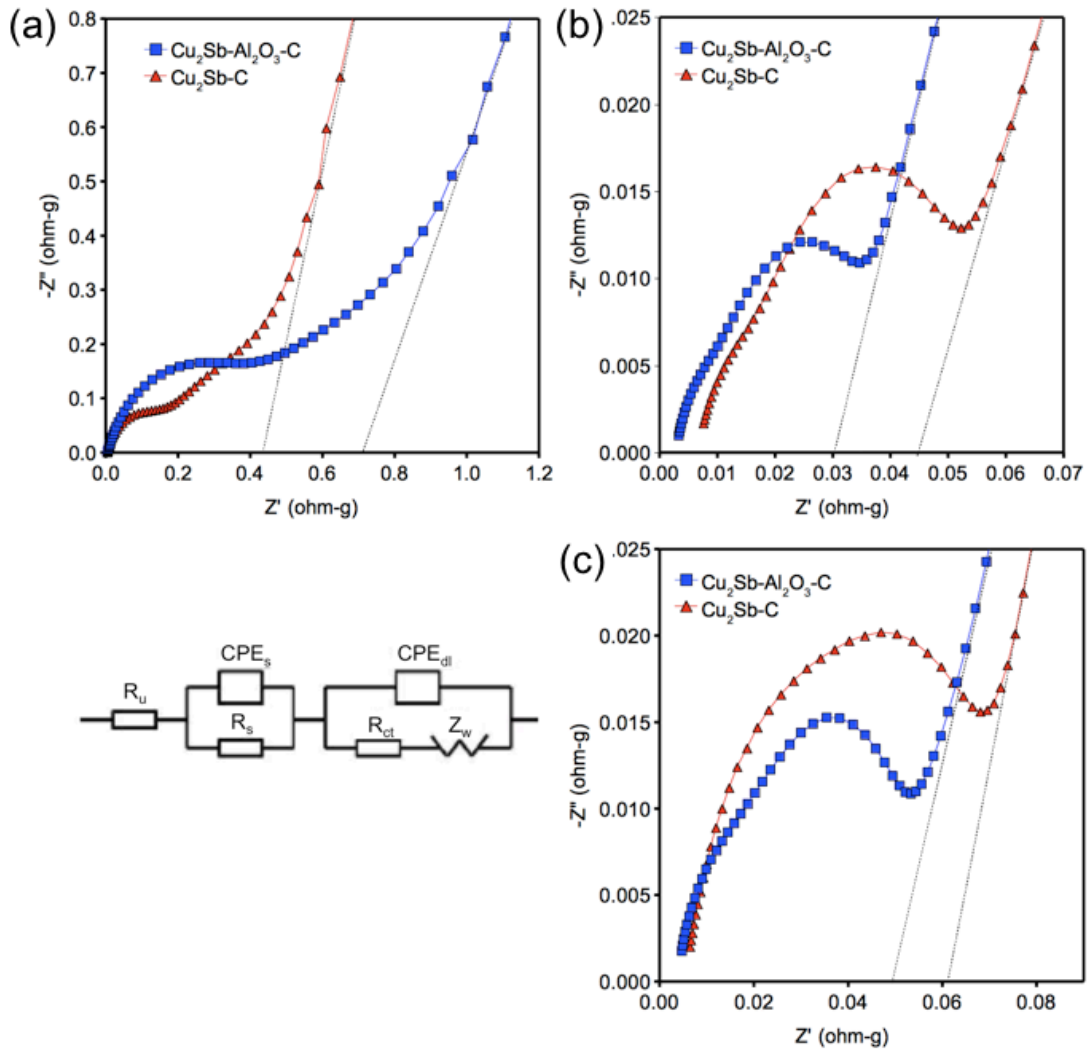

Figure 4.29. The equivalent circuit used for the impedance measurements and electrochemical impedance spectra (EIS) of the Cu_2Sb-Al_2O_3-C and Cu_2Sb-C nanocomposite materials (a) before cycling, (b) after the 1st cycle, and (c) after the 20th cycle.

by the charge-transfer resistance R_{ct}, which is related to the electrochemical reaction between particles or the reaction between the electrode and the electrolyte. After one cycle (Fig. 4.29(b)), the shape of the impedance curves for both materials changes. A semicircle is observed for each of the high and medium-to-low frequency ranges. The overall impedance of both materials has decreased compared to the values observed

before cycling, but the impedance of the Cu_2Sb-C is higher than that of Cu_2Sb-Al_2O_3-C in the medium-to-low and low frequency ranges. TEM images of both Cu_2Sb-C and Cu_2Sb-Al_2O_3-C show that the level of crystallinity in the materials increases during cycling. The TEM data on cycled materials are discussed in more detail in section 3.3. It is possible that the observed initial decrease in impedance for these materials is due to an increase in the ordering of the conductive, copper containing particles during cycling. After 20 cycles (Fig. 4.29(c)), the difference in the impedance response of Cu_2Sb-C and Cu_2Sb-Al_2O_3-C is even more significant, and Cu_2Sb-Al_2O_3-C exhibits lower resistance in all frequency ranges.

4.3.3 TEM and XRD of cycled electrodes

In order to understand the role of Al_2O_3 in providing a significant improvement in the cycle performance of Cu_2Sb-C, high-resolution TEM was performed on Cu_2Sb-Al_2O_3-C and Cu_2Sb-C electrodes that had been cycled for different numbers of cycles. Cu_2Sb-C was observed after 1, 50, and 247 cycles. 247 cycles was chosen as the stopping point for the Cu_2Sb-C cell because Cu_2Sb-C already lost over 50 % of its stable capacity after 247 cycles. Cu_2Sb-Al_2O_3-C was observed after 1, 50, and 500 cycles. At 500 cycles, the Cu_2Sb-Al_2O_3-C cell was still offering stable cycle performance.

The images in Figure 4.30(a) show that after one cycle, the Cu_2Sb-Al_2O_3-C material is largely amorphous. There are some small regions of crystallinity, but the Cu_2Sb particle boundaries are not well defined. After one cycle, the Cu_2Sb-C electrode shows well-defined boundaries of crystalline spherical Cu_2Sb particles (Fig. 4.30(b)). After 50 cycles, Cu_2Sb-Al_2O_3-C has developed areas of crystallinity. After 50 cycles, Cu_2Sb-C has almost completely transformed into crystalline spherical Cu_2Sb particles that are embedded in a carbon matrix. After 500 cycles, Cu_2Sb-Al_2O_3-C has retained 94

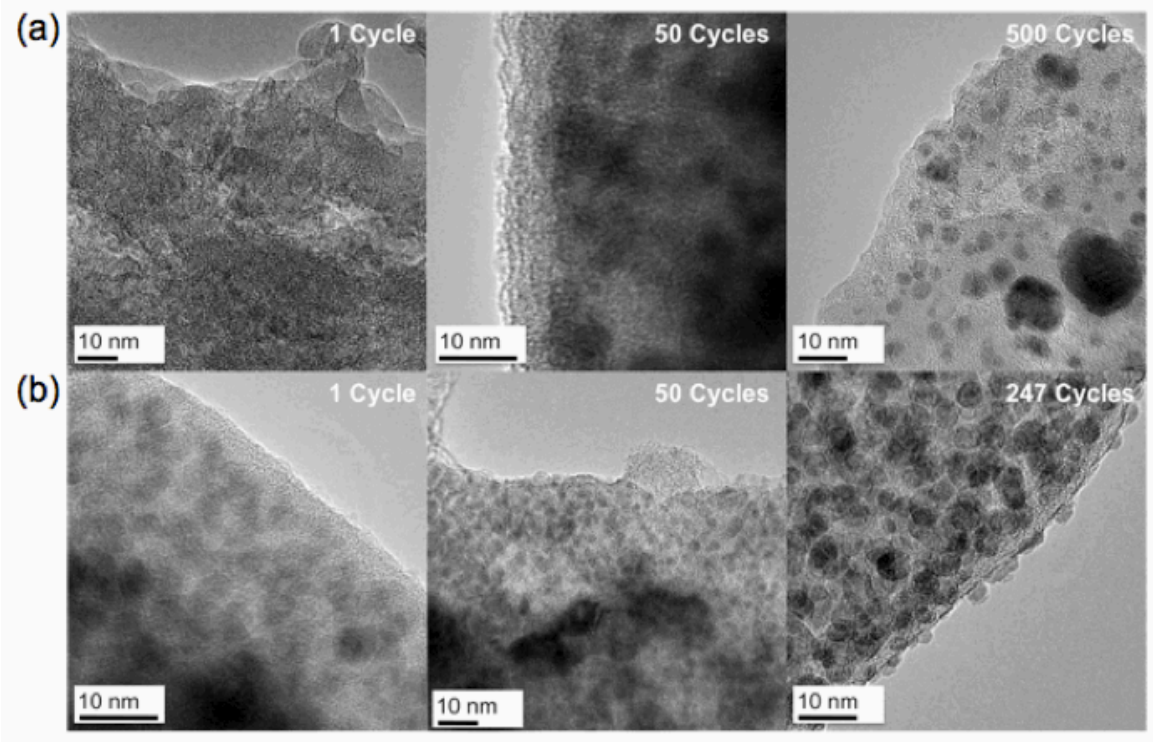

Figure 4.30. TEM images of electrode material after various numbers of cycles: (a) Cu_2Sb-Al_2O_3-C and (b) Cu_2Sb-C.

% of the capacity that was observed after 50 cycles and has transformed into well-defined, 2 – 10 nm crystalline Cu_2Sb particles that are almost entirely separate from one another and are surrounded by a matrix of Al_2O_3 and carbon. After 247 cycles, the Cu_2Sb-C material has already lost over 50 % of the capacity that was observed at cycle 50. The size of the Cu_2Sb-C particles does not significantly change between cycles 50 and 247, but the Cu_2Sb-C particles appear to be tightly agglomerated after 247 cycles. The XRD patterns of cycled Cu_2Sb-Al_2O_3-C electrodes after 1, 50, and 500 cycles support the notion that the degree of crystallinity of the Cu_2Sb particles within the Cu_2Sb-Al_2O_3-C increases with the number of cycles (Fig. 4.31).

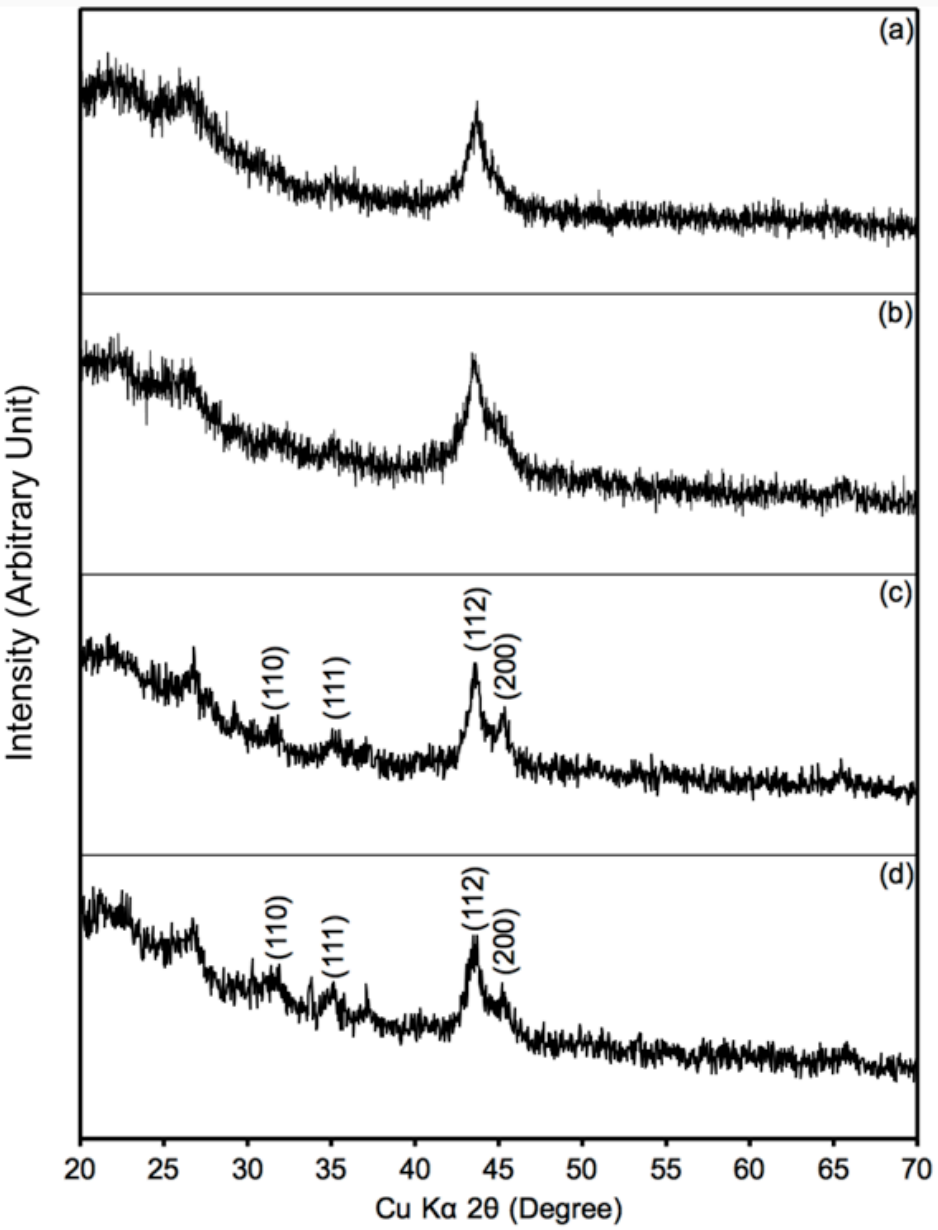

Figure 4.31. *Ex-situ* XRD of Cu_2Sb-Al_2O_3-C electrodes (a) before cycling, (b) after 1 cycle, (c) after 50 cycles, and (d) after 500 cycles.

4.4 CONCLUSIONS

The Cu_2Sb-C alloy anode was found to show stable cycle performance only to ~ 100 cycles. Through the incorporation of Al_2O_3 into the alloy anode to form Cu_2Sb-

Al_2O_3-C, the stable cycle performance was extended from 100 to 500 cycles. The presence of Al_2O_3 did not significantly change the Cu_2Sb particle size or outer morphology of the Cu_2Sb particles. However, prior to cycling, the Cu_2Sb particles in Cu_2Sb-C material were found to be more well defined than that in Cu_2Sb-Al_2O_3-C. After one cycle and after 20 cycles, the Cu_2Sb-Al_2O_3-C material showed lower surface, charge-transfer, and bulk resistances than those of Cu_2Sb-C. The Cu_2Sb-Al_2O_3-C material had a significant first-cycle irreversible capacity loss (199 mAh/g) when cycled between 0 – 2 V vs. Li/Li^+, but showed remarkable capacity retention over 500 cycles (326 mAh/g, 456 mAh/cm^3). The high-resolution TEM images of the cycled electrode materials showed that the presence of Al_2O_3 slows down the development of crystalline Cu_2Sb particles within the nanocomposite during cycling but does not significantly influence the Cu_2Sb particle size or morphology. The carbon in the matrix allows the Cu_2Sb particles to remain separate yet electronically connected within the nanocomposite during cycling. The Al_2O_3 in the composite is an ionic conductor and improves the diffusion of lithium within the Cu_2Sb-Al_2O_3-C material. Thus, both the carbon and the Al_2O_3 aid in reducing Cu_2Sb particle agglomeration and providing the exceptional cycle life and lower impedance than are observed with Cu_2Sb-C. The weakly crystalline nature of the Cu_2Sb-Al_2O_3-C material provides a challenge in determining the phase changes that occur during lithiation/delithiation. Studies on cycle performance within windows of limited potential showed that the insertion and extraction of lithium into Cu_2Sb-Al_2O_3-C is not a symmetric reaction. More detailed research needs to be carried out in order to investigate the precise reaction mechanism of Cu_2Sb-Al_2O_3-C with lithium.

The coulombic efficiency and first cycle irreversible capacity loss were greatly improved when the synthesis milling time for Cu_2Sb-Al_2O_3-C was doubled from 12 to 24 h. Optimization experiments with the carbon content of the composite showed that while

the tap density increases, the cycle life degrades as the carbon content decreases. The Cu_2Sb-Al_2O_3-C nanocomposite material also performed well in full pouch cell arrangements at high temperature with commercial cathodes containing manganese as the Cu_2Sb-Al_2O_3-C alloy anodes are resistant to dissolved manganese poisoning.

Chapter 5: Cu_6Sn_5-TiC-C Nanocomposite Anode Material

5.1 INTRODUCTION

With an aim to improve the gravimetric and volumetric capacities as well as cycle life, this chapter presents a systematic investigation of the Cu_6Sn_5-TiC-C nanocomposite, encompassing the active-inactive and nanostructured strategies together. The nanocomposites are prepared by furnace heating of a mixture of Cu, Sn, and Ti metals, followed by a simple high-energy mechanical milling (HEMM) of the Sn–Ti-Cu alloys and carbon. The ultrafine Cu_6Sn_5 particles dispersed in the TiC + C matrix are characterized by X-ray diffraction (XRD), *ex-situ* XRD, scanning electron microscopy (SEM), transmission electron microscopy (TEM), scanning transmission electron microscopy (STEM), X-ray photoelectron spectroscopy (XPS), and electrochemical charge–discharge measurements including impedance analysis.

5.2 EXPERIMENTAL

The Cu_6Sn_5-TiC-C nanocomposite was prepared as described below. First, a mixture of Cu-Sn-Ti alloy phases were obtained by heating a mixture of Sn (99.8%, < 45 μm, Aldrich), Cu (99 %, 45 μm Acros Organics), and Ti (99.99%, ~325 mesh, Alfa Aesar) powders in an atomic ratio of 3 : 1 : 5 at 900 ºC in a flowing Argon atmosphere for 12 h. The mixture of Cu-Sn-Ti phases was then mixed with 20 wt. % acetylene black and subjected to high energy mechanical milling (HEMM) for 40 h at a speed of 500 rpm in a vibratory mill at ambient temperature under argon atmosphere to obtain the Cu_6Sn_5-TiC-C nanocomposite.

The samples were characterized with a Rigaku Ultima IV X-ray diffractometer with Cu Kα radiation, Hitachi S-5500 STEM, and JEOL 2010 TEM operating at 300 kV. The STEM and TEM samples were prepared by dispersing the sample in ethanol,

depositing it dropwise onto a carbon-coated copper grid, and removing the ethanol at ambient temperature. Surface characterization was performed on the Cu_6Sn_5-TiC-C powder with a Kratos X-ray photoelectron spectrometer (XPS) with a monochromatic Al Kα source. The surface of the XPS sample was cleaned of surface oxides and other contamination by sputtering with a 4 keV beam energy and an extractor current of 75 μA for 300 seconds. The electrodes for the electrochemical evaluation were prepared and tested according to details listed in chapter 2.2.6. The discharge–charge experiments were performed galvanostatically at a constant current density of 100 mA/g of active material within the voltage range of 0 – 2.0 V vs. Li/Li^+ or 0.2 V – OCV vs. Li/Li^+. Cycle testing was performed at 25 ºC. To investigate the structural changes that may occur during electrochemical cycling, *ex-situ* XRD data were collected with a Rigaku Ultima IV X-ray diffractometer at a current rate of 100 mA/g of active material. Electrochemical cycle testing at 55 ºC was also performed with full, coffee-bag type cells with spinel manganese oxide cathodes and layered nickel-manganese-cobalt oxide cathodes with lithium metal as the reference electrode at a constant current density of 100 mA/g of active material within the voltage range of 0.2 – OCV vs. Li/Li^+. The electrodes for *ex-situ* XRD evaluation were prepared by mixing 70 wt. % active material (Cu_6Sn_5-TiC-C) powder, 15 wt. % carbon black (Super P), and 15 wt. % polytetrafluoroethylene (PTFE) with several drops of 2-propanol. The electrodes were pressed into copper mesh and dried at 120 ºC overnight under vacuum. Tap density measurements were made with a Quantachrome AT-4 Autotap machine.

Electrochemical impedance spectroscopic analysis (EIS) was conducted according to the methods detailed in in chapter 2.2.6.

5.3 RESULTS AND DISCUSSION

5.3.1 Structural, morphological, and surface characterization

Figure 5.1 shows the XRD pattern of the Cu_6Sn_5-TiC-C sample. The sample exhibits peaks corresponding to crystalline Cu_6Sn_5 (JCPDS No. 00-045-1488) and TiC (JCPDS No. 00-032-1383) and confirms the formation of Cu_6Sn_5 and TiC. The carbon in

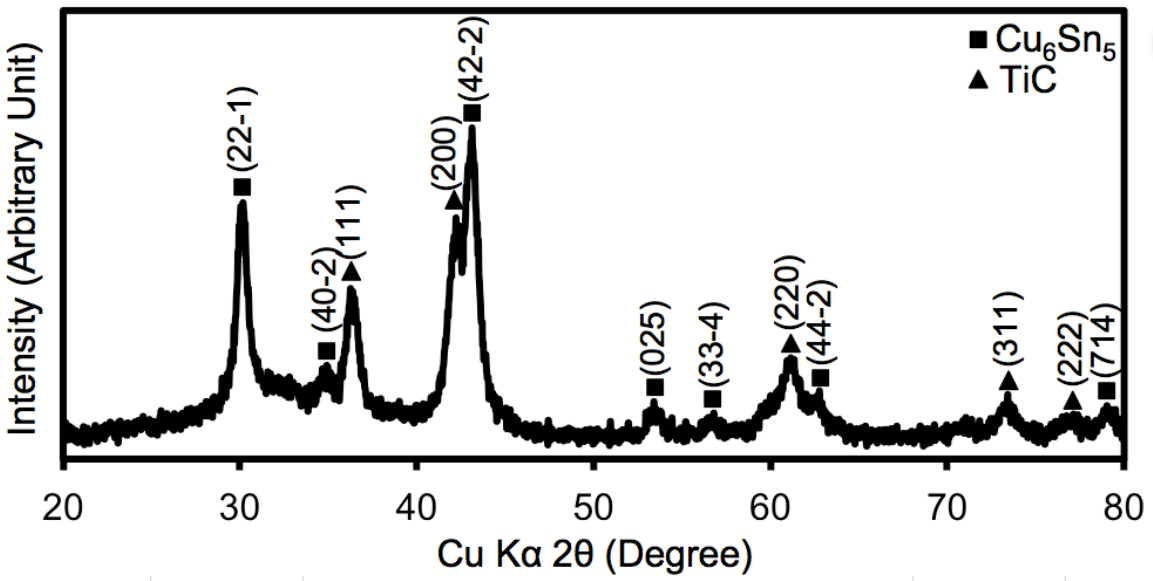

Figure 5.1. XRD patterns of Cu_6Sn_5-TiC-C nanocomposite obtained by the mechanochemical reduction reaction.

the composite is not highly crystalline and does not appear in the XRD pattern.

Figure 5.2 shows the SEM, TEM, and STEM element mapping images of the Cu_6Sn_5-TiC-C nanocomposite. The SEM image in Figure 5.2(a) shows the large particles of carbon (acetylene), with the smaller Cu_6Sn_5 and TiC particles blended and stuck to the carbon. The TEM image in Figure 5.2(b) shows the highly crystalline nature of a ~ 30 nm Cu_6Sn_5 particle. The particle in the TEM image appears to be coated with a layer of

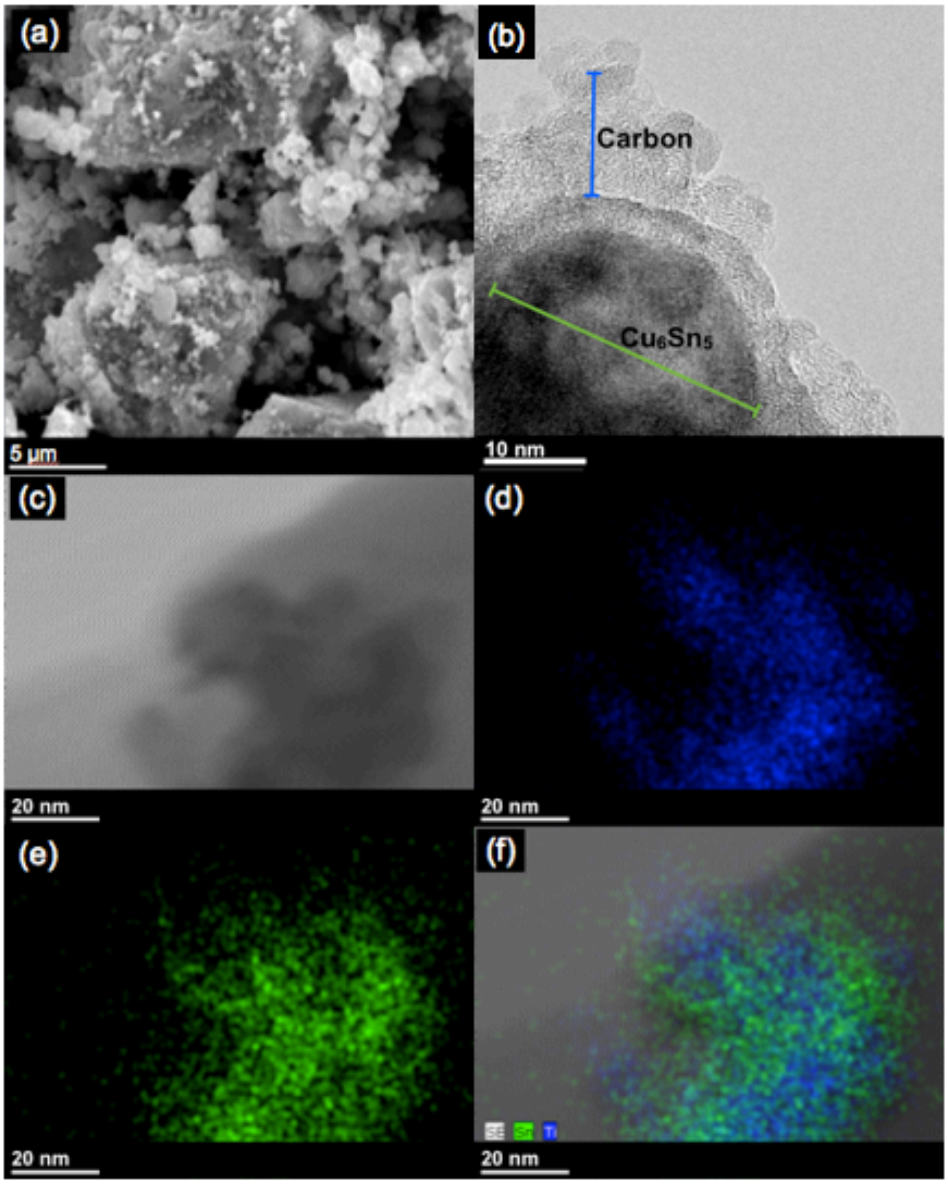

Figure 5.2. Images and element mapping of Cu_6Sn_5-TiC-C: (a) SEM, (b) TEM, (c) STEM, (d) element map of Ti, (e) element map of Sn, and (f) a composite element map of Ti and Sn.

either carbon or TiC, but lattice fringes could not be observed for TiC. The distribution of particle sizes observed via TEM was between 10 and 200 nm. The STEM images shown in Figure 5.2(d-f) reveal presence of Ti on the Cu_6Sn_5 particles. The TiC does not

appear to be a homogenous coating on the particles but rather is present as heterogeneous marbling on the outside of the particles.

XPS analysis showed that some tin oxide and titanium oxide impurities were present in the Cu_6Sn_5-TiC-C material. Table 5.1 shows the binding energy values for tin and titanium in the sample. Because the binding energies of SnO or SnO_2 are similar, the XPS data could not be used to differentiate between them in the sample.

Peak	Binding Energy (eV)	Phase
(1) Sn $3d^{5/2}$	486.5	SnO or SnO_2
(2) Sn $3d^{5/2}$	484.8	Cu_6Sn_5
(1) Ti $2p^{3/2}$	455.1	TiC
(2) Ti $2p^{3/2}$	458.3	TiO_2

Table 5.1. Binding energies of Sn and Ti binding in the Cu_6Sn_5-TiC-C nanocomposite.

5.3.2 Electrochemical characterization

The voltage profile and differential capacity plot of the Cu_6Sn_5-TiC-C nanocomposite are shown in Figure 5.3. When cycled between 0 and 2 V vs. Li/Li^+, the nanocomposite exhibits first gravimetric discharge and charge capacities of, respectively, 797 and 629 mAh/g. When the material is cycled between 0.2 V vs. Li/Li^+ and the open circuit voltage (OCV) for the material, the first gravimetric discharge and charge capacities are, respectively, 321 mAh/g and 225 mAh/g. When the operating voltage window is limited to 0.2 – OCV vs. Li/Li^+ for the material, the irreversible capacity loss is 96 mAh/g and the coulombic efficiency is around 70 %. The irreversible capacity loss may be largely associated with the reduction of the electrolyte on the active material surface and the formation of solid-electrolyte interphase (SEI) layer [1]. The voltage profile for Cu_6Sn_5-TiC-C closely resembles the gradual sloping that was observed in the

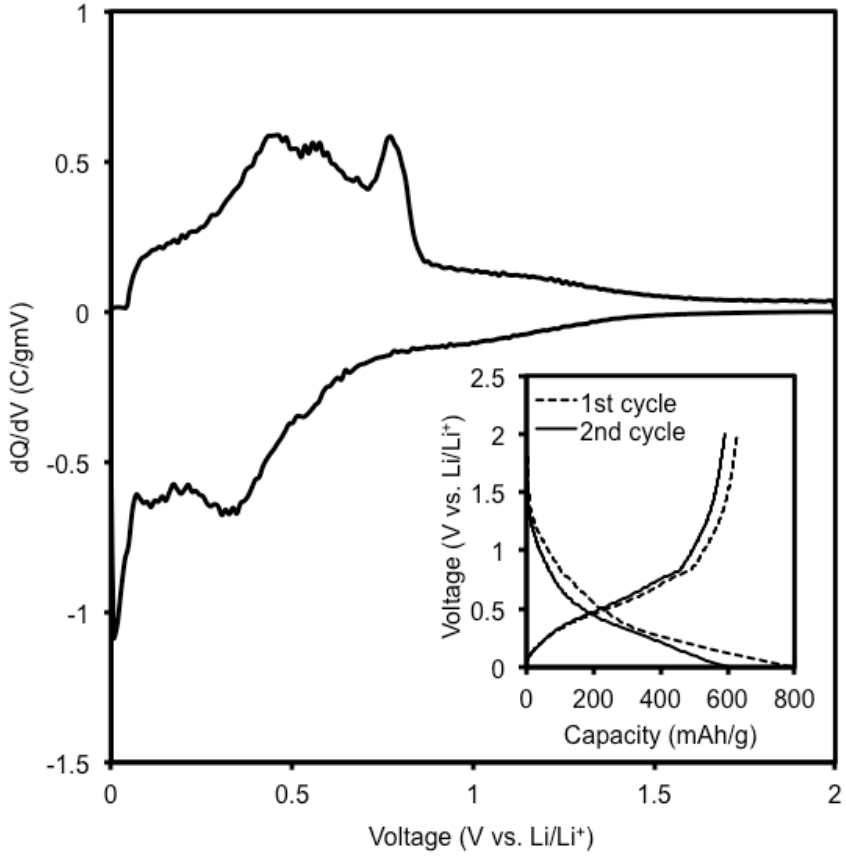

Figure 5.3. Voltage profiles and differential capacity plot of the second cycle for Cu_6Sn_5-TiC-C at 25 °C and a current of 100 mA/g of active electrode material between 0 – 2 V vs. Li/Li^+.

work of Thorne *et al* [28] on amorphous/nanostructured Cu_6Sn_5-C. The voltage plateaus for the two-phase regions that are normally observed for Cu_6Sn_5 are not observed when Cu_6Sn_5 is nanostructured. Figure 5.3 shows that the Cu_6Sn_5-TiC-C sample does not undergo a two-phase transition during cycling. When Cu_6Sn_5-TiC-C is cycled down to 0 V vs. Li/Li^+, the major peaks in the differential capacity plot (Fig. 5.3) occur around 0.35 and 0.13 V vs. Li/Li^+. When the sample is cycled between 0.2 V vs. Li/Li^+ and the open circuit voltage (OCV) of the material, only one peak is observed at around 0.31 V vs. Li/Li^+ in the discharge cycle (inset in Fig. 5.4).

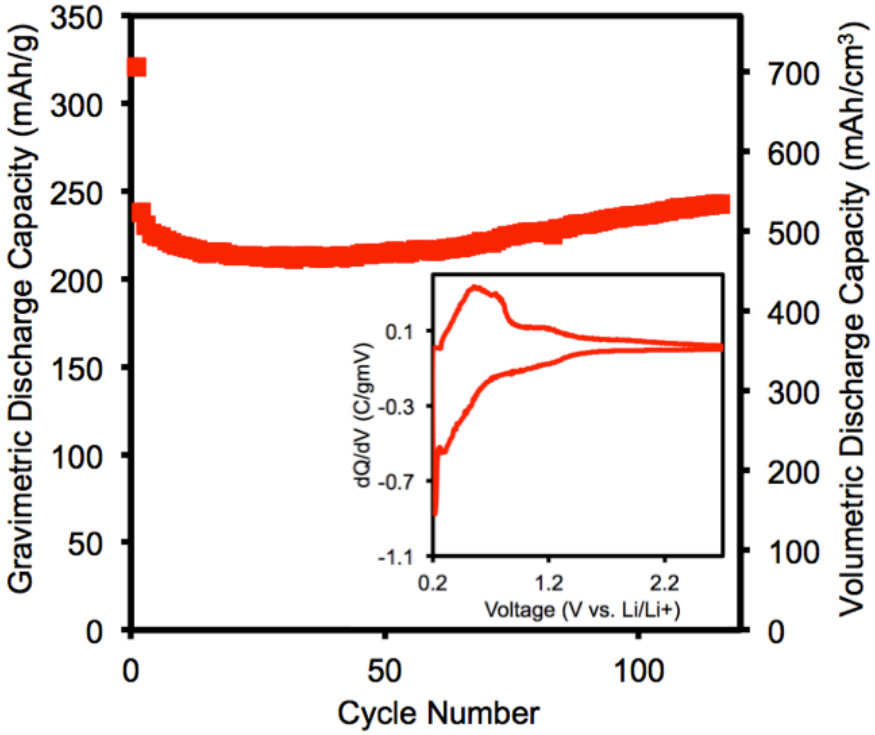

Figure 5.4. Volumetric and gravimetric discharge capacities of Cu_6Sn_5-TiC-C and commercial graphite from 0.2 – 2.7 V (OCV) vs. Li/Li^+ at 25 °C and a current rate of 100 mA/g of active electrode material and a differential capacity plot of the second cycle (inset).

This change in the differential capacity plot and the corresponding reduction in capacity indicates that when the material is discharged down to 0.2 V vs. Li/Li^+, the reaction of lithium with Cu_6Sn_5 is not complete. However, when the lower potential is set at 0.2 V vs. Li/Li^+ rather than 0 V vs. Li/Li^+, an improvement in the cycle performance of Cu_6Sn_5-TiC-C is observed (Fig. 5.4). The improvement in cycle life when the Cu_6Sn_5 material is kept above 0.2 V vs. Li/Li^+ is likely due to the avoidance of the significant structural changes that occur when the final Cu is extruded from the Cu_6Sn_5 material and $Li_{4.4}Sn$ is formed.

In order to investigate the structural changes that occur during electrochemical cycling, XRD data were collected on electrodes that had been cycled and then extracted from the cells. *Ex-situ* XRD patterns recorded with electrodes at various points in the discharge/charge cycle are shown in Figure 5.5. The peaks for the Cu_6Sn_5 phase gradually decrease in intensity during discharge to 0.07 V vs. Li/Li^+, and then completely

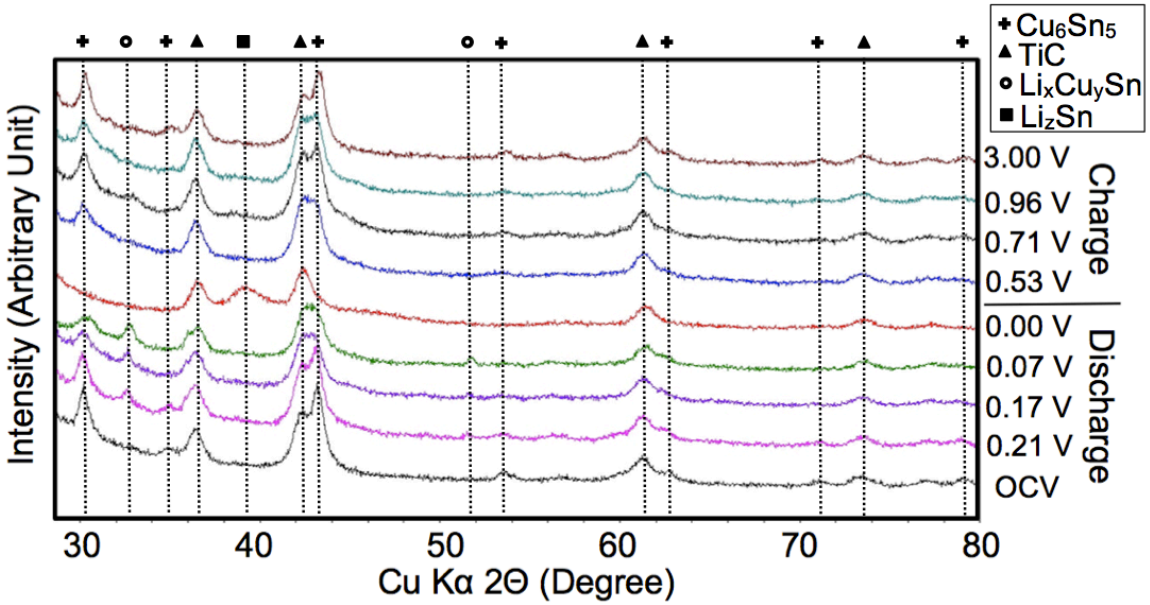

Figure 5.5. *Ex-situ* XRD patterns of Cu_6Sn_5-TiC-C during charge-discharge: Li_xCu_ySn represents the intermediate phases where $0 < y < 1$ and x gradually increases during discharge. Li_zSn represents a $Li_{4.4}Sn$-like phase.

disappear upon full discharge to 0.0 V vs. Li/Li^+. The Cu_6Sn_5 peaks then reappear during the charge cycle. The decomposition and reformation of the Cu_6Sn_5 phase is consistent with the previously published results. The TiC phase is present at all points during the cycle and is inactive towards lithium. At full discharge, the Li-Sn phase that appears has an XRD peak at approximately 39°, which corresponds to a phase that is nearly $Li_{4.4}Sn$. When Cu_6Sn_5-TiC-C is discharged to 0.21, 0.17, and 0.07 V vs. Li/Li^+, two peaks emerge

at around 33° and 52°. These two peaks are thought to correspond to an intermediate Li_xCu_ySn phase where $0 < y < 1$ and x gradually increases during discharge. These two peaks disappear when the material is fully discharged. Based upon the *ex-situ* XRD data and the fact that the voltage profile for Cu_6Sn_5-TiC-C does not contain any distinct plateaus, the reaction mechanism for the Cu_6Sn_5-TiC-C nanocomposite is thought to be a gradual blend of the following two reactions:

$$10\ Li + Cu_6Sn_5 \rightarrow 5\ Li_2CuSn + Cu \quad (5.1)$$

$$2.2\ Li + Li_2CuSn \rightarrow Li_{4.4}Sn + Cu \quad (5.2)$$

The two steps of the reaction do not happen in a stepwise fashion. Rather, the two steps of the reaction of the Cu_6Sn_5-TiC-C material with lithium occur somewhat simultaneously. This blended reaction mechanism is consistent with what has been published by Thorne *et al* [28] for the amorphous/nanostructured Cu_6Sn_5-C material. When the material is only discharged to 0.2 V vs. Li/Li^+, step two of the above reaction mechanism does not occur, and Cu_6Sn_5-TiC-C does not experience the significant structural change that accompanies the transition from Li_xCu_ySn phases to the $Li_{4.4}Sn$-like phase as the final Cu atoms are extruded.

Figure 5.6 compares the cyclability of Cu_6Sn_5-TiC-C and graphite at different temperatures and rates of charge. When Cu_6Sn_5-TiC-C is cycled between 0 – 2.0 V vs. Li/Li^+ at 25 °C and 100 mA/g of active electrode material, it shows a volumetric discharge capacity that is four times that of graphite and stable for 70 cycles. The cycle performance of Cu_6Sn_5-TiC-C at 55 °C and 100 mA/g is compared with graphite in Figure 5.6(c). At 55 °C, the cycle performance of Cu_6Sn_5-TiC-C is less stable than at 25 °C, but the volumetric discharge capacity is still greater than three times the volumetric capacity of graphite. Figure 5.6(d) compares the excellent rate capability of the Cu_6Sn_5-

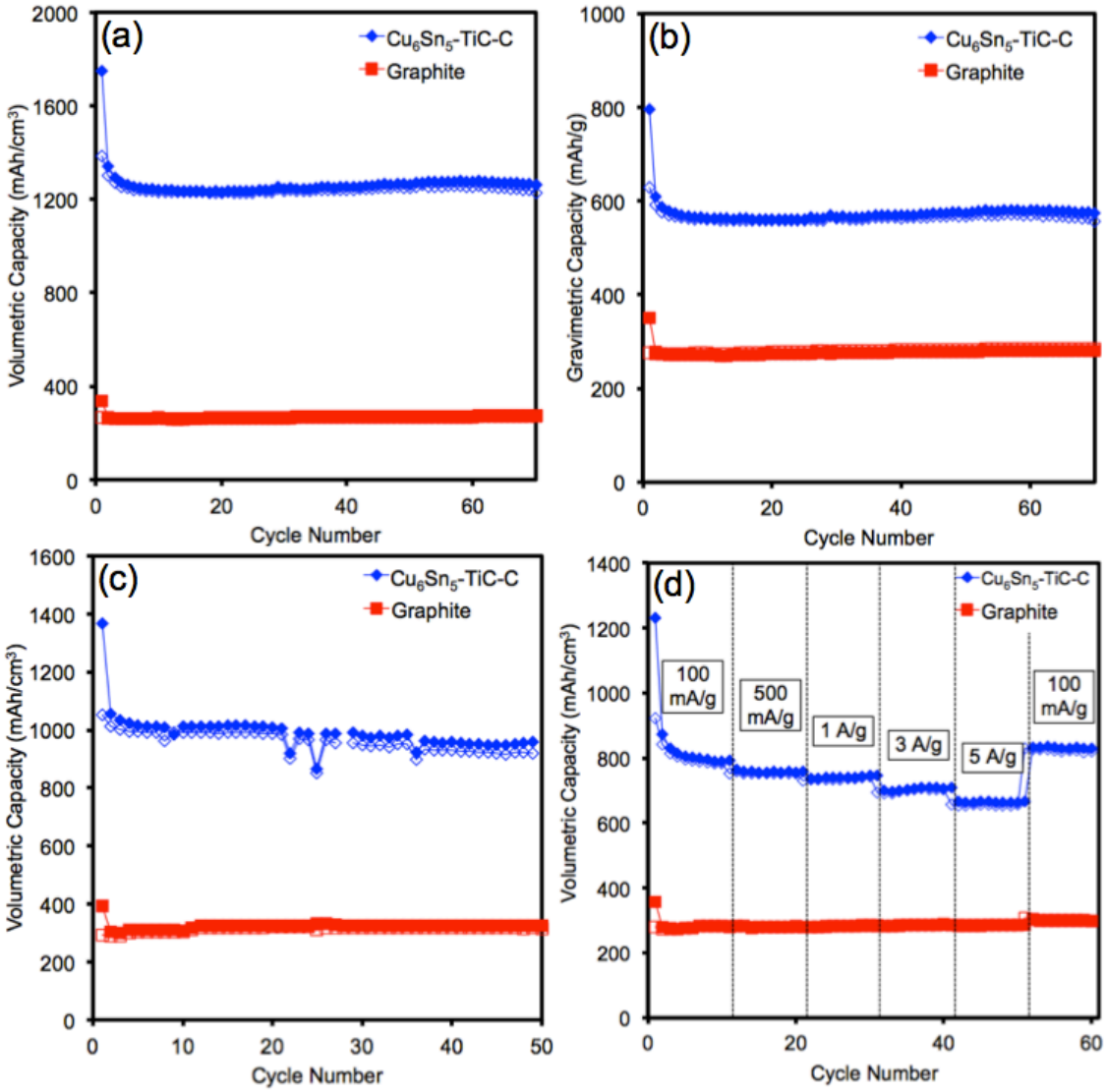

Figure 5.6. Cu_6Sn_5-TiC-C and commercial graphite comparisons: (a) Volumetric discharge capacity, (b) gravimetric discharge, (c) volumetric discharge capacity at 55 °C, and (d) rate capability at various current rates. All current rates were between 0 – 2 V vs. Li/ Li^+ at 25 °C and 100 mA/g of active electrode material unless otherwise indicated.

TiC-C nanocomposite with that of graphite. Even at a rate of 5 A/g of active material, Cu_6Sn_5-TiC-C shows high capacity.

The compatibility of Cu_6Sn_5-TiC-C with commercial manganese-containing spinel and layered cathode materials at 55 °C, 100 mA/g of active electrode material, cycled between 0.2 – 2.8 V vs. Li/Li^+ is shown in Figure 5.7. The potential window was limited to 0.2 – 2.8 V vs. Li/Li^+ in order to reduce the impact of structural changes and manganese poisoning on the cycle performance. The issue of manganese dissolution and subsequent poisoning of graphite is one of the factors that inhibit the use of graphite anodes with many commercially viable Mn-based cathode materials. Figure 5.7 shows that even at high temperatures, Cu_6Sn_5-TiC-C has a stable capacity for 200 cycles and is compatible with commercial manganese-containing cathode materials. The capacity of both full cells improves slightly after the 100^{th} cycle, and this is consistent with the performance of the half-cells when the cells are cycled above 0.2 V vs. Li/Li^+.

To gain insight into the electrochemical performance of Cu_6Sn_5-TiC-C, EIS measurements were conducted at 2 V vs. Li/Li^+ before cycling, after the 1st cycle, and after the 20th cycle. The EIS data were analyzed based on an equivalent circuit given in Figure 5.8 [87]. In Figure 5.8, R_u refers to uncompensated resistance between the working electrode and the lithium reference electrode, CPE_s refers to the constant phase element of the surface layer, R_s refers to the resistance of the SEI layer, CPE_{dl} refers to the constant phase element of the double layer, R_{ct} refers to the charge-transfer resistance, and Z_w refers to the Warburg impedance. Generally, the EIS spectrum can be divided into three frequency regions, *i.e.*, low frequency, medium-to-low- frequency, and high-frequency regions, which correspond, respectively, to the geometric capacitance of the cell, the charge-transfer reaction, and the lithium-ion diffusion through the surface layer. The EIS spectra recorded before cycling, after one cycle, and after 20 cycles in Figure 5.8

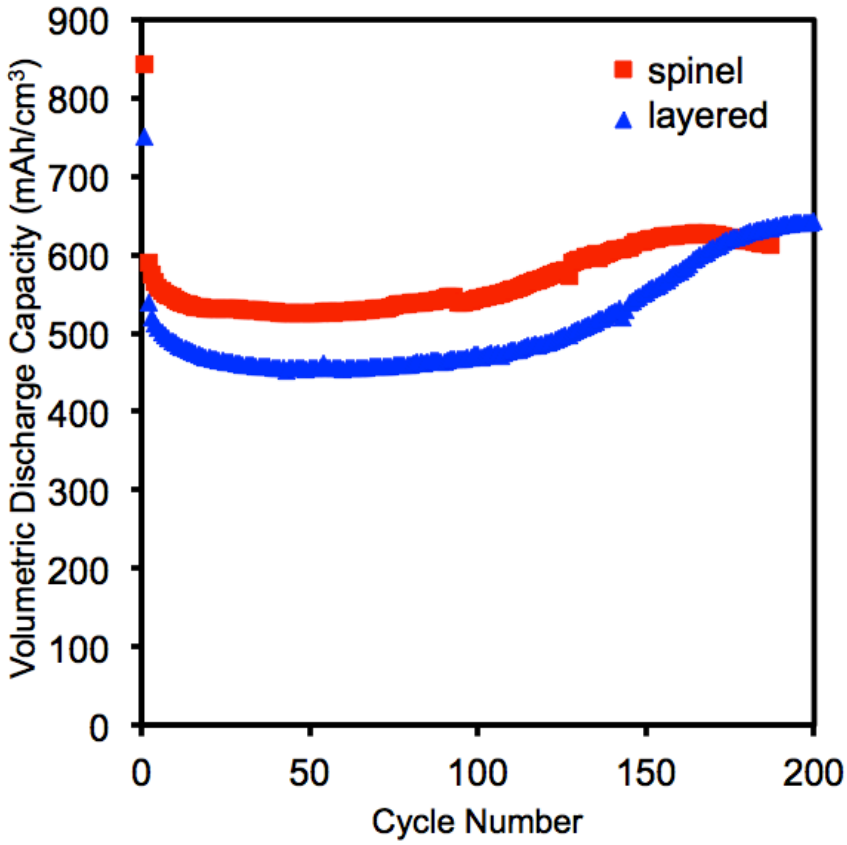

Figure 5.7. Cycle performance of cells fabricated with the Cu_6Sn_5-TiC-C anode and two commercial manganese-containing cathode materials (spinel and layered) at 55 °C, 100 mA/g of active electrode material, between 0.2 – 2.8 V vs. Li/Li^+.

consist of two semicircles and a line. The diameter of the semicircle in the high-frequency region (lowest Z' values) is a measure of the resistance R_s of the SEI layer. The diameter of the semicircle in the medium-frequency region (middle Z' values) is a measure of the charge-transfer resistance R_{ct}, which is related to the electrochemical reaction between the particles or between the electrode and the electrolyte. The portion of the impedance curve that has a linear slope is related to lithium-ion diffusion in the bulk of the active material.

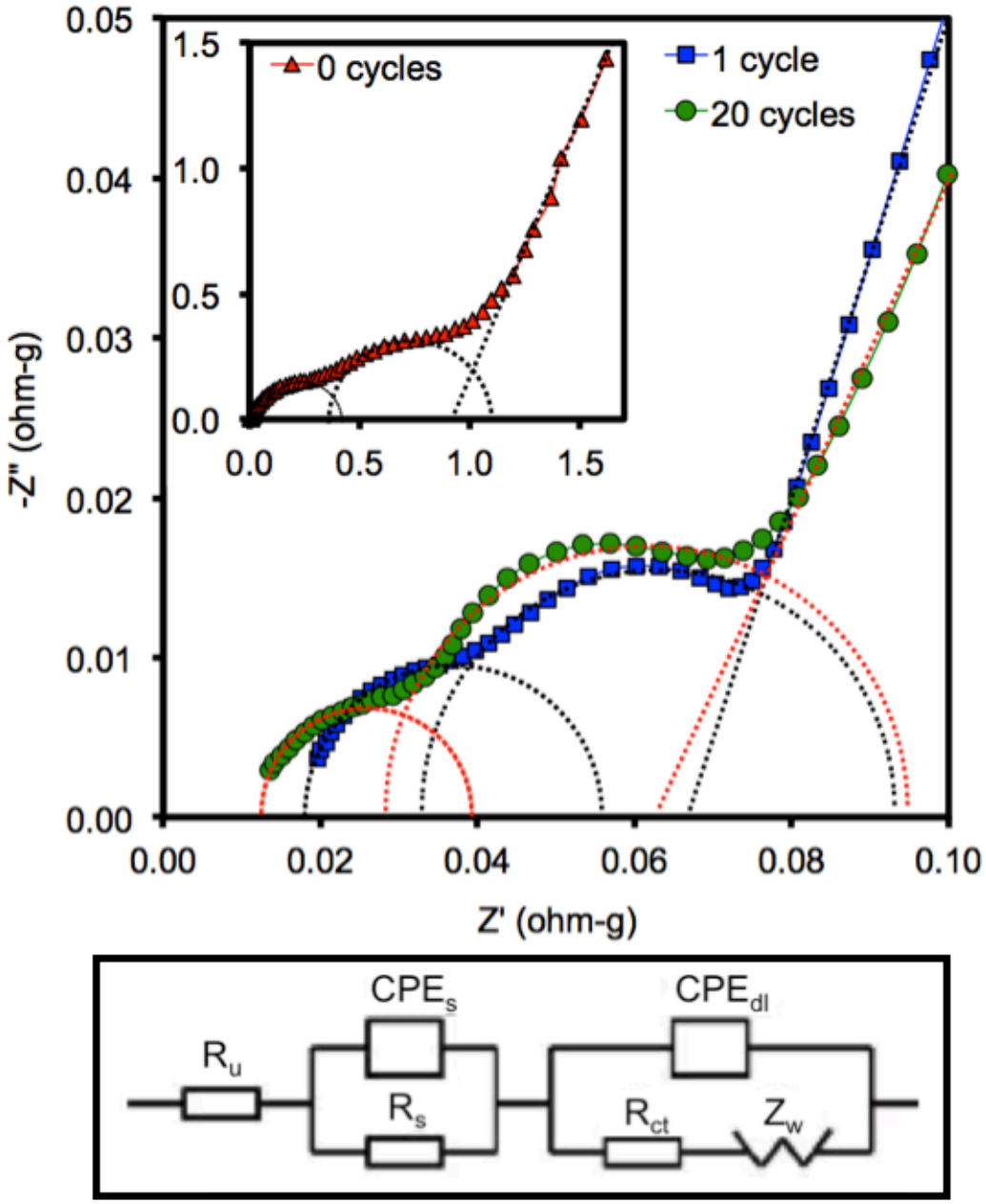

Figure 5.8. The equivalent circuit used for the impedance measurements and electrochemical impedance spectra (EIS) of the Cu_6Sn_5-TiC-C nanocomposite material before cycling (inset), after the 1st cycle, and after the 20th cycle.

Before cycling (Fig. 5.8, inset), the Cu_6Sn_5-TiC-C sample exhibits R_s, R_{ct}, and bulk diffusion resistances that are all an order of magnitude larger than the resistances of the Cu_6Sn_5-TiC-C samples after 1 or 20 cycles. After 20 cycles, the discharge capacity has begun to increase slightly, and this may be due to a decrease in bulk diffusion and surface resistances. When comparing the charge transfer resistance between the first and 20^{th} cycle, it was observed that the charge transfer resistance of the sample that had been cycled 20 times was higher, though not significantly. An increase in the charge transfer resistance after 20 cycles indicates that the electrochemical reactions between the particles or between the electrode and the electrolyte are becoming more difficult.

5.3.3 TEM and XRD of cycled electrodes

In order to better understand the changes in morphology of the Cu_6Sn_5-TiC-C material during cycling, XRD and high-resolution TEM were performed on electrode materials that had been fully discharged down to 0 V vs. Li/Li^+ and cycled between 0 and 200 cycles. After 200 cycles, the capacity of the Cu_6Sn_5-TiC-C electrode had been reduced to less than one percent of the original capacity. The XRD patterns for Cu_6Sn_5-TiC-C electrodes after up to 200 cycles do not change significantly for the electrodes that have been cycled, even after the material stops showing any appreciable capacity. This indicates that the particles are not agglomerating or significantly changing in size. The results of the XRD on cycled Cu_6Sn_5-TiC-C electrodes are further supported by the TEM images in Figure 5.9. The TEM images show that the morphology and size of the Cu_6Sn_5 particles do not change significantly during cycling, even after the material has failed.

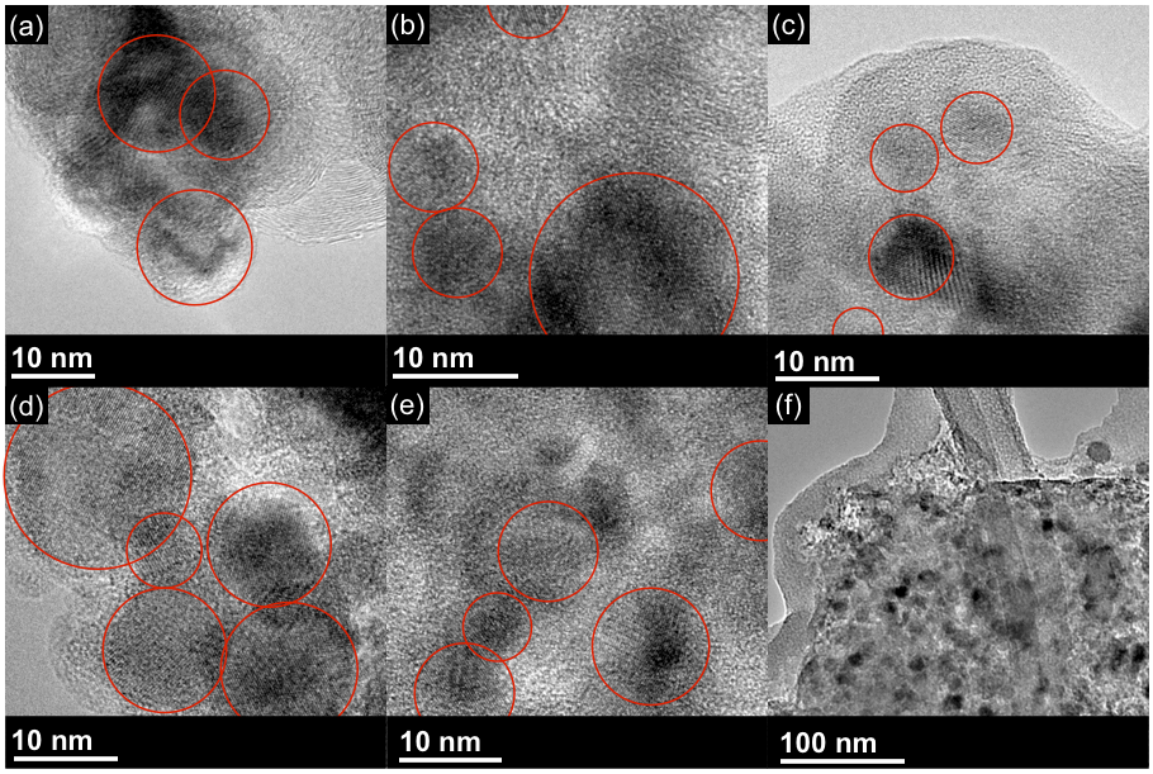

Figure 5.9. TEM of Cu_6Sn_5-TiC-C electrodes after (a) 0 cycle, (b) 20 cycles, (c) 50 cycles, (d) 100 cycles, and (e & f) 200 cycles.

5.4 CONCLUSIONS

The Cu_6Sn_5-TiC-C nanocomposite has been investigated as an anode material for lithium-ion batteries. Characterization data collected on Cu_6Sn_5-TiC-C with XRD, TEM, and STEM reveal a material that contains highly crystalline Cu_6Sn_5 particles mixed heterogeneously with crystalline TiC and dispersed within a conductive carbon matrix. When operated between 0 - 2.0 V vs. Li/Li^+, the Cu_6Sn_5-TiC-C nanocomposite anode shows a four-fold improvement in volumetric capacity over graphite and stable cycle life of 70 cycles. The length of stable cycle performance is doubled when the material is only discharged to 0.2 V vs. Li/Li^+. This improvement in cycle life is due to the avoidance of the structural changes that occur during the transition from Li_2CuSn to $Li_{4.4}Sn$. The

exceptionally high tap density of 2.2 g/cm^3 of the Cu_6Sn_5-TiC-C nanocomposite results in a volumetric capacity that is at least four times higher than that of the graphite anode and nearly 30 % higher than what can be achieved with silicon. The composition of this novel anode material is bronze alloy, titanium carbide, and carbon, which improve structural integrity of the electrode and are less toxic to the environment than many of the alternatives, including the commercialized Nexelion Sn-Co-C anode. Finally, it may be possible to further improve the cycle life when Cu_6Sn_5-TiC-C is fully lithiated by further reducing the particle size of the material.

Chapter 6: Optimization of Nanocomposite Alloy Anodes

6.1 INTRODUCTION

The electrolyte additives chosen for this study were from the carbonate family: Vinylene carbonate (VC), Fluoroethylene carbonate (FEC), and vinylethylene carbonate (VEC). The objective of experimentation with electrolyte additives was to improve the coulombic efficiency and reduce the first cycle irreversible capacity loss of Cu_2Sb-Al_2O_3-C anode materials. The mechanism for the beneficial effects of the electrolyte additives are not fully understood, but it is believed that the additives decompose upon cycling and form protective layers on the surface of the electrodes. Each of the electrolyte additives has a different reduction potential, which affects the voltage at which the protective layers are formed. Accordingly, this chapter presents an investigation of the effects of electrolyte additives on the coulombic efficiency and voltage profile of the Cu_2Sb-Al_2O_3-C nanocomposite alloy anodes in conventional half-cells and symmetric cells.

6.2 EXPERIMENTAL

The Cu_2Sb-Al_2O_3-C nanocomposite was synthesized by a reduction of Sb_2O_3 (99.6 %, Alfa) with aluminum (99.97 %, 17 μm, Alfa) and formation of Cu_2Sb with copper (99 %, 45 μm Acros Organics) metal powder in the presence of carbon (acetylene black) by a high-energy mechanical milling (HEMM) process, as discussed in Chapter 4.

The electrodes for the half cell experiments were prepared and tested according to details listed in chapter 2.2.6. For the symmetric cell preparation, a conventional half cell was assembled with a Cu_2Sb-Al_2O_3-C electrode with approximately twice the area of a normal half cell. This Cu_2Sb-Al_2O_3-C half cell with a larger electrode was then subjected to one conditioning cycle, followed by full lithiation. After full lithiation, the large Cu_2Sb-Al_2O_3-C electrode was removed from its half cell and used as the counter

electrode in a coin cell with a pristine Cu_2Sb-Al_2O_3-C electrode and a layer of blown micro fiber polypropylene (BMF, 3M) and Celgard separator material. The electrolytes with additives were prepared by adding the appropriate amount of VC (97 % with < 2 % BHT, Aldrich), VEC (99%, Aldrich), and FEC (SynQuest Labs) by volume to 1 M $LiPF_6$ in ethylene carbonate (EC)/diethyl carbonate (DEC) (1 : 1 v/v). The discharge–charge experiments were performed galvanostatically at a constant current density of 100 mA/g of active material within the voltage range of 0 – 2.0 V vs. Li/Li^+ or 0.2 V – OCV vs. Li/Li^+. Cycle testing was performed at 25 ºC.

6.3 RESULTS AND DISCUSSION

6.3.1 Half cell testing

Initially, half cells were used to compare the effects 2 % VC, 2 % VEC, and 2 % FEC electrolyte additives. Figure 6.1 shows the coulombic efficiencies of half cells fabricated with and without 2 % VC, VEC, and FEC additives. The 2 % VEC cell shows the best coulombic efficiency of all of the cells tested. The discharge capacities of the cells with 2 % electrolyte additives are shown in the inset in Figure 6.1. The 2 % FEC cell exhibits higher capacity than the other cells, but the capacity retention is poor as evidenced by the poor coulombic efficiency as well.

Because the half cells with 2 % VEC showed the best coulombic efficiency out of the three additives, VEC was chosen for further optimization. Different amounts of VEC were introduced into the electrolyte and used to make a series of half cells with 1, 2, 4, 6, 8, and 10 % VEC. Figure 6.2 shows the coulombic efficiencies and discharge capacities (inset) of half cells fabricated with 1, 2, 4, and 6 % VEC electrolyte additive. Above 6 % VEC, the cycle performance was too poor to warrant any comparisons. In Figure 6.2, The discharge capacity of the half cell with 1 % VEC is the highest among the four cells

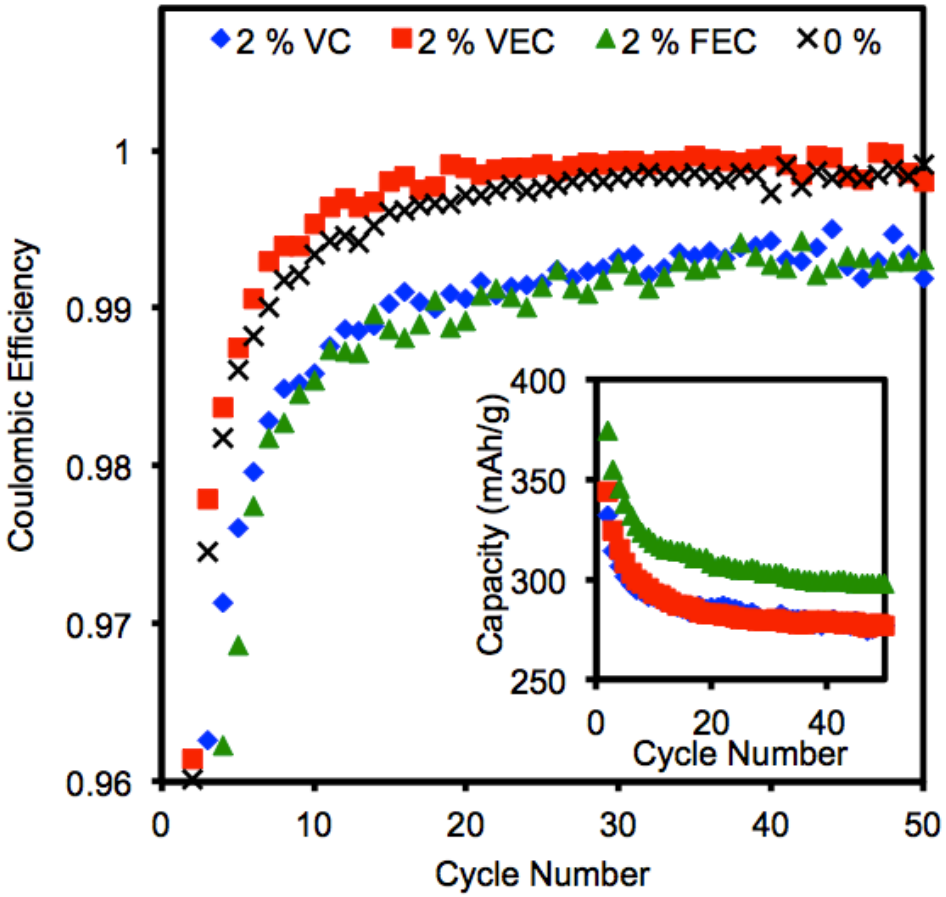

Figure 6.1. Coulombic efficiency and cycle performance (inset) of Cu_2Sb-Al_2O_3-C half-cells with 2 % VC, 2 % VEC, and 2 % FEC at 100 mA/g and 25 ºC between 0 and 2 V vs. Li/Li^+.

shown, but the coulombic efficiency of the cell with 1 % VEC is the lowest of the four cells. The coulombic efficiencies of the cells with 2 and 4 % VEC are virtually the same after 50 cycles. Because choosing the optimal amount of electrolyte additive is a balancing act between coulombic efficiency and discharge capacity, it was concluded that the half cells with 2 % VEC exhibit the best overall performance. The half cells with 2 % VEC have coulombic efficiencies similar to the half cells with 4 % VEC, but the

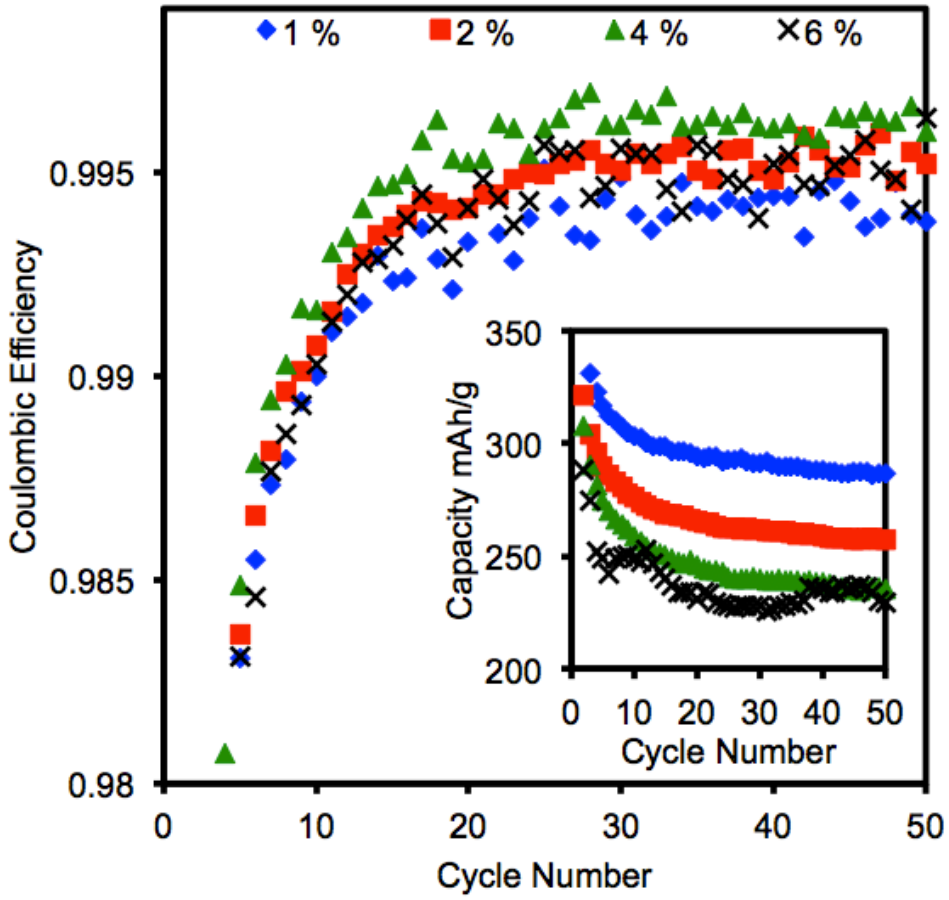

Figure 6.2. Coulombic efficiency and cycle performance (inset) of Cu_2Sb-Al_2O_3-C half-cells with 1, 2, 4, and 6 % VEC at 100 mA/g and 25 ºC between 0 and 2 V vs. Li/Li^+.

discharge capacity of the cells with 2 % VEC are nearly 25 mAh/g higher than those with 4 % VEC.

6.3.2 Symmetric cell testing

Because symmetric cell testing is viewed as a way to speed up the process of optimization, symmetric cells were made for experiments analogous to those performed with half cells. Figure 6.3 shows the coulombic efficiencies of symmetric cells with and

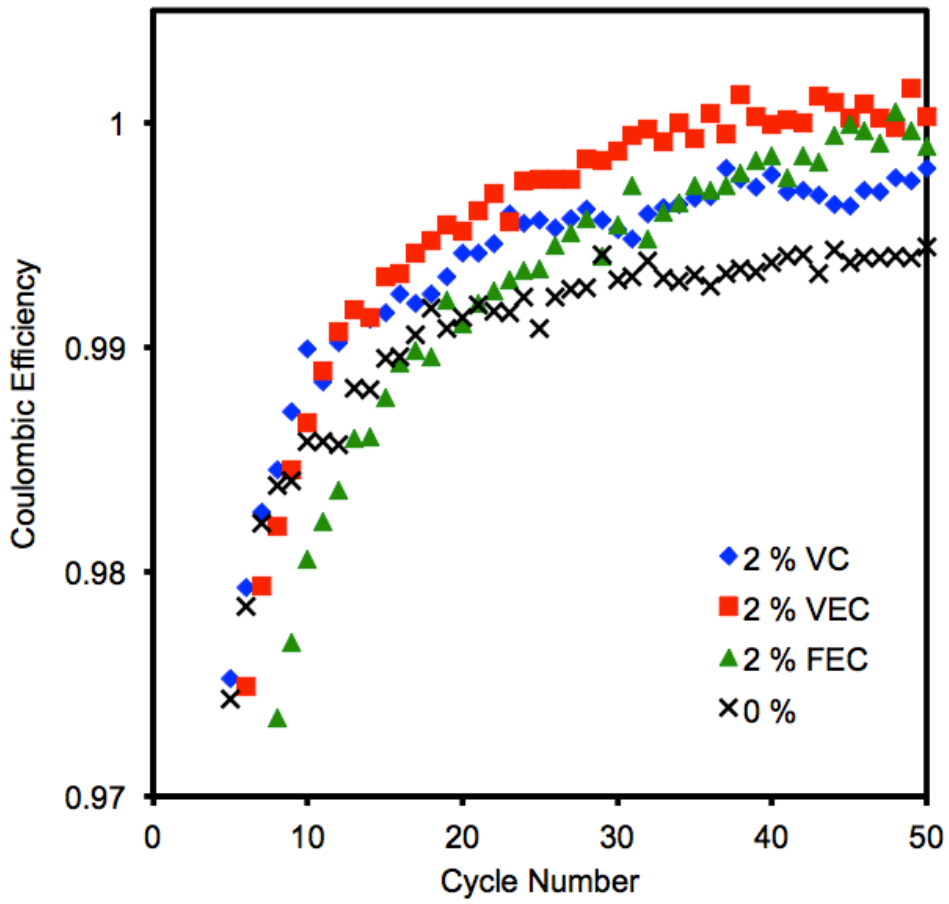

Figure 6.3. Coulombic efficiency of Cu_2Sb-Al_2O_3-C symmetric cells without and with 2 % VC, 2 % VEC, and 2 % FEC at 100 mA/g and 25 ºC between 0 and 2 V vs. Li/Li^+.

without 2 % VC, 2 % VEC, and 2 % FEC additives. Of the three electrolyte additives, VEC shows the best performance in terms of coulombic efficiency.

Figure 6.4 shows the comparison between symmetric cells made with and without 1, 2, and 4 % VEC. The symmetric cell with 2 % VEC shows the highest coulombic efficiency. In one fifth of the cycling time, symmetric cell testing confirmed the results that were obtained through half-cell testing with various electrolyte additives.

6.3.3 Comparison of reduction potentials

In order to better understand the effects of the electrolyte additives on the performance of the cells, differential capacity plots (DCP) were made for each half cell. Figure 6.5 compares the first cycle DCP of the cell without any electrolyte additive with

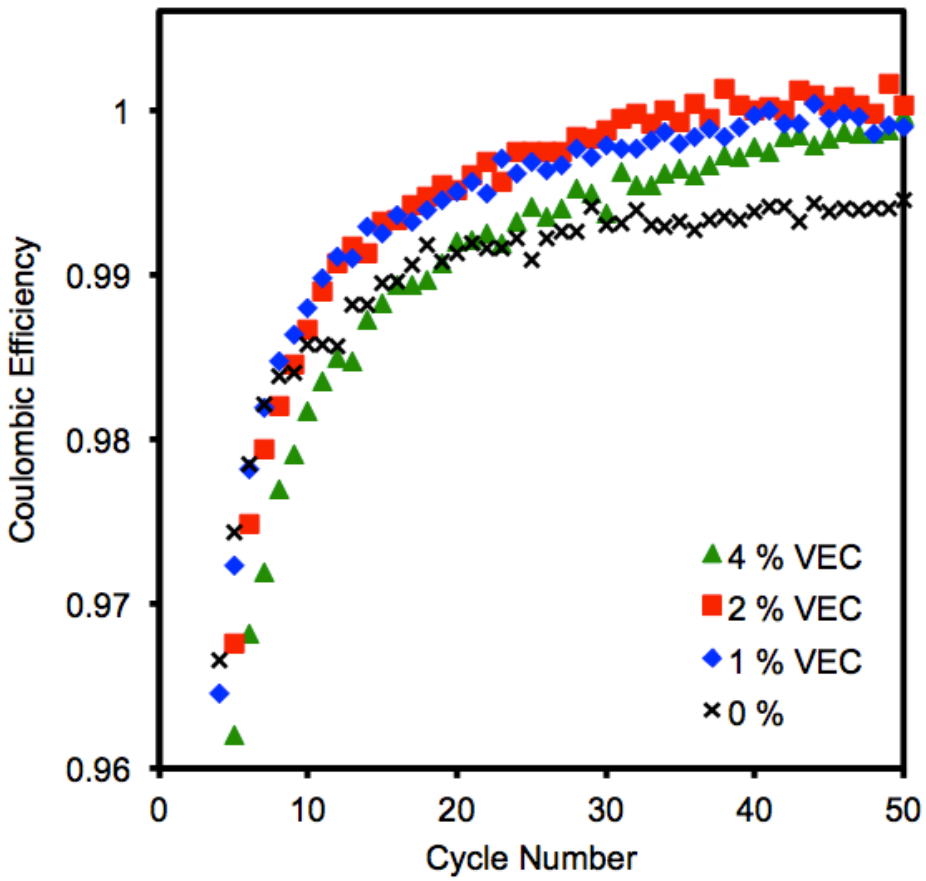

Figure 6.4. Coulombic efficiency of Cu_2Sb-Al_2O_3-C symmetric cells without and with 1, 2, and 4 % VEC at 100 mA/g and 25 ºC between 0 and 2 V vs. Li/Li^+.

those of cells with 2 % VC, VEC, and FEC additives. The most striking feature of Figure 6.5 is the peak that occurs for the cell with 2 % VEC at ~ 1.2 V vs. Li/Li^+ in the lithiation (discharge) cycle. This peak corresponds to the reduction of VEC. The reduction reactions for VC and FEC appear in the DCP as a series of small peaks that occur at 1.5

and 1.1 V for VC and 1.8, 1.5, and 1.1 V for FEC. The second cycle DCP for each of the three additives at 2 % is shown in Figure 6.6. All of the electrolyte reduction peaks do not appear in the second cycle. This indicates that the SEI layer has been formed during the first cycle and further electrolyte reduction is minimal. Furthermore, the amount of the electrolyte additive that is present in the cell can affect the potential at which the electrolyte is reduced [83]. Figure 6.7 shows that as the amount of VEC increases, the reduction potential for the electrolyte also increases.

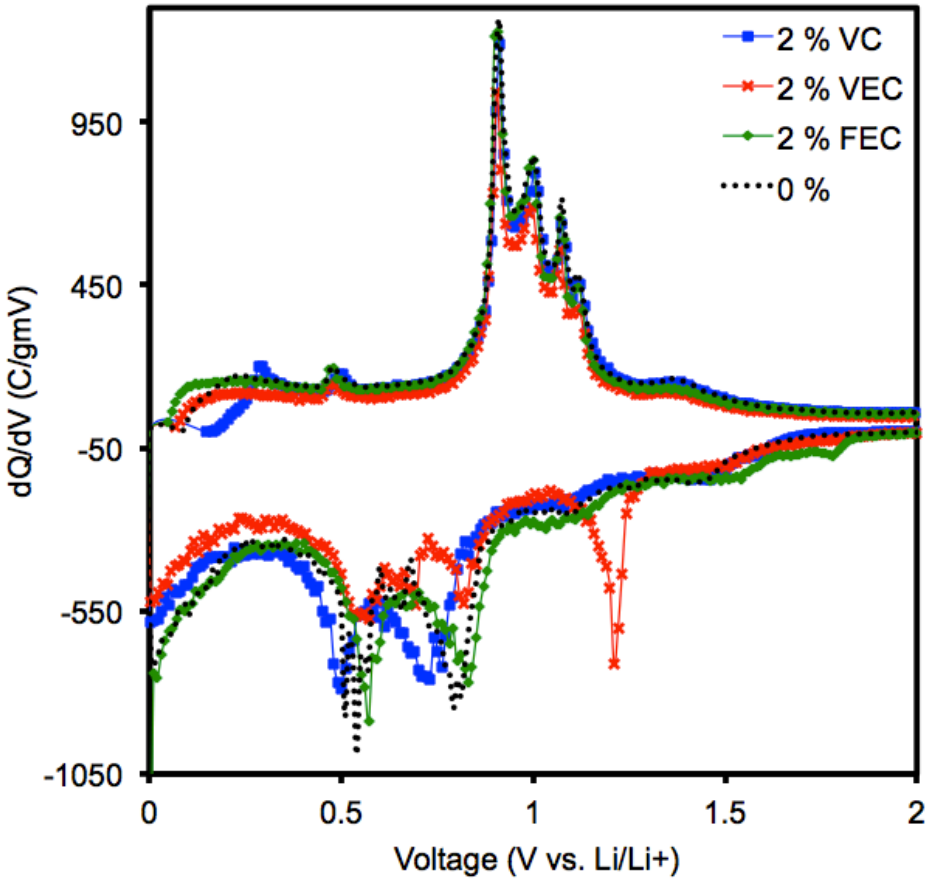

Figure 6.5. First cycle differential capacity plots (DCPs) of Cu_2Sb-Al_2O_3-C half cells without and with 2 % VC, 2 % VEC, and 2 % FEC at 100 mA/g and 25 ºC between 0 and 2 V vs. Li/Li^+.

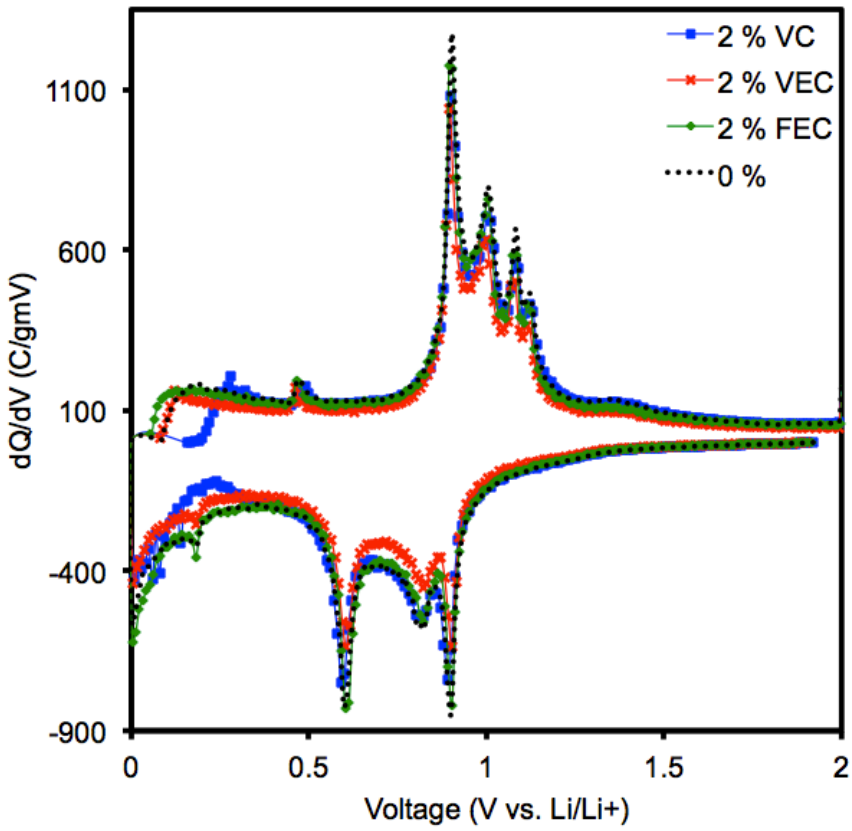

Figure 6.6. Second cycle differential capacity plots (DCPs) of Cu_2Sb-Al_2O_3-C half cells without and with 2 % VC, 2 % VEC, and 2 % FEC at 100 mA/g and 25 ºC between 0 and 2 V vs. Li/Li^+.

6.4 CONCLUSIONS

Cu_2Sb-Al_2O_3-C is known to show exceptional cycle life (500 + cycles) [88] as seen in Chapter 4, and the incorporation of additives into the electrolytes is found in this Chapter as a way to further optimize its electrochemical performance and minimize losses. Among the three additives (VC, VEC, and FEC) investigated with different concentrations, 2 % VEC is found to offer the best cell performance with the Cu_2Sb-Al_2O_3-C anode. Above 4 % VEC, the cycle performance becomes less stable. Differential capacity plots reveal that as the amount of VEC additive is increased, the electrolyte reduction potential also increases, but too high a concentration of the additives

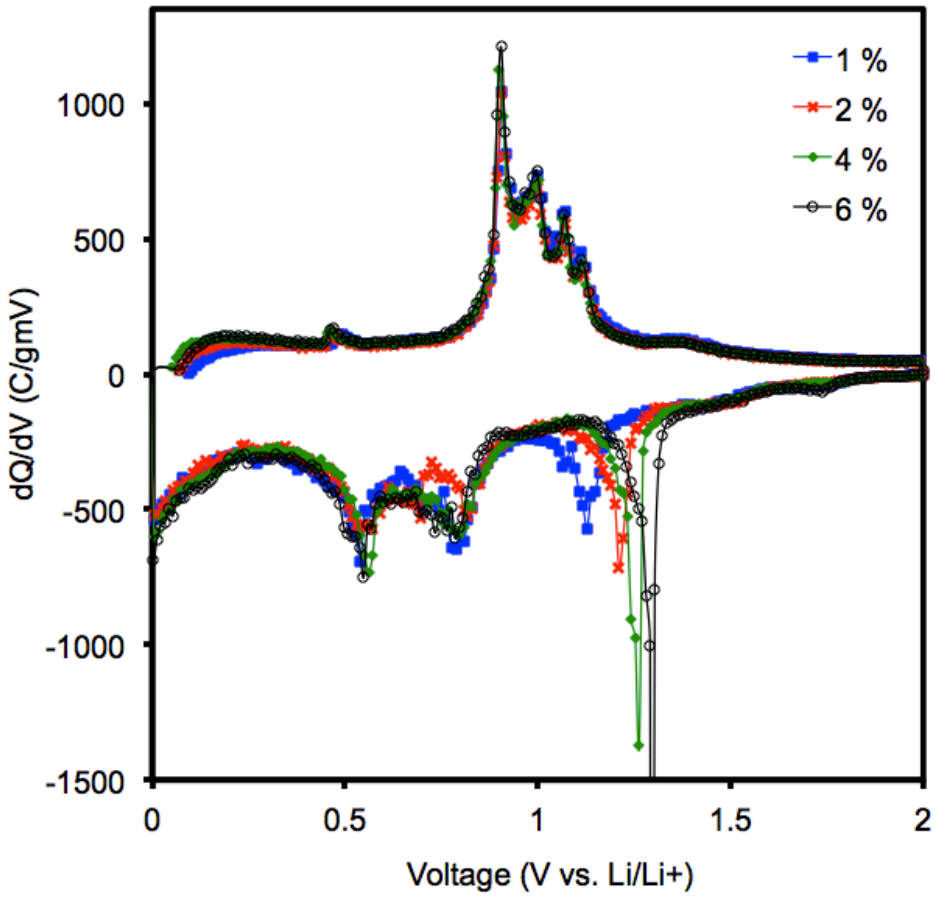

Figure 6.7. First cycle differential capacity plots (DCPs) of Cu_2Sb-Al_2O_3-C half cells with 1, 2, 4, and 6 % VEC at 100 mA/g and 25 ºC between 0 and 2 V vs. Li/Li^+.

sacrifices the discharge capacity. Furthermore, symmetric cell testing is found as an effective way for rapidly determining the effects of electrolyte additives on electrode materials for lithium-ion batteries; the symmetric cell testing can speed up the process of optimizing battery materials.

Chapter 7: Summary

This dissertation explored the properties and performance of a group of Sb- and Sn-based composite anode materials. The goal was to develop lithium-ion battery anode materials that could be viable alternatives to commercial graphite. The synthesis methods used are simple and scalable in order to further increase the likelihood that the developed materials would be commercialized. The materials developed in this research all react with lithium at reduction potentials that are higher than that for the reaction of lithium with graphite. This increase in reduction potential translates to safer operation of the anodes, particularly at low temperatures.

Mo_3Sb_7-C is a novel battery material that has a discharge capacity of 518 mAh/g (907 mAh/cm^3) and a tap density of 1.75 g/cm^3. The volumetric discharge capacity of Mo_3Sb_7-C composite anodes is three times higher than that of graphite anodes. The performance of Mo_3Sb_7-C was optimized by using 30 wt. % Super P rather than 20 wt. % acetylene black. A related composite was also created by adding 4 atom % excess molybdenum metal powder to the reaction mixture: Sb-Mo-MoO_2-C. The cycle life of Sb-Mo-MoO_2-C was preferable to that of Mo_3Sb_7-C, and further optimization is possible.

Cu_2Sb-Al_2O_3-C was synthesized via one-step mechanochemical reduction. The particle size distribution of Cu_2Sb-Al_2O_3-C with 20 wt. % acetylene black is 2 – 10 nm and the material has a capacity retention of 80 % over 500 cycles (330 mAh/g) after the first cycle. When the amount of carbon in the composite is reduced, the cycle life becomes poor, and 20 wt. % was found to be the minimum amount of carbon necessary to achieve stable cycle life of over 300 cycles. When the milling synthesis time is increased from 12 to 24 h, the first cycle coulombic efficiency is increased from 67 to 75 % and the cycle performance over 200 cycles is more stable. TEM of cycled electrodes

showed that even over 500 cycles, the crystalline Cu_2Sb particles in the composite do not agglomerate or increase in size.

Studies of the reaction mechanism were performed with *ex-situ* XRD and cycling within limited potential windows. The *ex-situ* XRD data did not reveal information about the reaction mechanism due to the small crystallite size and the amorphous nature of the Al_2O_3 present in the composite. The DCPs from cycling under a wide array of voltage ranges showed that the reaction mechanism of Cu_2Sb-Al_2O_3-C is asymmetric and fully reversible. The proposed reaction mechanism for Cu_2Sb-Al_2O_3-C is:

Insertion:
$$Cu_2Sb + Li^+ \rightarrow LiCu_2Sb \quad (7.1)$$
$$LiCu_2Sb + Li^+ \rightarrow Li_2CuSb + Cu \quad (7.2)$$
$$Li_2CuSb + Li^+ \rightarrow Li_3Sb + Cu \quad (7.3)$$

Extraction:
$$Li_3Sb + Cu \rightarrow Li_2CuSb + Li^+ \quad (7.4)$$
$$Li_2CuSb \rightarrow LiCuSb + Li^+ \quad (7.5)$$
$$LiCuSb + Cu \rightarrow LiCu_2Sb \quad (7.6)$$
$$LiCu_2Sb \rightarrow Cu_2Sb + Li^+ \quad (7.7)$$

The charge cycle in the proposed reaction mechanism includes four steps, which is different from the published reaction mechanism for Cu_2Sb. It is believed that the difference in reaction mechanism is due to the small size of the crystalline Cu_2Sb particles within the Cu_2Sb-Al_2O_3-C composite. Further analysis is necessary to provide further evidence of the size-dependence of the reaction of Cu_2Sb with lithium. Sb Mössbauer, NMR, and *in-situ* x-ray absorption spectroscopy have been proposed as potential analysis techniques that could further investigate the reaction mechanism. If the size-dependence of the reaction mechanism is confirmed, the impact on the area of nanoscale battery materials could be significant.

The coulombic efficiency of Cu_2Sb-Al_2O_3-C anode material was further improved through the introduction of 2 % VEC into the electrolyte. Symmetric cell testing was used to rapidly determine the optimal amount of electrolyte additive, and is considered to be a valuable tool for evaluating battery materials. More optimization is possible for Cu_2Sb-Al_2O_3-C anode materials through experimentation with different binders, separator material, milling time, and etc.

With a second cycle discharge capacity of 1340 mAh/cm^3 (610 mAh/g) and a tap density of 2.2 g/cm^3, the Cu_6Sn_5-TiC-C nanocomposite anode offers a volumetric capacity that is at least four times higher than that of the graphite anode and 30 % higher than what can be achieved with silicon. Cu_6Sn_5-TiC-C is made of components that are relatively environmentally friendly, which is not often the case with battery materials. The reaction mechanism for the Cu_6Sn_5-TiC-C nanocomposite does not appear to be a distinct two step mechanism, rather it is thought to be a gradual blend of the following two reactions:

$$10\ Li + Cu_6Sn_5 \rightarrow 5\ Li_2CuSn + Cu \qquad (7.8)$$

$$2.2\ Li + Li_2CuSn \rightarrow Li_{4.4}Sn + Cu \qquad (7.9)$$

TEM studies on cycled electrodes showed that the crystalline particles of Cu_6Sn_5 do not change significantly during cycling. Optimization of carbon content, electrolyte additives, and synthesis conditions could further improve the performance of Cu_6Sn_5-TiC-C.

Overall, the goals of developing composite alloy anode materials to be alternatives to graphite were achieved. An entire library of materials following the formulas M'_ySb-MO_x-C (M = metals like Al, Mg, Ti, V, Cr, Mn, Fe, Co, Ni, Zr, Mo, W, Nb, Ta… and M' = elements such as Cu, Mo, Ni, Ti, Zn, Sn…) and M'_ySn-MC_x-C (M = elements such as Ti, V, Cr, Fe, Co, Ni, Mo, W, Si… and M' = elements such as Cu, Mo,

Ni, Ti, Zn, Sb…) might hold further possibilities for alternative anodes and should be explored. Also, *in situ* investigation of the charge-discharge processes with a combination of techniques such as X-ray diffraction, neutron diffraction, X-ray absorption spectroscopy, Raman spectroscopy, and high resolution transmission electron microscopy could enhance further the understanding of the charge-discharge mechanisms of these nanocomposite materials and reveal how these nanocomposites differ from conventional micron size particles. Such studies and understanding can help to design and develop optimized high-performance alloy compositions as anodes for next generation lithium-ion batteries.

References

1. M. Winter, J.O. Besenhard, M.E. Spahr, and P. Novák, *Adv. Mater.* **10**, 725–763 (1998).
2. R. A. Huggins, *J. Power Sources* **81–82**, 13–19 (1999).
3. P. Limthongkul, H. Wang, and Y-M. Chiang, *Chem. Mater.* **13**, 2397-2402 (2001).
4. H. Bryngelsson, J. Eskhult, L. Nyholm, M. Herranen, O. Alm, and K. Edström, *Chem. Mater.* **19**, 1170-1180 (2007).
5. C-M. Park, S. Yoon, S-I. Lee, J-H. Kim, J-H. Jung, and H-J. Sohn, *J. Electrochem. Soc.* **154**, A917-A920 (2007).
6. J. O. Besenhard, M. Hess, and P. Komenda, *Solid State Ionics* **40-41**, 525-529 (1990).
7. J. L. Tirado, *Materials Science and Engineering R* **40**, 103-136 (2003).
8. L. M. L. Fransson, J. T. Vaughey, R. Benedek, K. Edström, J. O. Thomas, and M. M. Thackeray, *Electrochem. Commun.* **3**, 317-323 (2001).
9. R. Alcántara, F. J. Fernández-Madrigal, P. Lavela, J. L. Tirado, J. C. Jumas, and J. Olivier-Fourcade, *J. Mater. Chem.* **9**, 2517-2521 (1999).
10. F. J. Fernández-Madrigal, P. Lavela, C. Pérez-Vicente, and J. L. Tirado, *J. Electroanal. Chem.* **501**, 205–209 (2001).
11. L. M. L. Fransson, J. T. Vaughey, K. Edström, and M. M. Thackeray, *J. Electrochem. Soc.* **150**, A86-A91 (2003).
12. J. Yang, Y. Takeda, N. Imanish, and O. Yamamoto, *J. Electrochem. Soc.* **146**, 4009-4013 (1999).
13. H. Li, L. Shi, W. Lu, X. Huang, and L. J. Chen, *Electrochem. Soc.* **148**, A915-A922 (2001).
14. M-S. Park, S. A. Needham, G-X. Wang, Y-M. Kang, J-S. Park, S-X. Dou, and H-K. Liu, *Chem. Mater.* **19**, 2406-2410 (2007).
15. K. C. Hewitt, L. Y. Beaulieu, and J. R. Dahn, *J. Electrochem. Soc.* **148**, A402-A410 (2001).
16. A. S. Arico, P. Bruce, B. Scrosati, J.-M. Tarascon, and W. Van Schalkwijc, *Nature Mater.* **4**, 366-377 (2005).
17. G. Derrien, J. Hassoun, S. Panero, and B. Scrosati, *Adv. Mater.* **19**, 2336-2340 (2007).

18. A. D. W. Todd, R. E. Mar and J. R. Dahn, *J. Electrochem. Soc.* **153**, A1998-A2005 (2006).

19. J-M. Tarascon and M. Armand, *Nature* **414**, 359-367 (2001).

20. R. Retoux, T. Brousse, and D.M. Schleich, *J. Electrochem. Soc.* **146**, 2472-2476 (1999).

21. M. Holzapfel, H. Buqa, W. Scheifele, P. Novák, and F-M. Petrat, *Chem. Commun.* 1566-1568 (2005).

22. M. Winter and J.O. Besenhard, *Electrochim. Acta* **45**, 31-50 (1999).

23. S. Yoon and A. Manthiram, *Electrochim. Acta* **56**, 3029-3035 (2011).

24. K.D. Kepler, J.T. Vaughey, and M.M. Thackeray, *J. Power Sources* **81-82**, 383-387 (1999).

25. S. Sharma, L. Fransson, E. Sjöstedt, L. Nordström, B. Johansson, and K. Edström, *J. Electrochem. Soc.* **150**, A330-A334 (2003).

26. T. Sarakonsri, C.S. Johnson, S.A. Hackney, and M.M. Thackeray, *J. Power Sources* **153**, 319-327 (2006).

27. M.M. Thackeray, J.T. Vaughey, C.S. Johnson, A.J. Kropf, R. Benedek, L.M.L. Fransson, and K. Edström, *J. Power Sources* **113**, 124-130 (2003).

28. J. S. Thorne, J. R. Dahn, M. N. Obrovac, and R. A. Dunlap, *J. Electrochem. Soc.* **158**, A1328-A1334 (2011).

29. X. B. Zhao and G. S. Cao, *Electrochim. Acta* **46**, 891–896 (2001).

30. H. Honda, H. Sakaguchi, Y. Fukuda, and T. Esaka, *Mater. Res. Bull.* **38**, 647–656 (2003).

31. D. L. Chen, M. C. Chaturvedi, N. Goel, and N. L. Richards, *Int. J. Fatigue* **21**, 1079–1086 (1999).

32. M. S. El-Eskandarany, *J. Alloys Compd.* **279**, 263–271 (1998).

33. G-J. Jeong, Y. U. Kim, H-J. Sohn, and T. Kang, *J. Power Sources* **101**, 201-205 (2001).

34. S. Yoon and A. Manthiram, *Chem. Mater.* **21**, 3898-3904 (2009).

35. H. Bryngelsson, J. Eskhult, L. Nyholm, and K. Edström, *Electrochim. Acta* **53** 7226–7234 (2008).

36. R. L. Kift and T. J. Prior, *J. Alloy Compd.* **505** 428–433 (2010).

37. M. Kundu, S. Mahanty, and R. N. Basu, *Electrochem. Commun.* **11** 1389–1392 (2009).

38. D. Larcher, S. Beattie, M. Morcrette, K. Edström, J-C. Jumas, and J-M. Tarascon, *J. Mater. Chem.* **17** 3759-3772 (2007).

39. M. Morcrette, D. Larcher, J.M. Tarascon, K. Edström, J.T. Vaughey, M.M. Thackeray, *Electrochim. Acta* **52** 5339–5345 (2007).

40. J. M. Mosby and A. L. Prieto, *J. Am. Chem. Soc.* **130** 10656–10661 (2008).

41. L. Trahey, H. H. Kung, M. M. Thackeray, and J. T. Vaughey, *Eur. J. Inorg. Chem.* 3984–3988 (2011).

42. W-J. Zhang, *J. Power Sources* **196** 13-24 (2011).

43. Y. He, L. Huang, X. Li, Y. Xiao, G-L. Xu, J-T. Li, and S-G. Sun, *J. Mater. Chem.* **21** 18517-18519 (2011).

44. M.D. Fleischauer, M.N. Obrovac, J.D. McGraw, R.A. Dunlap, J.M. Topple, J.R. Dahn, *J. Electrochem. Soc.* **153** A484-A491 (2006).

45. U. Kasavajjula, C. Wang, and A. J. Appleby, *J. Power Sources* **163** 1003–1039 (2007).

46. B.A. Boukamp, G.C. Lesh, and R.A. Huggins, *J. Electrochem. Soc.* **128** 725-729 (1981).

47. C. K. Chan, R. N. Patel, M. J. O'Connell, B. A. Korgel, and Y. Cui, *ACS Nano* **4** 1443–1450 (2010).

48. S. Bourderau, T. Brousse, and D.M Schleich, *J. Power Sources* **81–82** 233–236 (1999).

49. L-F. Cui, R. Ruffo, C. K. Chan, H. Peng, and Y. Cui, *Nano Lett.* **9** 491–495 (2009).

50. M-H. Park, M. G. Kim, J. Joo, K. Kim, J. Kim, S. Ahn, Y. Cui, and J. Cho, *Nano Lett.* **9** 3844–3847 (2009).

51. J. Graetz, C. C. Ahn, R. Yazami, and B. Fultz, *Electrochem. Solid-State Lett.* **6** A194-A197 (2003).

52. C. K. Chan, H. Peng, G. Liu, K. McIlwrath, X. F. Zhang, R. Huggins, and Y. Cui, *Nat. Nanotechnol.* **3** 31-35 (2008).

53. M. Uehara, J. Suzuki, K. Tamura, K. Sekine, and T. Takamura, *J. Power Sources* **146** 441–444 (2005).

54. Z. P. Guo, E. Milin, J. Z. Wang, J. Chen, and H. K. Liu, *J. Electrochem. Soc.* **152** A2211-A2216 (2005).

55. M-H. Park, M. G. Kim, J. Joo, K. Kim, J. Kim, S. Ahn, Y. Cui, and J. Cho, *Nano Lett.* **9** 3844–3847 (2009).

56. J. Xiao, W. Xu, D. Wang, D. Choi, W. Wang, X. Li, G. L. Graff, J. Liu, and J. Zhang, *J. Electrochem. Soc.* **157** A1047-A1051 (2010).

57. D. Aurbach, K. Gamolsky, B. Markovsky, Y. Gofer, M. Schmidt, U. Heider, *Electrochim. Acta* **47** 1423-1439 (2002).

58. J. C. Burns, N. N. Sinha, D. J. Coyle, G. Jain, C. M. VanElzen, W. M. Lamanna, A. Xiao, Erik Scott, J. P. Gardner, J. R. Dahn, *J. Electrochem. Soc.* **159** A85-A90 (2012).

59. L. Chen, K. Wang, X. Xie, J. Xie, *J. Power Sources* **174** 538–543 (2007).

60. A.T. Ribes, P. Beaunier, P. Willmann, D. Lemordant, J. *Power Sources* **58** 189-195 (1996).

61. H. Ota, Y. Sakata, A. Inoue, S. Yamaguchi, *J. Electrochem. Soc.* **151** A1659-A1669 (2004).

62. J-A. Choi, Y-K. Sun, E-G. Shim, B. Scrosati, D-W. Kim, *Electrochim. Acta* **56** 10179-10184 (2011).

63. Y. E. Hyung, D. R. Vissers, and K. Amine, *J. Power Sources* **119–121** 383-387 (2003).

64. H.F. Xiang, H.Y. Xu, Z.Z. Wang, C.H. Chen, *J. Power Sources* **173** 562-564 (2007).

65. S. Izquierdo-Gonzales, W. Li, B. L. Lucht, *J. Power Sources* **135** 291-296 (2004).

66. J. C. Burns, L. J. Krause, D-B. Le, L. D. Jensen, A. J. Smith, D. Xiong, J. R. Dahn, *J. Electrochem. Soc.* **158** A1417-A1422 (2011).

67. J. Barker, R. Koksbang, M. Y. Saidi, *Solid State Ionics* **82** 143-151 (1995).

68. H. Kitaura, A. Hayashi, K. Tadanaga, M. Tatsumisago, *J. Electrochem. Soc.* **157** A407-A411 (2010).

69. C.H. Chen, J. Liu, K. Amine, *J. Power Sources* **96** 321-328 (2001).

70. C.H. Chen, J. Liu, K. Amine, *Electrochem. Commun.* **3** 44-47 (2001).

71. S.S. Zhang, K. Xu, T.R. Jow, *J. Power Sources* **115** 137-140 (2003).

72. E-G. Shim, T-H. Nam, J-G. Kim, H-S. Kim, S-I. Moon, *J. Power Sources* **172** 901-907 (2007).

73. N-S. Choi, K. H. Yew, K. Y. Lee, M. Sung, H. Kim, S-S. Kim, *J. Power Sourc*es **161** 1254-1259 (2006).

74. V. Etacheri, O. Haik, Y. Goffer, G. A. Roberts, I. C. Stefan, R. Fasching, D. Aurbach, *Langmuir* **28** 965-976 (2012).

75. S-K. Jeong, M. Inaba, R. Mogi, Y. Iriyama, T. Abe, Z. Ogumi, *Langmuir* **17** 8281-8286 (2001).

76. R. McMillan, H. Slegr, Z.X. Shu, W. Wang, *J. Power Sources* **81–82** 20-26 (1999).

77. H. Nakai, T. Kubota, A. Kita, and A. Kawashima, *J. Electrochem. Soc.* **158** A798-A801 (2011).

78. I. A. Profatilova, S-S. Kim, N-S. Choi, *Electrochimica Acta* **54** 4445-4450 (2009).

79. M-H. Ryou, G-B. Han, Y. M. Lee, J-N. Lee, D. J. Lee, Y. O. Yoon, J-K. Park, *Electrochimica Acta* **55** 2073-2077 (2010).

80. G. Chen, G. V. Zhuang, T. J. Richardson, G. Liu, P. N. Ross, Jr. *Electrochem. Sol. St.* **8** A344-A347 (2005).

81. Y. Hu, W. Kong, H. Li, X. Huang, L. Chen, *Electrochem. Commun.* **6** 126-131 (2004).

82. J. Li, W. Yao, Y. S. Meng, Y. Yang, *J. Phys. Chem. C* **112** 12550-12556 (2008).

83. H. Xiang, J. Chen, H. Wang, *Ionics* **17** 415-420 (2011).

84. U. Häussermann, M. Elding-Pontén, C. Svensson, and S. Lidin, *Chemistry: a*

European Journal **4** 1007-1015 (1998).

85. P. Jensen, and A. Kjekshus, *Acta Chimica Scandinavica* **20** 417-422 (1966).

86. J. T. Vaughey, C. S. Johnson, A. J. Kropf, R. Benedek, M. M. Thackeray, H. Tostmann, T. Sarakonsri, S. Hackney, L. Fransson, K. Edström, and J. O. Thomas, *J. Power Sources* **97-98** 194-197 (2001).

87. J. Liu, and A. Manthiram, *Chem. Mater.* **21** 1695-1707 (2009).

88. D. Applestone, S. Yoon, and A. Manthiram, *J. Mater. Chem.* **22** 3242-3248 (2012).

Vita

Danielle Salina Applestone grew up in Mena, Arkansas and attended public school there until 1996. For 11th and 12th grades of high school, she attended the Arkansas School of Mathematics and Sciences and graduated in 1998. During the last year of high school, she was named a Presidential Scholar by the Clinton administration. She received her S.B. from the Massachusetts Institute of Technology in Chemical Engineering in 2002. She co-founded a software company and worked various jobs in software, construction, and materials science before beginning her study at the University of Texas at Austin in 2004. She joined Professor Arumugam Manthiram in the Materials Science and Engineering Program and began studying battery materials.

List of Publications:

1. D. Applestone, S. Yoon, and A. Manthiram, "Mo_3Sb_7-C Composite Anodes for Lithium-ion Batteries," *The Journal of Physical Chemistry* **115**, 18909-18915 (2011).

2. D. Applestone, S. Yoon, and A. Manthiram, "Cu_2Sb-Al_2O_3-C Nanocomposite Alloy Anodes with Exceptional Cycle Life for Lithium Ion Batteries," *The Journal of Materials Chemistry* **22**, 3242 – 3248 (2012).

3. D. Applestone, and A. Manthiram, "Cu_6Sn_5-TiC-C Nanocomposite Alloy Anodes with High Volumetric Capacity for Lithium Ion Batteries**,"** *RSC Advances,* accepted manuscript (2012).

List of Submitted Manuscripts:

1. D. Applestone, and A. Manthiram, "Symmetric Cell Evaluation of the Effects of Electrolyte Additives on Cu_2Sb-Al_2O_3-C Nanocomposite Anodes," *Journal of Power Sources*, in review.

Email : smile@alum.mit.edu

This dissertation was typed by the author.